Spectrum Sensing in Cognitive Radio

Von der Fakultät für Elektrotechnik und Informationstechnik
der Rheinisch-Westfälischen Technischen Hochschule Aachen
zur Erlangung des akademischen Grades eines Doktors
der Ingenieurwissenschaften genehmigte Dissertation

vorgelegt von

Diplom-Ingenieur
Andreas Bollig

aus Wittlich

Berichter: Prof. Dr. rer. nat. Rudolf Mathar
Prof. Dr.-Ing. habil. Reiner S. Thomä

Tag der mündlichen Prüfung: 26. Oktober 2016

Preface

This thesis was written during my time at the Institute for Theoretical Information Technology of RWTH Aachen University. I would like to thank Prof. Dr. Rudolf Mathar for giving me the opportunity to pursue my doctorate at his institute and for supporting my research. Prof. Dr. Thomä deserves many thanks for acting as the second examiner of this thesis. Furthermore I would like to thank my former colleagues, especially Steven, Martijn, Markus, Niklas and Christopher, for good times as well as extensive and interesting discussions. Last but not least, I would like to thank my family: my wife Maja, my parents Elke and Matthias, and my brothers Christoph and Florian, for supporting me spiritually throughout writing this thesis.

Aachen, December 2016 Andreas Bollig

Contents

1 Introduction

1.1 Motivation

The recent years have seen a dramatic increase in the demand for wireless communication, largely driven by the wide adoption of the smartphone in consumer markets. Despite technological advancements aimed at boosting spectral efficiency such as new waveforms and algorithms as well as hardware enhancements, radio spectrum has become a tremendously scarce resource. One of the reasons for this can be found in the legacy of spectrum licensing policies from the past decades, where licenses have been issued for most of the frequency range suitable for radio communication (for the US, see Figure 1.1 [1]; for Germany, see [2]).

As a consequence of this licensing scheme, large parts of the radio spectrum are severely underutilized, i. e., their licensees only access them at certain geographic locations or certain points in time [3, 4]. This results in an inefficient use of the available assets.

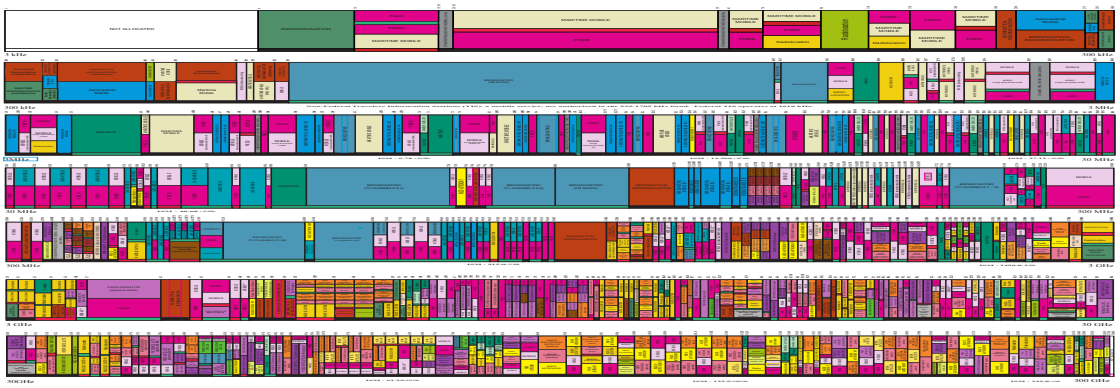

Figure 1.1: United States Frequency Allocations, 2011 [1]. White denotes unallocated spectrum. As can be seen, most of the spectrum has been allocated.

In addition to easing the cellular network operators' growing demand for spectrum, making a change in policy is a necessary step that needs to be taken in order not to stifle innovation in the wireless sector. Examples of this are the widespread deployment of the Internet of Things (IoT) [5, 6, 7] based on machine to machine (M2M) communications and the progressive proliferation of sensor networks [8] in a broad set of scenarios.

One approach towards more efficient spectrum use (given adequate policy changes) is opportunistic spectrum access (OSA) [9], originally called spectrum pooling (SP) [10]. Emanating from the field of cognitive radio (CR) [11, 12], it aims at making better use of the given resources by allowing unlicensed transceivers (secondary users (SUs)) to access spectral bands while their licensees (primary users (PUs)) do not occupy them. To facilitate safe spectrum reuse such that the unlicensed transmission does not cause interference in the primary system, the secondary system has to sense the spectral band of interest for primary user activity reliably and only access it if no ongoing transmission is detected. Determining the occupancy status of a spectral band is known as spectrum sensing. The focus of this work lies on the development and analysis of spectrum sensing algorithms.

1.2 Outline

The thesis is organized as follows. In Chapter 2, the notations used throughout this dissertation are introduced.

Chapter 3 provides an overview of the different fields of study this thesis is based on. The fundamental spectrum sensing problem is introduced together with a short treatment of binary hypothesis testing as well as a review of the most important test statistics used in spectrum sensing. Some methods proposed in this thesis are based on core ideas and algorithms from the field of compressed sensing. Thus, the background chapter contains a synopsis of the field's most important concepts and algorithms. Finally, it is discussed, which problems in the area of spectrum sensing can gain from the application of compressed sensing.

One of the core problems of cyclostationarity-based spectrum sensing is the requirement of knowing the cyclic frequency to test at beforehand. This rules out blind operation. The problem can be fixed by the application of compressed sensing, which is demonstrated in Chapter 4. To tackle the problem, two greedy algorithms based on the orthogonal matching pursuit [13, 14] are proposed. In order to be able to assess the estimation performance of the aforementioned algorithms, a closed-form expression for the discrete-time cyclic autocorrelation of linearly modulated signals with a rectangular pulse shape is derived. Essential information necessary for the estimation of the test statistic used in the time-domain test [15] is lost in the sparse recovery process. This problem is overcome by an alternative way of obtaining the test statistic.

When Eigenvalue-based spectrum sensing was first introduced in [16], one of its advertised advantages was the independence from the exact knowledge of the receiver's noise power, the lack of which leads to a so-called SNR-wall in the energy detector. An SNR-wall is an SNR value below which a detector cannot robustly detect anymore. In Chapter 5, it is shown that while the (eigenvalue-based) maximum-minimum-eigenvalue (MME) detector may not suffer from a noise-power-uncertainty induced SNR-wall, it does experience an SNR-wall when faced with uncertainty in the amount of coloring

of the receiver noise. A lower bound for the SNR-wall based on uncertainty about the amount of noise-coloring is derived and is used to show that low amounts of man-made impulsive noise lead to SNR-walls in the MME detector that are above the desired regime of operation. Furthermore, two new eigenvalue-based test statistics for spectrum sensing are proposed and compared to the most popular ones from the literature.

In Chapter 6, the problem of distributed spectrum sensing using energy detection is studied. A scenario with multiple sensors and a fusion center, which receives raw samples from the sensors, is considered. The fusion center estimates the frequency spectrum from the received measurements, such that at a later stage, it can be decided which parts of the spectrum are occupied and which ones are free to be used opportunistically. An approach for spectral estimation that makes use of samples from all sensors in a single ℓ_1-minimization operation is proposed to minimize the amount of data that has to be transmitted to the fusion center by exploiting spatial diversity.

The numerical evaluation parts of this thesis are based on results of Monte Carlo simulations. Most of these simulations exhibit the same workflow. Blocks of samples are generated, detection algorithms are run on these blocks, and the results are analyzed statistically. In Chapter 7, the software framework that was developed to make the simulation code more reusable and stable is presented.

Finally, Chapter 8 concludes this dissertation with a summary of the presented work and an outlook.

Parts of the present thesis and related topics have been published in [17, 18, 19, 20, 21, 22]. Works containing other parts of the thesis are currently under review, i. e., [23, 24].

2 Notation

This chapter introduces the notation used throughout the thesis.

Scalars Scalars are denoted by lowercase symbols with normal font-weight, e. g.,

$$x. \tag{2.1}$$

The complex conjugate of the scalar x is given by

$$x^*, \tag{2.2}$$

while its absolute value is given by

$$|x|. \tag{2.3}$$

Vectors Vectors are denoted by lowercase bold-faced type , e. g.,

$$\mathbf{x}. \tag{2.4}$$

To denote the i-th element of the vector $\mathbf{x}$, the following notations are used interchangeably:

$$x_i \text{ and } [\mathbf{x}]_i . \tag{2.5}$$

The transpose, element-wise complex conjugate and conjugate transpose of the vector $\mathbf{x}$ are given by

$$\mathbf{x}^{\mathrm{T}}, \mathbf{x}^*, \text{ and } \mathbf{x}^{\mathrm{H}}, \tag{2.6}$$

respectively. The support of the vector $\mathbf{x}$ and its element-wise absolute value are denoted by

$$\operatorname{supp}(\mathbf{x}) \text{ and } |\mathbf{x}|, \tag{2.7}$$

respectively.

Special Vectors The N-dimensional zero vector, i. e., the vector of size N containing zeros for all elements is denoted by $\mathbf{0}_N$.

Matrices Matrices are denoted by uppercase bold-faced type, e. g.,

$$\mathbf{X}. \tag{2.8}$$

To denote the element of the matrix $\mathbf{X}$ that is located in the i-th row and the j-th column, the following notations are used interchangeably:

$$x_{ij} \text{ and } [\mathbf{X}]_{ij}\,. \tag{2.9}$$

The i-th column of $\mathbf{X}$ is denoted by

$$\mathbf{x}_i, \tag{2.10}$$

while the i-th row of $\mathbf{X}$ is denoted by

$$[\mathbf{X}]_{i:}. \tag{2.11}$$

The transpose, element-wise complex conjugate and conjugate transpose of the matrix $\mathbf{X}$ are given by

$$\mathbf{X}^{\mathrm{T}}, \mathbf{X}^{*}, \text{ and } \mathbf{X}^{\mathrm{H}}, \tag{2.12}$$

respectively. The element-wise absolute value of the matrix $\mathbf{X}$ and its kernel (nullspace) are denoted by

$$|\mathbf{X}| \text{ and } \ker(\mathbf{X})\,, \tag{2.13}$$

respectively, while the inverse of the matrix $\mathbf{X}$ is given by

$$\mathbf{X}^{-1}. \tag{2.14}$$

The vectorization of a matrix $\mathbf{X}$, i. e., the concatenation of its columns to a single vector is denoted by

$$\mathrm{vec}\{\mathbf{X}\}\,, \tag{2.15}$$

while the trace of the matrix $\mathbf{X}$ is denoted by

$$\mathrm{Tr}(\mathbf{X}). \tag{2.16}$$

Special Matrices The symbol $\mathbf{I}_N$ denotes the identity matrix of size $N \times N$, while the symbol $\mathbf{F}_N$ stands for the $N \times N$ discrete Fourier transform matrix.

Expected Value The expected value of a scalar random variable x is denoted by

$$\mathbb{E}[x]\,. \tag{2.17}$$

The element-wise expected values of the vector $\mathbf{x}$ and the matrix $\mathbf{X}$ are accordingly denoted by

$$\mathbb{E}[\mathbf{x}] \text{ and } \mathbb{E}[\mathbf{X}]\,, \tag{2.18}$$

respectively.

Components of Complex-Valued Expressions The real and imaginary part of a complex scalar x is denoted by

$$\mathfrak{Re}\{x\} \text{ and } \mathfrak{Im}\{x\}, \tag{2.19}$$

respectively. The element-wise real and imaginary part of the vector $\mathbf{x}$ and the matrix $\mathbf{X}$ are accordingly denoted by

$$\mathfrak{Re}\{\mathbf{x}\} \text{ and } \mathfrak{Im}\{\mathbf{x}\}, \tag{2.20}$$

and

$$\mathfrak{Re}\{\mathbf{X}\} \text{ and } \mathfrak{Im}\{\mathbf{X}\}, \tag{2.21}$$

respectively.

Norms The ℓ_p-norm of a vector $\mathbf{x}$ of size n is denoted by

$$\|\mathbf{x}\|_p. \tag{2.22}$$

Its definition is given by

$$\|\mathbf{x}\|_p = \left(|x_1|^p + |x_2|^p + \cdots + |x_n|^p\right)^{\frac{1}{p}}. \tag{2.23}$$

In the area of compressed sensing the ℓ_0-"norm", which is denoted by $\|\cdot\|_0$, is used. It is defined as the number of nonzero entries in a vector, i. e., given the definition in (2.23) the ℓ_0-"norm" of a vector $\mathbf{x}$ can be expressed as [25, Ch. 2.1]

$$\lim_{p\to 0} \|\mathbf{x}\|_p^p = \lim_{p\to 0} \sum_{i=1}^{n} |x_i|^p = |x_1|^0 + |x_2|^0 + \cdots + |x_n|^0, \tag{2.24}$$

where expressions with exponent zero are treated as follows:

$$x^0 = \begin{cases} 0 \text{ for } x = 0 \\ 1 \text{ otherwise.} \end{cases} \tag{2.25}$$

However, the ℓ_0-"norm" does not satisfy the definition of a *norm* and is usually referred to as ℓ_0-"norm" or ℓ_0-pseudonorm.

The Frobenius norm of a matrix $\mathbf{X}$ is denoted by

$$\|\mathbf{X}\|_{\mathrm{F}}. \tag{2.26}$$

Sets and Cardinality Sets are denoted by calligraphic uppercase symbols with normal font-weight, e. g.,

$$\mathcal{X}, \tag{2.27}$$

with the exception of the set of real numbers (of dimension n), the set of complex numbers (of dimension n), and the set of integers (of dimension n), which are denoted by

$$\mathbb{R}^n, \mathbb{C}^n \text{ and } \mathbb{Z}^n, \tag{2.28}$$

respectively. In the case of one-dimensional sets, the corresponding superscript may be omitted. The complement of a discrete set $\mathcal{X}$ is denoted by

$$\mathcal{X}^{\mathrm{C}}, \tag{2.29}$$

while its cardinality is denoted by

$$|\mathcal{X}|. \tag{2.30}$$

The cardinality uses the same notation as the absolute value of a scalar, i. e., the meaning of $|\cdot|$ depends on the context. The definition of a set is denoted by curly brackets, e. g.,

$$\mathcal{X} = \{x \in \mathbb{R} \mid x > 0\}. \tag{2.31}$$

The set comprises all elements of the set given before the vertical bar for which all conditions given after the vertical bar are fulfilled.

Probability Distributions The univariate uniform distribution on the interval $[a, b]$ is denoted by

$$\mathcal{U}(a, b). \tag{2.32}$$

The univariate Gaussian distribution with mean μ and variance σ^2 is denoted by

$$\mathcal{N}(\mu, \sigma^2), \tag{2.33}$$

while the multivariate Gaussian distribution with mean vector $\boldsymbol{\mu}$ and covariance matrix $\boldsymbol{\Sigma}$ is denoted by

$$\mathcal{N}(\boldsymbol{\mu}, \boldsymbol{\Sigma}). \tag{2.34}$$

The circularly-symmetric complex Gaussian distribution with mean vector $\boldsymbol{\mu}$ and covariance matrix $\boldsymbol{\Sigma}$ is denoted by

$$\mathcal{CN}(\boldsymbol{\mu}, \boldsymbol{\Sigma}). \tag{2.35}$$

The central chi-squared distribution with n degrees of freedom is denoted by

$$\chi^2_n, \tag{2.36}$$

while the non-central chi-squared distribution with n degrees of freedom and non-centrality parameter λ is denoted by

$$\chi^2_n(\lambda). \tag{2.37}$$

The symbol $\sim$ denotes that a random variable is distributed according to a given probability distribution, i. e.,

$$x \sim \mathcal{N}(0, 1) \tag{2.38}$$

expresses that x is distributed according to a standard normal distribution. Convergence in distribution is denoted by the symbol $\stackrel{\mathrm{D}}{=}$, i. e.,

$$\lim_{n \to \infty} x(n) \stackrel{\mathrm{D}}{=} \mathcal{N}(0, 1) \tag{2.39}$$

expresses that the distribution of $x(n)$ asymptotically converges to the standard normal distribution.

3 Background

This chapter serves as a brief introduction to the fundamental concepts the present work is based on. First, the spectrum sensing problem is introduced together with a selection of notable algorithms and their underlying ideas. Subsequently, the main building blocks of compressed sensing are reviewed. In the final part of this chapter, the application of compressed sensing to the spectrum sensing problem is discussed.

3.1 Spectrum Sensing

The basic spectrum sensing problem can be cast as a hypothesis test as follows. Consider a secondary system receiver sampling some frequency band, resulting in the baseband signal $x(t)$. To make a statement about the band's occupancy, it has to be decided which of the following two hypotheses is true:

$$\begin{aligned} \mathcal{H}_0 : x(t) &= \eta(t), \\ \mathcal{H}_1 : x(t) &= s'(t) + \eta(t), \end{aligned} \tag{3.1}$$

where $\eta(t)$ denotes receiver noise and $s'(t)$ stands for a primary user signal after propagation effects.

The discrete-time measurements used as the input of spectrum occupancy detectors are sampled from one of two different probability distributions (PDs) depending on whether $\mathcal{H}_0$ or $\mathcal{H}_1$ is true. Realizations of the detectors can be classified as either state detectors or change detectors. State detectors determine the current occupancy *state* and thus assume the samples to be distributed according to a homogeneous distribution, i. e., the PD the samples are drawn from does not change throughout the process of detection.

The category of state detectors can again be divided into two types: block detectors, also called fixed sample size (FSS) detectors and sequential detectors [26]. FSS detectors take a predefined number of samples and make their best effort to determine the band's occupancy from these. Since the sample size is fixed and independent of how easily the signal might be detected, this type of detector typically takes more samples than necessary as to become robust against, e. g., low signal-to-noise ratios (SNRs). Sequential detectors on the other hand aim at making a decision from as few samples as possible, such that the observation time necessary is minimized. To accomplish this, they continuously try to decide about the presence of a primary user signal. If one decision attempt

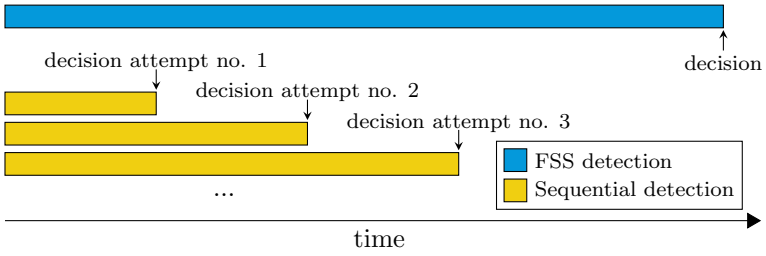

Figure 3.1: State detection. The blocks represent the samples considered in a decision.

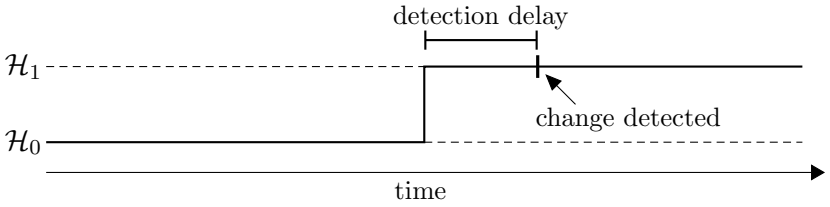

Figure 3.2: Change detection.

is inconclusive, another attempt is made after taking more samples. Figure 3.1 visualizes the difference between the two types of state detectors.

Change detectors work on a different premise. They expect the spectral band's occupancy state to change during the observation time. At the time of the disruption, the samples stop being drawn from the PD of one of the hypotheses and start being drawn from the PD of the other hypothesis, as depicted in Figure 3.2. The detector tries to notice when the PU either begins using its spectrum or stops using its spectrum. Minimizing the time between an event happening and its detection, i. e., the detection delay, is the objective of quickest detection (QD) [27, 28].

This work focuses on FSS detectors.

3.1.1 Binary Hypothesis Testing

In the following, the fundamental properties of FSS detectors and the accompanying hypothesis test is discussed. Consider a secondary system receiver that needs to decide whether a certain spectral band is occupied or free. It samples the baseband signal $x(t)$ uniformly with a sampling period T_e. This results in the vector of discrete-time samples $\mathbf{x} \in \mathbb{C}^N$, where

$$\mathbf{x} = [x(0), x(T_e), \ldots, x((N-1)T_e)]^{\mathrm{T}}. \tag{3.2}$$

Equation (3.1) can be rewritten in terms of $\mathbf{x}$ as

$$\begin{aligned} \mathcal{H}_0 : \mathbf{x} &= \boldsymbol{\eta}, \\ \mathcal{H}_1 : \mathbf{x} &= \mathbf{s}' + \boldsymbol{\eta}, \end{aligned} \tag{3.3}$$

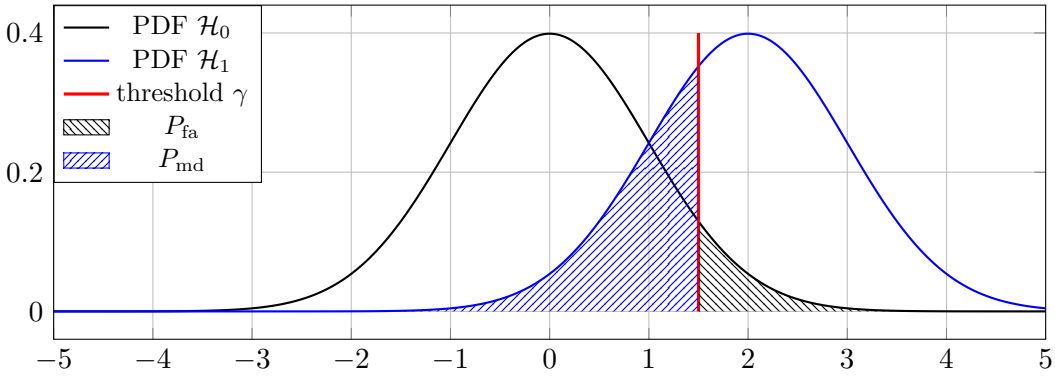

Figure 3.3: Threshold design in FSS detection.

where

$$\boldsymbol{\eta} = [\eta(0), \eta(T_e), \ldots, \eta((N-1)T_e)]^{\mathrm{T}} \tag{3.4}$$

denotes the sampled receiver noise and

$$\mathbf{s}' = [s'(0), s'(T_e), \ldots, s'((N-1)T_e)]^{\mathrm{T}} \tag{3.5}$$

stands for the sampled primary user signal after propagation effects. In order to arrive at a decision, the sensor computes a test statistic $\mathcal{T}(\mathbf{x}) : \mathbb{C}^N \to \mathbb{R}$ and compares it to a threshold γ, i. e.,

$$\mathcal{T}(\mathbf{x}) \underset{\mathcal{H}_1}{\overset{\mathcal{H}_0}{\lessgtr}} \gamma. \tag{3.6}$$

If the value of $\mathcal{T}(\mathbf{x})$ is below the threshold, the sensor decides that $\mathcal{H}_0$ is true, i. e., that the observed band is free and can be used by the secondary system. If it is above the threshold, it decides that $\mathcal{H}_1$ is true, which means that the secondary system has to refrain from accessing the band.

The threshold γ is a design parameter of the system. To gain an intuition about how the choice of the threshold impacts the system behavior, consider Figure 3.3. The figure shows two probability density functions (PDFs). The black line represents the PDF of the test statistic in the $\mathcal{H}_0$ case, while the blue line represents the PDF of the test statistic in the $\mathcal{H}_1$ case. Clearly, it is impossible never to make wrong decisions in this situation since the PDFs overlap. There are two quantities, corresponding to the two possible types of decision errors, resulting from the choice of the threshold. The probability of false alarm (P_{fa}), or false alarm rate, which is indicated by the black-shaded area and the probability of missed detection (P_{md}), or missed detection rate, which is indicated by the blue-shaded area. These two quantities are formally defined as

$$\begin{aligned} P_{\text{md}} &= P(\mathcal{H}_0 \mid \mathcal{H}_1) &&= \text{prob(decide } \mathcal{H}_0 \text{ when } \mathcal{H}_1 \text{ is true)}, \\ P_{\text{fa}} &= P(\mathcal{H}_1 \mid \mathcal{H}_0) &&= \text{prob(decide } \mathcal{H}_1 \text{ when } \mathcal{H}_0 \text{ is true)}. \end{aligned} \tag{3.7}$$

In a situation where the two PDFs do not overlap, we could choose a threshold that would result in a probability of zero for both types of wrong decisions. However, in the

case that the PDFs do overlap, one can only trade off between the two types of errors by the choice of the threshold value.

In order to guarantee the PU a certain level of safeness against interruptions, and interference-free operation in his licensed band, the threshold should be set such that it results in a pre-specified missed detection rate (P_{md}), e. g., $\{1, 3, 5\}$ percent. However, in most spectrum sensing scenarios, the sensors are regarded as being *blind*, meaning they are not in possession of any prior information about the PU transmitter and the signal it emits, i. e., they do not know about the signal type, the transmission power or the channel gain / receive SNR. Thus, the $\mathcal{H}_1$ PDF is completely unknown to the sensor, making it impossible to know which threshold to choose in order to achieve an intended P_{md}. The $\mathcal{H}_0$ PDF, however, is independent of the PU and is thus known (up to a certain accuracy [29, 30, 31]). Knowing the $\mathcal{H}_0$ PDF, the secondary system sensor can set a threshold that leads to a pre-specified P_{fa}. A detector featuring a $\mathcal{H}_0$ PDF that is asymptotically independent of any unknown parameters is called a constant false alarm rate (CFAR) detector [32, Ch. 6.5]. CFAR is a very attractive feature of a detector since it allows to set a threshold leading to an exact P_{fa} without exactly knowing the system parameters, e. g., the receiver noise power. However, as shown in [30] and [31], there is little hope of any detector truly having the CFAR property.

The goal of designing a good test statistic $\mathcal{T}(\mathbf{x})$ for spectrum sensing is to achieve maximum separateness of the two PDFs, i. e., minimum overlap, for all possible observed signals $\mathbf{x}$. A typical graphical plot illustrating the performance of a test statistic and the associated binary classifier system is the receiver operating characteristic (ROC). The ROC plots the detection rate (P_{d}) over the false alarm rate (P_{fa}). Each point on the curve corresponds to a different value of the threshold γ. Note, that the detection rate, or probability of detection, is given by $P_{\mathrm{d}} = 1 - P_{\mathrm{md}}$. An example of a ROC curve (showing the situation from Figure 3.3) is given in Figure 3.4. The closer the curve gets to the top left corner, the better the detector.

A number of test statistics for the problem of spectrum sensing have been proposed in the literature [33, 34, 35]. Based on the amount of information about the primary user signal incorporated, these solutions can be classified into the following three categories: *energy detection*, *feature detection* and *matched filter detection*. While energy detectors [36] do not make use of any prior knowledge in regard to the primary user's signal, matched filter detectors [32, Ch. 4.3] need to know the exact waveform of at least part of the signal emitted by the PU, typically a pilot or preamble. Feature detectors are an in-between, as they only make assumptions about structural or statistical properties of the signal. A number of stochastic features which are present in communication signals but are not present in pure noise have been identified. Spectrum sensing algorithms based on these have to decide if some feature is present in the measurements or not. If the feature can be found in the samples, a primary user signal is present and the secondary system should refrain from accessing the channel. However, if the feature cannot be found, the secondary system is free to make use of the spectral band it has sensed. In the following, some state-of-the-art spectrum sensing detectors are reviewed.

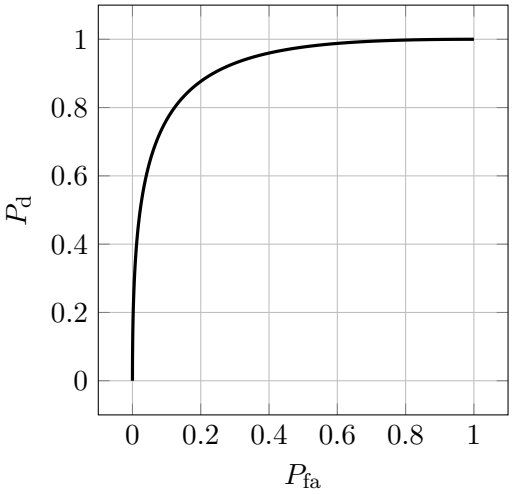

Figure 3.4: ROC curve.

3.1.2 Detectors

Energy Detection One of the most basic detection techniques is the well-known energy detector [36, 29], also known as radiometer. It determines the energy present in a block of samples and compares it to a predetermined threshold in order to decide whether a PU signal exists or whether what has been sensed is pure noise. For a known receiver noise power σ^2 this yields the Neyman-Pearson optimal binary hypothesis test [37]

$$\mathcal{T}_\mathrm{energy}(\mathbf{x}) = \frac{\|\mathbf{x}\|_2^2}{\sigma^2} \underset{\mathcal{H}_1}{\overset{\mathcal{H}_0}{\lessgtr}} \gamma. \tag{3.8}$$

The energy detector does not assume or exploit any knowledge about the PU signal's structure. If both PDFs of the test statistic, under $\mathcal{H}_0$ and under $\mathcal{H}_1$ are known, it can be shown that the performance of the energy detector comes close to that of the optimal detector under certain conditions [38]. Also, the energy detector has a very low computational complexity, which makes it an attractive choice for constrained environments, e. g., sensor networks built from low cost devices.

However, in the case of imperfect knowledge regarding the noise power σ^2, the detection performance degrades considerably, leading to so-called SNR-Walls [30]. This means that for a given amount of noise-uncertainty, there exists a value for the SNR below which robust detection is impossible. In this situation, the detector cannot decide between $\mathcal{H}_0$ with an underestimated noise power and $\mathcal{H}_1$ with an overestimated noise power. In order to facilitate reliable spectrum sensing, PU signals have to be detected in very low SNR regimes [38, 39]. The energy detector may not be able to guarantee this depending on the uncertainty in the receiver noise estimation. If the receiver noise power σ^2 is completely unknown, no appropriate threshold can be determined and thus the energy

detector cannot be used at all. Chapter 6 of this thesis is concerned with the topic of energy detection.

Cyclostationarity Detection Another way of probing a spectral band's occupancy status is to test for the presence of cyclostationarity. This method exploits the fact that most man-made signals vary periodically with time [40] and can thus be characterized as cyclostationary. Although the data contained in a modulated signal may be the output of a purely stationary random process, the coupling with sine wave carriers, pulse trains, repeating, spreading, hopping sequences and cyclic prefixes going along with the signal modulation causes a built-in periodicity [41]. Thus, virtually all waveforms used in wireless communications possess this feature. The underlying periodicity can be exploited for detecting the presence of a signal despite contamination with noise [15, 42, 43].

One of the algorithms for detecting the presence of cyclostationarity in a signal is the *time-domain test (TDT)* as detailed in [15]. The test can decide between the presence and absence of cyclostationarity for a pre-specified cycle frequency α. It is based on the cyclic autocorrelation (CA) which, given an observed signal $x(t)$, is determined by [40]

$$R_x^\alpha(\tau) = \lim_{T\to\infty} \frac{1}{T} \int_{-T/2}^{T/2} x(t+\tau/2)x^*(t-\tau/2)e^{-j2\pi\alpha t}\,\mathrm{d}t \tag{3.9}$$

for a cycle frequency α and a delay τ. For purely stationary signals $R_x^\alpha(\tau) = 0$ for all $\alpha \neq 0$, while for cyclostationary signals $R_x^\alpha(\tau) \neq 0$ for some $\alpha \neq 0$. The frequencies α with nonzero CA coefficients are called cycle frequencies. The set of cycle frequencies caused by one of potentially multiple incommensurate second-order periodicities in a cyclostationary signal comprises the periodicity's fundamental cycle frequency (the reciprocal of the fundamental period) as well as its harmonics (integer multiples).

Given the above information, the hypotheses from (3.1) can be rewritten as

$$\begin{aligned} \mathcal{H}_0 &: \forall\{\alpha \in \mathbb{R} \mid \alpha \neq 0\} : R_x^\alpha(\tau) = 0, \\ \mathcal{H}_1 &: \exists\{\alpha \in \mathbb{R} \mid \alpha \neq 0\} : R_x^\alpha(\tau) \neq 0. \end{aligned} \tag{3.10}$$

Testing for PU activity using the cyclostationarity feature comes down to evaluating (3.9) and testing if $R_x^\alpha(\tau) \neq 0$ for some $\alpha \neq 0$. If there are $\alpha \neq 0$ with nonzero coefficients, the band is occupied. Otherwise, it is free and can be used by the secondary user. Note that in a real scenario with a finite number of samples, only an estimation of $R_x^\alpha(\tau)$ is available, requiring a more sophisticated detection algorithm, e. g., the TDT from [15]. The TDT as well as the accompanying discrete-time estimation of the CA are presented in Chapter 4.

The omnipresence of cyclostationarity in wireless communication signals makes the stochastic feature a good candidate for spectrum sensing. However, using the classical TDT, the sensor has to have prior knowledge about the cycle frequency α, which

makes the detector non-blind. A method for circumventing this shortcoming is proposed in Chapter 4. Although cyclostationarity detectors cannot be considered to exhibit the CFAR property [31], some of them, e. g., the TDT, are independent of the receiver noise power in contrast to the energy detector. Due to the required evaluation of the CA, however, the TDT exhibits a considerably higher computational complexity than the energy detector.

Covariance- / Eigenvalue-Based Detection Another class of feature detectors used in spectrum sensing are covariance-based detectors, several of which have been proposed in the literature, e. g., [44, 16, 45, 46, 47, 48]. These algorithms exploit the properties of a signal's covariance matrix in order to detect primary user activity.

The statistical covariance matrix of the received signal vector $\mathbf{x}$ taken at a secondary system receiver is defined by

$$\begin{aligned}\boldsymbol{\Sigma}_{\mathbf{x}} &= \mathbb{E}\left[\mathbf{x}\mathbf{x}^{\mathrm{H}}\right] \\ &= \mathbf{H}\boldsymbol{\Sigma}_{\mathbf{s}}\mathbf{H}^{\mathrm{H}} + \boldsymbol{\Sigma}_{\boldsymbol{\eta}} \\ &= \mathbf{H}\boldsymbol{\Sigma}_{\mathbf{s}}\mathbf{H}^{\mathrm{H}} + \sigma^2\mathbf{I}_N,\end{aligned} \tag{3.11}$$

where $\boldsymbol{\Sigma}_{\mathbf{s}} = \mathbb{E}\left[\mathbf{s}\mathbf{s}^{\mathrm{H}}\right]$ and $\boldsymbol{\Sigma}_{\boldsymbol{\eta}} = \mathbb{E}\left[\boldsymbol{\eta}\boldsymbol{\eta}^{\mathrm{H}}\right]$ denote the statistical covariance matrices of the PU signal and the additive noise respectively. The noise variance is denoted by σ^2, while $\mathbf{H}$ stands for the channel gain matrix. Finally, the symbol $\mathbf{s}$ denotes the primary user signal before the effects of the communication channel.

Here we make the standard assumption that both the signal and the noise are zero-mean. Note that the last step in (3.11) is due to the noise being i.i.d. and the fact that the noise is not correlated with the signal.

Equation (3.11) provides the definition of the statistical received signal covariance matrix for the $\mathcal{H}_1$ case, i. e., when a PU signal is present. In the case of an unoccupied channel ($\mathcal{H}_0$), the PU signal vector $\mathbf{s} = \mathbf{0}$ such that only the noise part remains, i. e., $\boldsymbol{\Sigma}_{\mathbf{x}} = \sigma^2\mathbf{I}_N$. This relationship can be exploited for determining a band's occupancy status. More specifically, the hypotheses from (3.1) can be rewritten in terms of $\boldsymbol{\Sigma}_{\mathbf{x}}$ as

$$\begin{aligned}&\mathcal{H}_0 : \boldsymbol{\Sigma}_{\mathbf{x}} = \mathbf{H}\boldsymbol{\Sigma}_{\mathbf{s}}\mathbf{H}^{\mathrm{H}} + \sigma^2\mathbf{I}_N, \\ &\mathcal{H}_1 : \boldsymbol{\Sigma}_{\mathbf{x}} = \sigma^2\mathbf{I}_N.\end{aligned} \tag{3.12}$$

The above distinction gives rise to a multitude of possible approaches. A very basic spectrum sensing algorithm based on the above properties would be a detector checking if there are nonzero entries outside of the diagonal of the covariance matrix $\boldsymbol{\Sigma}_{\mathbf{x}}$. If there are, the band is occupied, otherwise it is idle. However, due to the finite amount of samples available to the detection algorithms, they have to work on the *sample* covariance matrix $\hat{\boldsymbol{\Sigma}}_{\mathbf{x}}$, which is the estimation of the statistical covariance matrix from the N available samples contained in the vector $\mathbf{x}$. Depending on N, this can be a very rough estimation. Of course no entry of $\hat{\boldsymbol{\Sigma}}_{\mathbf{x}}$ is exactly zero, which renders the above naive

approach for signal detection impractical. Usable approaches have to employ a more sophisticated method of discerning between $\mathcal{H}_0$ and $\mathcal{H}_1$.

Different directions are taken in the family of covariance-based detectors. Some directly work on $\hat{\mathbf{\Sigma}}_{\mathbf{x}}$, e. g., [44, 47]. Others base their tests on the eigenvalues of $\hat{\mathbf{\Sigma}}_{\mathbf{x}}$, e. g., [16, 45, 46, 48]. The latter group of detectors are called eigenvalue-based detectors.

While covariance-based detectors and eigenvalue-based detectors can be called *blind* and are independent of the receiver noise power, they have a considerably higher computational complexity than the energy detector. Chapter 5 deals with eigenvalue-based detectors.

3.2 Compressed Sensing

Compressed sensing (CS) [49, 50] represents a paradigm change in the field of signal acquisition. The core aim of CS is to measure as little as necessarily required in order to obtain a signal. Conventional knowledge in the field of sampling dictates that in order to fully capture all information contained in a signal, one has to gather a full set of equidistant time-domain samples taken at a rate that is at least twice the highest frequency contained in the signal. This result is commonly called the Nyquist–Shannon sampling theorem [51, 52, 53].

The CS theory asserts that for certain kinds of signals and given certain sampling modalities, a signal can be recovered from far fewer samples than demanded by the Nyquist-Shannon sampling rate. The basic compressed sensing problem is defined as follows. Consider the under-determined system of linear equations

$$\mathbf{y} = \mathbf{A}\mathbf{x}, \tag{3.13}$$

where $\mathbf{y} \in \mathbb{C}^m$, $\mathbf{x} \in \mathbb{C}^N$ and $\mathbf{A} \in \mathbb{C}^{m \times N}$ with $m \ll N$. The goal is to recover $\mathbf{x}$ from $\mathbf{y}$ with $\mathbf{A}$ known. Since the system of equations is under-determined, this problem is of course impossible to solve in general. However, if the two fundamental prerequisites of CS are fulfilled, the original signal $\mathbf{x}$ can be recovered.

Splitting up the matrix $\mathbf{A}$ into the measurement matrix $\mathbf{\Phi} \in \mathbb{C}^{m \times N}$ and the full-rank representation matrix $\mathbf{\Psi} \in \mathbb{C}^{N \times N}$ such that $\mathbf{A} = \mathbf{\Phi}\mathbf{\Psi}$, the fundamental requirements for CS to work can be stated as follows.

- The signal to be sampled needs to exhibit a low complexity, i. e., it needs to be either sparse or compressible when expressed in some representation basis $\mathbf{\Psi}$. The *sparsity* and *compressibility* properties are properly introduced in Section 3.2.1.
- The sampling basis $\mathbf{\Phi}$ and the representation basis $\mathbf{\Psi}$ need to be incoherent. The *incoherence* property is properly introduced in Section 3.2.3.

Given these two conditions and a sufficient number of samples $m \ll N$, $\mathbf{x}$ can be recovered from $\mathbf{y}$. In the following subsections, the conditions as well as efficient recovery algorithms are discussed.

3.2.1 Sparsity and Compressibility

Sparsity is a property which indicates that most of a signal's components are zero. Many real-world signals are well approximated by their sparse counterparts, i. e., when expressed in a suitable basis, removing all but the largest signal components does not lead to the loss of much of the signal's information content. These kinds of signals are called *compressible*. The fact that many real-world signals are of this type is the basis for some of the most widely used lossy compression algorithms like, e. g., the Joint Photographic Experts Group (JPEG) and the Moving Picture Experts Group (MPEG) standards for images and videos, respectively.

A vector $\mathbf{x} \in \mathbb{C}^N$ is called s-sparse if

$$\|\mathbf{x}\|_0 = |\{j | x_j \neq 0\}| \leq s, \tag{3.14}$$

i. e., if it has at most s nonzero entries [25, Ch. 2.1]. If it is not exactly sparse, it may still exhibit a weaker albeit useful property termed *compressibility*. The vector $\mathbf{x}$ can informally be called compressible if its *best s-term approximation error*, which is defined by

$$\sigma_s(\mathbf{x})_p = \inf \left\{ \|\mathbf{x} - \mathbf{z}\|_p , \mathbf{z} \in \mathbb{C}^N \text{ is } s\text{-sparse} \right\} \tag{3.15}$$

for $p > 0$ decays quickly in s. The infimum is achieved by an s-sparse vector $\mathbf{z}$ that equals the vector $\mathbf{x}$ at its s largest entries [25, Ch. 2.1].

To gain an intuition of why the notion of compressibility is interesting consider a picture taken with a camera. These kinds of pictures typically have the property that most of their energy is concentrated in a few discrete cosine - or wavelet coefficients, which means that they are compressible. File formats like JPEG exploit this fact and compress these signals by only storing the largest few of said coefficients. This kind of compression is lossy but as we know from everyday consumer systems, it does not noticeably degrade the image quality.

3.2.2 Algorithms for Sparse Recovery

Consider the problem of sparse recovery given the underdetermined system of linear equations (3.13) again. We assume the signal $\mathbf{x}$ is s-sparse and $s < m \ll N$. If the support of $\mathbf{x}$ (i. e., the set of the locations of the nonzero entries of $\mathbf{x}$) was known prior to the sensing procedure, the matrix $\mathbf{A}$ could be reduced to the columns corresponding to the support of $\mathbf{x}$, which would render the system of linear equations overdetermined. The signal $\mathbf{x}$ could then be obtained by conducting the standard least-squares approach.

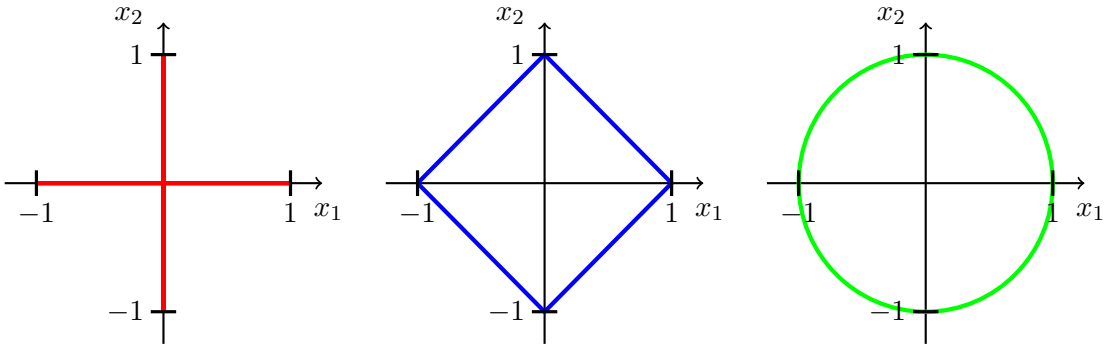

Figure 3.5: Two-dimensional unit norm balls of the ℓ_0-"norm" (red), the ℓ_1-norm (blue) and the ℓ_2-norm (green) respectively. While the ℓ_0-"norm" ball is not convex, both, the ℓ_1-norm ball and the ℓ_2-norm ball are. The ℓ_1-norm is the *tightest convex* relaxation of the ℓ_0-"norm".

The same approach is viable if the signal $\mathbf{x}$ is not s-sparse but compressible with most of the energy allocated to a known set of s entries of $\mathbf{x}$. The above sensing procedure would be an efficient, resource friendly way of obtaining $\mathbf{x}$ compared to the traditional approach of taking the full set of N samples to obtain the N entries of $\mathbf{x}$ only to then throw away all but the s nonzero / high-energy entries in the compression step.

As described above, sparse recovery with known support is trivial. The problem considered in CS is a more involved one. In CS, the support of $\mathbf{x}$ is considered to be unknown prior to the sensing procedure. Since in this case the underdetermined system of linear equations cannot be reduced to an overdetermined one, a method has to be devised to select the actual signal vector $\mathbf{x}$ out of the infinite set of possible solutions that are consistent with the system of equations. A wealth of algorithms that tackle this problem have been proposed in the literature. Some of these are introduced in the following.

Basis Pursuit (BP) The first approach that comes to mind is to exploit the signal's sparsity by choosing the vector $\mathbf{x}$ which has the smallest number of nonzero entries among all solutions to (3.13), i. e., the *sparsest* one. This is equivalent to choosing the vector with the lowest ℓ_0-"norm". The optimization problem representing the above approach is given by

$$\begin{aligned} \min_{\mathbf{x}\in\mathbb{C}^N} \quad & \|\mathbf{x}\|_0 \\ \text{s.t.} \quad & \mathbf{y} = \mathbf{A}\mathbf{x}. \end{aligned} \tag{3.16}$$

Unfortunately, this approach is a poor fit for signal acquisition, especially for large signals, i. e., for large N, since in general ℓ_0-minimization is NP-hard.

Replacing the ℓ_0-"norm" in the objective by its tightest convex relaxation (cf. Figure 3.5), the ℓ_1-norm, renders the problem convex and thus tractable. One of the most important results in the field of CS is that *for most large underdetermined systems of linear equations the minimal ℓ_1-norm solution is also the sparsest solution* [54]. The

corresponding optimization problem, which goes by the name basis pursuit (BP) [55] or simply ℓ_1-minimization is given by

$$\begin{aligned} \min_{\mathbf{x}\in\mathbb{C}^N} \quad & \|\mathbf{x}\|_1 \\ \text{s.t.} \quad & \mathbf{y} = \mathbf{A}\mathbf{x}. \end{aligned} \tag{3.17}$$

Since in many engineering disciplines one cannot hope for perfect noise-free measurements, the linear samples taken by a sensor are better described by

$$\mathbf{y}' = \mathbf{A}\mathbf{x} + \mathbf{e}, \tag{3.18}$$

where $\mathbf{e}$ contains random noise. To recover the original signal vector $\mathbf{x}$ from the noisy measurements $\mathbf{y}'$, a noise-aware version of BP called *quadratically constrained basis pursuit (QCBP)* can be employed. It is given by

$$\begin{aligned} \min_{\mathbf{x}\in\mathbb{C}^N} \quad & \|\mathbf{x}\|_1 \\ \text{s.t.} \quad & \|\mathbf{A}\mathbf{x} - \mathbf{y}'\|_2 \leq \epsilon, \end{aligned} \tag{3.19}$$

where ϵ limits the amount of noise the optimization problem solver expects the samples to contain. It is very similar to (but not to be confused with) *basis pursuit denoising (BPDN)* [25, Ch. 3.1].

Orthogonal Matching Pursuit (OMP) As an alternative to convex optimization, different greedy algorithms for recovering the original signal vector have been proposed in the literature. One of them is called orthogonal matching pursuit (OMP) [13, 14]. It is formally defined in Algorithm 1.

Algorithm 1: Orthogonal matching pursuit (OMP)

Input: $\mathbf{y} \in \mathbb{C}^m$, $\mathbf{A} \in \mathbb{C}^{m\times N}$, n_{iter}

1 $\mathbf{x}_0 = \mathbf{0}, S_0 = \emptyset$;

2 **for** $i = 1, \ldots, n_{iter}$ **do**

3 $\quad \mathbf{c}_i = \mathbf{A}^{\mathrm{H}}(\mathbf{y} - \mathbf{A}\mathbf{x}_{i-1})$;

4 $\quad j_i = \underset{j\in\{1,\ldots,N\}}{\operatorname{argmax}} \left\{ \left| [\mathbf{c}_i]_j \right| \right\}$;

5 $\quad S_i = S_{i-1} \cup \{j_i\}$;

6 $\quad \mathbf{x}_i = \underset{\mathbf{z}\in\mathbb{C}^N}{\operatorname{argmin}} \{ \|\mathbf{y} - \mathbf{A}\mathbf{z}\|_2 , \operatorname{supp}(\mathbf{z}) \subset S_i \}$;

Output: $\mathbf{x}_{n_{\text{iter}}} \in \mathbb{C}^N$

The algorithm iteratively determines the support of the signal vector that is to be acquired. Given the obtained support with a cardinality lower than the number of samples m (the signal is assumed to be sparse), the underdetermined system of linear equations (3.13) can be reduced to an overdetermined system, which can be solved using a standard least-squares approach.

In line 1, the signal vector $\mathbf{x}$ is initialized to the all-zero vector and the support set S is initialized to the empty set. The loop that starts in line 2 iterates over the signal support. Each iteration, one index is added to the support set S. The stopping condition used in Algorithm 1 is the number of iterations n_{iter} that the algorithm is supposed to execute. Obviously, this number should be at least as high as the expected signal sparsity, i. e., the expected number of nonzero entries in $\mathbf{x}$. Since this number is not necessarily known before signal recovery, the stopping criterion can alternatively be replaced by a maximum residual energy $\epsilon_{\max}$. In that case, the for-loop is replaced by a while-loop given by [**while** $\|\mathbf{y} - \mathbf{A}\mathbf{x}_{i-1}\|_2^2 \geq \epsilon_{\max}$ **do**].

In line 3 the residual of the previous iteration ($\mathbf{y} - \mathbf{A}\mathbf{x}_{i-1}$) is correlated with the so-called atoms contained in the matrix $\mathbf{A}$. The index of the atom with the strongest correlation is chosen in line 4. It is added to the support set in line 5. In line 6 the signal $\mathbf{x}$ is expressed as accurately as possible in a squared-error sense given the part of the support set determined so far (S_i). In the subsequent iteration, the algorithm tries to determine which atom can best explain the residuum of the i-th iteration, i. e., the part of the samples that could not be expressed with the atoms corresponding to the indices contained in S_i. Since the cardinality of S always stays well below the number of samples m, the optimization problem in line 6 always solves an overdetermined system of equations.

Other Recovery Algorithms Due to the high popularity of CS, many sparse recovery algorithms spanning a number of categories have been developed. A non-comprehensive list of notable algorithms is given in the following. Besides OMP, one of the most popular greedy methods is the compressive sampling matching pursuit (CoSaMP) [56]. In addition to optimization methods and greedy methods, an important category of sparse recovery algorithms are thresholding-based methods. Notable contenders in this category are basic thresholding, iterative hard thresholding (IHT), hard thresholding pursuit (HTP), and subspace pursuit [25, Ch. 3.3].

3.2.3 Recovery Conditions

As discussed above, the unknown support of $\mathbf{x}$ assumed in CS renders the recovery problem underdetermined. This means that even for sparse $\mathbf{x}$, one cannot hope for successful recovery by any means using an arbitrary matrix $\mathbf{A}$. In the following, we present desirable properties for $\mathbf{A}$ and their implications for signal recovery as well as their consequences for the design of CS matrices.

Null Space Property (NSP) The null space property [57], [25, Ch. 4.1] is defined as follows. A matrix $\mathbf{A}$ satisfies the null space property relative to a set $\mathcal{S} \subset \{1, 2, \ldots, N\}$ if

$$\|\mathbf{v}_{\mathcal{S}}\|_1 < \|\mathbf{v}_{\mathcal{S}^{\mathrm{C}}}\|_1 \text{ for all } \mathbf{v} \in \ker(\mathbf{A}) \setminus \{\mathbf{0}\}. \tag{3.20}$$

Furthermore, $\mathbf{A}$ satisfies the null space property (NSP) of order s if it satisfies the NSP relative to any set $\mathcal{S} \subset \{1, 2, \ldots, N\}$ with $|\mathcal{S}| \leq s$. Roughly speaking, the NSP states that the nullspace of $\mathbf{A}$ should contain neither sparse nor highly compressible vectors. The NSP constitutes a necessary and sufficient condition for the exact recovery of all s-sparse vectors via BP.

Restricted Isometry Property (RIP) The NSP provides guarantees for the exact recovery of *sparse* signals. However, since the signals in most engineering applications contain noise and can thus be classified as *compressible* rather than *sparse*, it is desirable to have matrix properties guaranteeing the successful recovery of *compressible* signals. The restricted isometry property [58] provides exactly this. It is defined as follows [59, Ch. 1.4.2]. A matrix $\mathbf{A}$ satisfies the restricted isometry property (RIP) of order s if there exists a $\delta_s \in (0, 1)$ such that

$$(1 - \delta_s) \|\mathbf{x}\|_2^2 \leq \|\mathbf{A}\mathbf{x}\|_2^2 \leq (1 + \delta_s) \|\mathbf{x}\|_2^2 \tag{3.21}$$

holds for all s-sparse $\mathbf{x}$. Roughly speaking, the RIP guarantees that the distance between sparse vectors is preserved under the transformation through $\mathbf{A}$. If a matrix satisfies the RIP, this implies that it also satisfies the NSP. The smaller δ_s, the better a matrix is suited for sparse recovery. Given a sufficiently small constant δ_s, the RIP has been shown to guarantee successful recovery of compressible signals with a multitude of algorithms, i. e., BP, IHT, HTP, OMP and CoSaMP [25, Ch. 6].

Coherence Although the NSP and the RIP provide strong recovery guarantees, they are impractical when it comes to assessing the suitability of a matrix for CS. The reason for this is that verifying that a matrix satisfies any of these properties is generally NP-hard [60]. Thus it is often desirable to evaluate the so-called coherence of a matrix, which is a quicker to compute albeit weaker indicator of fitness for sparse recovery. The coherence of a matrix $\mathbf{A}$ is given by [59, Ch. 1.4.3]

$$\mu(\mathbf{A}) = \max_{1 \leq i < j \leq N} \frac{\left|\mathbf{a}_i^{\mathrm{T}} \mathbf{a}_j\right|}{\|\mathbf{a}_i\|_2 \|\mathbf{a}_j\|_2}, \tag{3.22}$$

i. e., it is the largest absolute inner product between any two columns of $\mathbf{A}$. As with the RIP constant δ_s, a smaller coherence generally leads to a better recovery performance.

Matrix Construction and Required Number of Samples Constructing explicit matrices that fulfill the RIP and are free of major shortcomings seems to be a hard problem. Indeed, it remains an open problem to construct explicit matrices that are provably optimal for CS (regarding s, m, and N) [25, Ch. 1.1]. Luckily, random matrices have proven to be an effective workaround. The two most popular classes are Gaussian and Bernoulli matrices. Gaussian matrices are constructed by independently drawing each

entry from a standard normal distribution, while Bernoulli matrices are built by independently drawing each entry from the set $\{-1, 1\}$, where either option is drawn with a probability of 0.5. Matrices from both classes have been shown to satisfy the RIP with high probability for a certain amount of samples, i. e., for a high enough m. A key result derived from this fact is that using a Gaussian or Bernoulli matrix, all s-sparse vectors can be reconstructed using a variety of algorithms if

$$m \geq Cs \ln(N/s), \tag{3.23}$$

where C is a constant that is independent of s, m, and N. The above bound is optimal.

In engineering scenarios the structure of the problem often influences or even dictates the choice of a matrix. An example that appears in many applications is the random partial Fourier matrix. This matrix is constructed by uniformly selecting a set of m rows of the $N \times N$ discrete Fourier transform (DFT) matrix at random. The random partial Fourier matrix fits into the category of structured random matrices and while it is not as well suited for sparse recovery as the fully random Gaussian and Bernoulli matrices, it constitutes an effective option in situations where the choice of the matrix is restricted. Given a certain number of rows, the random partial Fourier matrix can be shown to satisfy the RIP with high probability [25, Ch. 12.6]. Thus, guarantees similar to (3.23) can be given for this type of matrix.

3.3 Compressed Sensing in Spectrum Sensing

In spectrum sensing there are two instances where high amounts of redundant data create technical problems. The first one arises when a secondary receiver tries to sense a band with a very large bandwidth. Sampling a wide band is of great interest to the secondary system, since the more bandwidth is sensed, the higher the chance of finding a suitable spectrum hole, i. e., an unused portion of the spectrum. However, obeying the minimum necessary sampling rate given by the Shannon-Nyquist sampling theorem, sensing a wide band comes at a great cost to the secondary receiver. This is caused by the fact that analog-to-digital converters (ADCs) with high sampling rates are both, high in price and power hungry. Employing compressed sensing, a lot less samples have to be taken, such that a slower ADC can be used.

The other instance is related to the hidden terminal problem [61, Ch. 14.3.3], which is illustrated in Figure 3.6. The hidden terminal problem occurs when the PU signal cannot be detected at the secondary system node which senses the spectrum, but a secondary system signal would disturb a primary receiver.

To tackle this problem, the secondary system employs a number of geographically distributed sensors. The risk that none of the sensors is at a location where it can pick up the PU signal decreases with the number of sensors deployed. The process of finding a consensus about a channel's occupancy within the secondary system makes it necessary

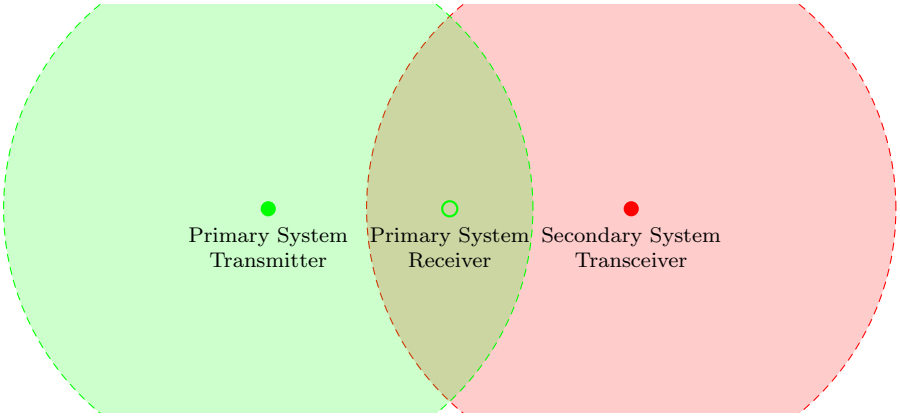

Figure 3.6: Hidden Terminal Problem.

to exchange either measurements or local decisions. In a system sharing measurements, the spectral resources used for the exchange can be minimized by getting rid of the redundancy in the data being exchanged by means of compressed sensing.

Given the underutilization of the licensed radio spectrum, the frequency spectrum of a received wideband signal can be assumed to be only sparsely occupied. This fact can be exploited when applying compressed sensing to energy detection. Since the number of periodicities in typical communication signals is small, the cyclic autocorrelation can realistically be assumed to be sparse, which facilitates the use of compressed sensing for cyclostationarity detection. In both of the above-mentioned methods, the random partial Fourier matrix plays a crucial role.

4 Cyclostationarity Detection

Although random signals are often modeled as being statistically stationary, more often than not, this is an incorrect assumption and although many statistical signal processing methods work well despite this fact, exploiting non-stationarity can result in enhanced performance [62] or, as in the case of spectrum sensing, open up whole new ways of approaching a problem. The underlying assumption of stationary signals is that the parameters of the signal-generating physical phenomenon do not change over time. However, in most man-made signals they do. This includes wireless communication signals since even if the data contained in a modulated signal is a purely stationary random process, the coupling with sine wave carriers, pulse trains, repeating, spreading, hopping sequences and cyclic prefixes going along with its modulation causes a built-in periodicity [41]. If the parameters of the physical phenomenon generating a signal, and as a consequence also the signal's statistical properties, vary cyclically with time, the signal is called cyclostationary. Wireless communication signals fall into this category and since cyclostationarity allows an SU receiver to discriminate between pure stationary noise ($\mathcal{H}_0$) and a communication signal contaminated with noise ($\mathcal{H}_1$), it is one of the stochastic features used in spectrum sensing.

In this chapter we consider the problem of *blind* cyclostationary spectrum sensing. Historically, *blind* operation has not been a feature of cyclostationarity-based algorithms. Indeed, in many application scenarios the information required for traditional cyclostationarity detection might not be available, hindering its practical applicability. We propose two new cyclostationary spectrum sensing algorithms that make use of the inherent sparsity of the cyclic autocorrelation to make blind operation possible. Along with utilizing sparse recovery methods for estimating the cyclic autocorrelation, we take further advantage of its structure by introducing joint sparsity as well as general structure dictionaries into the recovery process. Furthermore, we extend a statistical test for cyclostationarity to accommodate sparse cyclic spectra. Our numerical results demonstrate that the new methods achieve a near constant false alarm rate behavior in contrast to earlier approaches from the literature.

Parts of the present chapter are contained in [23], which is currently under review.

4.1 Motivation and Prior Work

One of the algorithms exploiting cyclostationarity for the purpose of spectrum sensing is the so called *time-domain test (TDT)* as introduced in [15]. The test can decide between

the presence and absence of cyclostationarity for a pre-specified potential cycle frequency α. It operates on the cyclic autocorrelation (CA), which, given an observed signal $x(t)$, is defined as [40]

$$R_x^\alpha(\tau) = \lim_{T\to\infty} \frac{1}{T} \int_{-T/2}^{T/2} x(t+\tau/2)x^*(t-\tau/2)e^{-j2\pi\alpha t}\,\mathrm{d}t \tag{4.1}$$

for a potential cycle frequency α and a delay τ. For purely stationary signals $R_x^\alpha(\tau) = 0$ for all $\alpha \neq 0$, while for cyclostationary signals $R_x^\alpha(\tau) \neq 0$ for some $\alpha \neq 0$. The α with non-zero CA coefficients are called cycle frequencies. The set of cycle frequencies caused by one of potentially multiple incommensurate second-order periodicities in a cyclostationary signal comprises the periodicity's fundamental cycle frequency (the reciprocal of the fundamental period) as well as its harmonics (integer multiples).

Given the above information, we can rewrite the hypothesis test (3.1) as

$$\begin{aligned} \mathcal{H}_0 &: \forall\{\alpha \in \mathbb{R} | \alpha \neq 0\} : R_x^\alpha(\tau) = 0, \\ \mathcal{H}_1 &: \exists\{\alpha \in \mathbb{R} | \alpha \neq 0\} : R_x^\alpha(\tau) \neq 0. \end{aligned} \tag{4.2}$$

Since the CA is zero on its whole support except the set of cycle frequencies and $\alpha = 0$, it can be called sparse. This sparsity can be taken advantage of for the purpose of estimating the CA employing compressed sensing methods.

Multiple contributions have been made in the field of compressive cyclostationary spectrum sensing. The authors of [63] formulate the estimation of the CA as a sparse recovery problem, which they solve using the OMP algorithm [25, Ch. 3.2]. Based on the sparse estimate of the CA, they propose two detection algorithms exploiting different CA properties. The first one, called slot comparison method (SCM), compares the biggest CA components OMP finds in two consecutive blocks of samples. If for both blocks the same discrete cycle frequencies are chosen, $\mathcal{H}_1$ is selected, otherwise $\mathcal{H}_0$ is selected. The second detection algorithm is called symmetry method (SM). It exploits the fact, that for certain types of signals, the CA is symmetric around the direct current (DC) component. Instead of the CA, the authors of [64] use the spectral correlation (SC), which can be obtained by Fourier-transforming the CA over τ, for detecting multiple transmitters in a wideband signal using CS. In order to estimate the SC from compressed samples via CS, they established a direct linear relation between the compressed samples and the SC. Based on [64], the authors of [65] derive a method for recovering the SC from sub-Nyquist samples using a reduced complexity approach, for which they provide a closed form solution. In [66], the modulated wideband converter (MWC) [67] is used to obtain the SC from sub-Nyquist samples to then apply cyclostationarity detection.

In this chapter we propose two novel CA estimation algorithms, both of which exploit *further* prior information about the CA in addition to its sparsity: the simultaneous OMP-based (SOber) and the dictionary assisted (Dice) compressive CA estimator. The first one exploits the joint sparsity of the CA vectors with regard to the time delay in

order to recover the CA matrix for all delays simultaneously, while the second one takes advantage of the signal induced structure of the CA by introducing structure dictionaries into the recovery process. In order to evaluate the performance of the proposed CA estimators we derive a closed-form expression of the CA of *sampled* linearly modulated signals with rectangular pulse shape. Furthermore, we show how the expression can be used as prior information in the dictionary assisted approach. Note, that the use of sparse recovery in the novel CA estimation approaches results in the automatic detection of a signal's cycle frequencies. This in turn allows *blind* spectrum sensing by eliminating the integral need of the classical TDT for the perfect knowledge of said cycle frequencies. However, the resulting sparse structure of the compressive CA estimates does not allow for the application of the traditional TDT since the noise statistics are missing. To compensate for this phenomenon, we develop a modified TDT and thus enable blind compressive cyclostationary spectrum sensing. Numerical tests show that the proposed method achieves a near CFAR behavior.

4.2 System Model and Classical CA Estimation

Consider a secondary system receiver that needs to decide whether a certain spectral band is occupied or free. It samples the baseband signal $x(t)$ uniformly with a sampling period T_e. This results in the vector of discrete samples $\mathbf{x}_{t_0} \in \mathbb{C}^N$, where

$$\mathbf{x}_{t_0} = [x(t_0), x(t_0 + T_e), \ldots, x(t_0 + (N-1)T_e)]^{\mathrm{T}}. \tag{4.3}$$

We assume the vector $\mathbf{x}_{t_0}$ is discrete and zero-mean and due to the nature of man-made signals it represents an (almost [68, Ch. 1.3]) cyclostationary process [15]. The presence of stochastic periodicity in the samples and thus the presence of a man-made signal can be revealed by applying a detection algorithm such as the TDT to the CA of the samples. There are different ways of obtaining the CA from the baseband samples, one of which is the following (classical) estimator

$$\hat{R}^a_{x,t_0}(\nu) = \frac{1}{N} \sum_{n=0}^{N-1-\nu} x(t_0 + nT_e) x^*(t_0 + (n+\nu)T_e) e^{-j2\pi \frac{a}{N} n} e^{-j\pi \frac{a}{N} \nu}. \tag{4.4}$$

Evaluating this function results in the CA coefficient for the cycle frequency $\alpha = \frac{a}{NT_e}$ and the time-delay $\tau = \nu T_e$, where a stands for the discrete cycle frequency and ν denotes the discrete time delay. Note that the factor $e^{-j\pi \frac{a}{N} \nu}$ remains constant throughout the sum. It is a phase shift necessary to maintain compatibility with the symmetric CA (4.1). The estimator (4.4) is biased but exhibits a smaller estimation variance than an unbiased one [15].

We define the CA vector as

$$\hat{\mathbf{r}}^{\nu}_x = [\hat{R}^0_{x,t_0}(\nu), \ldots, \hat{R}^{N-1}_{x,t_0}(\nu)]^{\mathrm{T}}. \tag{4.5}$$

Subsequently, we rewrite the estimation of the CA vector as a matrix-vector product. To do so, we need the (N element) *delay-product* with time-delay $\tau = \nu T_e$, which is given by

$$\mathbf{y}_N^\nu = \mathbf{x}_{t_0} \circ \mathbf{x}_{t_0+\nu T_e}^*, \tag{4.6}$$

where $\circ$ denotes component-wise multiplication. Note that since the receiver only takes N samples, $\mathbf{x}_{t_0+\nu T_e}^*$ is zero-padded at the end. The CA vector is now given by

$$\hat{\mathbf{r}}_x^\nu = \frac{1}{N}\mathbf{F}_N \mathbf{y}_N^\nu, \tag{4.7}$$

where $\mathbf{F}_N$ denotes the $(N \times N)$ DFT matrix. Finally, the CA matrix for time-delays $\nu_1 T_e, \ldots, \nu_{n_\nu} T_e$ is given by

$$\hat{\mathbf{R}}_x = [\hat{\mathbf{r}}_x^{\nu_1}, \ldots, \hat{\mathbf{r}}_x^{\nu_{n_\nu}}] = \frac{1}{N}\mathbf{F}_N \mathbf{Y}_N, \tag{4.8}$$

with $\mathbf{Y}_N = [\mathbf{y}_N^{\nu_1}, \ldots, \mathbf{y}_N^{\nu_{n_\nu}}]$.

4.3 The Time-Domain Test for Cyclostationarity

As mentioned in Section 4.1, the statistical CA of a cyclostationary signal is sparsely occupied, containing spikes only at the DC component as well as the cycle frequencies of inherent signal periodicities and their harmonics. Thus, given the statistical CA, one could decide between $\mathcal{H}_0$ and $\mathcal{H}_1$ by testing it for being non-zero at the signal's inherent cycle frequencies. However, instead of the statistical CA, we only have access to its estimation, the sample CA (which asymptotically converges to the statistical CA). The coefficients of the sample CA are not constant but rather follow different probability distributions, depending on whether $\mathcal{H}_0$ or $\mathcal{H}_1$ is true. In the seminal work [15], these probability distributions have been identified and a test for cyclostationarity based on this knowledge has been designed. The test is briefly described in the following.

Consider the $1 \times 2n_\nu$ vector

$$\begin{aligned}\hat{\mathbf{r}}_{xx^*}(a_0) = \Big[&\mathfrak{Re}\left\{\hat{\mathbf{R}}_x[a_0, \nu_1]\right\}, \ldots, \mathfrak{Re}\left\{\hat{\mathbf{R}}_x[a_0, \nu_{n_\nu}]\right\}, \\ &\mathfrak{Im}\left\{\hat{\mathbf{R}}_x[a_0, \nu_1]\right\}, \ldots, \mathfrak{Im}\left\{\hat{\mathbf{R}}_x[a_0, \nu_{n_\nu}]\right\}\Big],\end{aligned} \tag{4.9}$$

which represents the concatenation of the real and the imaginary part of the row of $\hat{\mathbf{R}}_x$ corresponding to the discrete cycle frequency a_0. The frequency a_0 is the cycle frequency of interest, i. e., the one for the presence of which we want to test the signal. Given this vector, we can formulate the following non-asymptotic hypotheses

$$\begin{aligned}\mathcal{H}_0 : \hat{\mathbf{r}}_{xx^*}(a_0) &= \boldsymbol{\epsilon}_{xx^*}(a_0), \\ \mathcal{H}_1 : \hat{\mathbf{r}}_{xx^*}(a_0) &= \mathbf{r}_{xx^*}(a_0) + \boldsymbol{\epsilon}_{xx^*}(a_0),\end{aligned} \tag{4.10}$$

where $\mathbf{r}_{xx^*}(a_0)$ is the deterministic but unknown asymptotic counterpart of $\hat{\mathbf{r}}_{xx^*}(a_0)$ and $\boldsymbol{\epsilon}_{xx^*}(a_0)$ is the estimation error. Note that in contrast to the hypotheses from equation (4.2), this formulation considers the presence of cyclostationarity in the received signal for *one fixed* cycle frequency a_0.

Since $\mathbf{r}_{xx^*}(a_0)$ is nonrandom, the distribution of $\hat{\mathbf{r}}_{xx^*}(a_0)$ under $\mathcal{H}_0$ and $\mathcal{H}_1$ only differs in mean. As shown in [15], the estimation error $\boldsymbol{\epsilon}_{xx^*}(a_0)$ asymptotically follows a Gaussian distribution, i. e.,

$$\lim_{N\to\infty} \sqrt{N}\boldsymbol{\epsilon}_{xx^*}(a_0) \overset{\mathrm{D}}{=} \mathcal{N}(\mathbf{0}_{2n_\nu}, \boldsymbol{\Sigma}_{xx^*}(a_0)), \tag{4.11}$$

where $\boldsymbol{\Sigma}_{xx^*}(a_0)$ is the statistical covariance matrix of $\hat{\mathbf{r}}_{xx^*}(a_0)$ and $\overset{\mathrm{D}}{=}$ denotes convergence in distribution. The covariance matrix can be computed as [15]

$$\boldsymbol{\Sigma}_{xx^*}(a_0) = \begin{bmatrix} \Re\mathfrak{e}\left\{\frac{\mathbf{Q}+\mathbf{Q}^*}{2}\right\} & \Im\mathfrak{m}\left\{\frac{\mathbf{Q}-\mathbf{Q}^*}{2}\right\} \\ \Im\mathfrak{m}\left\{\frac{\mathbf{Q}+\mathbf{Q}^*}{2}\right\} & \Re\mathfrak{e}\left\{\frac{\mathbf{Q}^*-\mathbf{Q}}{2}\right\} \end{bmatrix}, \tag{4.12}$$

where the (m,n)-th entries of the matrices $\mathbf{Q}$ and $\mathbf{Q}^*$ are given by

$$[\mathbf{Q}]_{mn} = S_{\mathbf{y}_N^{\nu_m}\mathbf{y}_N^{\nu_n}}(2a_0, a_0) \tag{4.13}$$

and

$$[\mathbf{Q}^*]_{mn} = S^*_{\mathbf{y}_N^{\nu_m}\mathbf{y}_N^{\nu_n}}(0, -a_0), \tag{4.14}$$

respectively. The term $S_{\mathbf{y}_N^{\nu_m}\mathbf{y}_N^{\nu_n}}(\cdot,\cdot)$ denotes the unconjugated, while $S^*_{\mathbf{y}_N^{\nu_m}\mathbf{y}_N^{\nu_n}}(\cdot,\cdot)$ denotes the conjugated cyclic spectrum of a signal. One way to estimate these is to determine the following frequency-smoothed periodograms:

$$\hat{S}_{\mathbf{y}_N^{\nu_m}\mathbf{y}_N^{\nu_n}}(2a_0, a_0) = \frac{1}{NL} \sum_{s=-\frac{L-1}{2}}^{\frac{L-1}{2}} W(s)\hat{\mathbf{R}}_x[a_0 - s, \nu_n]\hat{\mathbf{R}}_x[a_0 + s, \nu_m] \tag{4.15}$$

$$\hat{S}^*_{\mathbf{y}_N^{\nu_m}\mathbf{y}_N^{\nu_n}}(0, -a_0) = \frac{1}{NL} \sum_{s=-\frac{L-1}{2}}^{\frac{L-1}{2}} W(s)\hat{\mathbf{R}}^*_x[a_0 + s, \nu_n]\hat{\mathbf{R}}_x[a_0 + s, \nu_m], \tag{4.16}$$

where W is a normalized spectral window of odd length L. Looking at the equations (4.15) and (4.16), it becomes clear why the cyclic spectrum is often referred to as the spectral correlation (SC). Note, that there are different ways of obtaining the SC, one of which are the above expressions. It can also be determined by Fourier-transforming the CA over the time-delay ν (or τ depending on whether the discrete-time or the continuous-time CA is used).

Given the estimated quantities described above, the following generalized likelihood ratio (GLR) test statistic can be derived [42]

$$\mathcal{T}_{xx^*} = N\hat{\mathbf{r}}_{xx^*}(a_0)\hat{\boldsymbol{\Sigma}}^{-1}_{xx^*}(a_0)\hat{\mathbf{r}}^{\mathrm{T}}_{xx^*}(a_0). \tag{4.17}$$

The test statistic can be interpreted as a normalized energy. The inverse of the covariance matrix scales $\hat{\mathbf{r}}_{xx^*}(a_0)$ such that under $\mathcal{H}_0$ its entries follow a standard normal distribution. Thus, under $\mathcal{H}_0$, the test statistic asymptotically follows a central chi-squared distribution with $2n_\nu$ degrees of freedom, i. e., $\lim_{N\to\infty} \mathcal{T}_{xx^*} \overset{\mathrm{D}}{=} \chi^2_{2n_\nu}$, while under $\mathcal{H}_1$, the test statistic asymptotically follows a non-central chi-squared distribution with unknown non-centrality parameter λ, i. e., $\lim_{N\to\infty} \mathcal{T}_{xx^*} \overset{\mathrm{D}}{=} \chi^2_{2n_\nu}(\lambda)$. Based on the above test statistic we can design a CFAR detector with some false alarm rate P_{fa} by finding the corresponding decision threshold in the $\chi^2_{2n_\nu}$ tables. We cannot design a test based on a desired detection rate P_{d}, since although $\mathbf{r}_{xx^*}(a_0)$ is deterministic, it depends on the type of signal emitted by the transmitter as well as the SNR at the receiver, both of which are assumed to be unknown.

The classical approach for cyclostationary spectrum sensing is to apply the TDT to the CA estimate from (4.4). However, to do so one needs to know which cycle frequency to test beforehand, which eliminates the possibility of true *blind* spectrum sensing. One could sequentially test the received signal for all possible cycle frequencies. However, with high probability the estimation noise at some cycle frequency would have a value above the decision threshold, leading to a false alarm.

4.4 Simultaneous OMP CA Estimation

In this section we cast the CA estimation as a joint sparse recovery problem. Since this method is able to detect the CA's support, it removes the traditional approach's requirement of knowing the cycle frequencies beforehand, thus making truly blind cyclostationarity-based spectrum sensing possible.

We begin by rewriting equation (4.8) as

$$\mathbf{Y}_N = N\mathbf{F}_N^{-1}\hat{\mathbf{R}}_x, \tag{4.18}$$

where $\mathbf{F}_N^{-1}$ is the $(N \times N)$ inverse discrete Fourier transform (IDFT) matrix. Now consider an $m \times N$ matrix $\mathbf{M}$, which consists of a selection of m rows of the $N \times N$ identity matrix $\mathbf{I}_N$. It represents the undersampling operation. Applying $\mathbf{M}$ to (4.18), we get

$$\mathbf{Y}_m = \mathbf{M}\mathbf{Y}_N = N\mathbf{M}\mathbf{F}_N^{-1}\hat{\mathbf{R}}_x, \tag{4.19}$$

where $\mathbf{Y}_m$ contains a selection of m coefficients of the delay-products for different delays. We now want to recover $\hat{\mathbf{R}}_x$ from $\mathbf{Y}_m$ by solving the underdetermined inverse problem (4.19). To do so we exploit our knowledge about the CA's sparsity.

The straightforward solution would be to solve the following optimization problem

$$\begin{aligned} \min \quad & \left\| \mathrm{vec}\left\{\hat{\mathbf{R}}_x\right\} \right\|_0 \\ \text{s.t.} \quad & \mathbf{Y}_m = N\mathbf{M}\mathbf{F}_N^{-1}\hat{\mathbf{R}}_x, \end{aligned} \tag{4.20}$$

where $\|\cdot\|_0$ denotes the ℓ_0-"norm" [50], which is the number of non-zero entries in a vector, and vec$\{\cdot\}$ stands for the vectorization of a matrix, i. e., the concatenation of its columns to a single vector. Equation (4.20) is known to be a non-convex combinatorial problem [50]. One way to solve it within a practically feasible amount of time is to substitute the ℓ_0-"norm" by its tightest convex relaxation, the ℓ_1-norm. With high probability, this produces the same result since for most large underdetermined systems of linear equations the minimal ℓ_1-norm solution is also the sparsest solution [54]. Another way of solving (4.20) efficiently is applying one of the many greedy sparse recovery algorithms that have been developed in the field of CS, such as, e. g., orthogonal matching pursuit (OMP).

OMP (cf. Algorithm 1 in Section 3.2.2) is a greedy algorithm that iteratively determines a vector's support from an underdetermined system of linear equations and subsequently recovers the vector by solving a least-squares problem. Using it, we could solve (4.20) for each column of $\hat{\mathbf{R}}_x$ individually (as in [63]), i. e., we could solve

$$\begin{aligned} \min \quad & \|\hat{\mathbf{r}}_x^{\nu}\|_0 \\ \text{s.t.} \quad & \mathbf{y}_m^{\nu} = N\mathbf{M}\mathbf{F}_N^{-1}\hat{\mathbf{r}}_x^{\nu}, \end{aligned} \tag{4.21}$$

for each ν. In order to exploit the additional knowledge that the vectors $\hat{\mathbf{r}}_x^{\nu}|_{\nu=\nu_1}^{\nu_{n_\nu}}$ have the same support (they are jointly sparse with regard to the time delay), we propose to use an extension of OMP called simultaneous orthogonal matching pursuit (SOMP) [69]. The CA estimation based on SOMP is given in Algorithm 2.

Algorithm 2: SOMP-based CA estimator (SOBER)

Input: $\mathbf{Y}_m, n_{\text{iter}}, \mathbf{A} = N\mathbf{M}\mathbf{F}_N^{-1}$
Output: $\hat{\mathbf{R}}_x$

$\hat{\mathbf{R}}_x = \mathbf{0}, S_0 = \emptyset$;
for $i = 1, \ldots, n_{iter}$ **do**
  $\mathbf{C} = (\mathbf{Y}_m - \mathbf{A}\hat{\mathbf{R}}_x)^{\mathrm{H}}\mathbf{A}$;
  $S_i = S_{i-1} \cup \underset{j\in\{1,\ldots,N\}}{\operatorname{argmax}} \left\{\|\mathbf{c}_j\|_1\right\}$;
  for $k = 1, \ldots, n_\nu$ **do**
    $\hat{\mathbf{r}}_x^{\nu_k} = \underset{\mathbf{z}\in\mathbb{C}^N}{\operatorname{argmin}} \{\|\mathbf{y}_m^{\nu_k} - \mathbf{A}\mathbf{z}\|_2, \operatorname{supp}(\mathbf{z}) \subset S_i\}$;

The number of iterations is denoted by n_{iter}, the $n_\nu \times N$ matrix $\mathbf{C}$ contains correlation values and $\mathbf{c}_j$ is its j-th column, $\mathbf{y}_m^{\nu_k}$ denotes the k-th column of $\mathbf{Y}_m$ and $\operatorname{supp}(\cdot)$ stands for the support of a vector, i. e., the indices of its non-zero entries. We refer to the columns of the matrix $\mathbf{A} = N\mathbf{M}\mathbf{F}_N^{-1}$ introduced in Algorithm 2 as atoms.

Since asymptotically, $\hat{\mathbf{R}}_x$ has only few rows with non-zero entries, up to a certain residuum the columns of $\mathbf{Y}_m$ should be representable by a weighted combination of only few of the atoms contained in $\mathbf{A}$. The goal of the algorithm is to find the indices

of the atoms contained in $\mathbf{Y}_m$, i. e., the support of the columns of $\hat{\mathbf{R}}_x$, and subsequently recover the identified non-zero rows of $\hat{\mathbf{R}}_x$ by solving least-squares problems. We start with an empty support S_0. Each iteration, one atom index is added to the support. The index is selected according to the sum of the absolute correlation values between the corresponding atoms and the delay products of different time delays (lines 3-4). Using the new support set S_i, a least-squares problem is solved for each column in $\hat{\mathbf{R}}_x$ (lines 5-6). In each iteration the atom index to be added to the index set is chosen according to the correlation between the residuum of $\mathbf{Y}_m$ and the atom set. Since every iteration adds one index to the support set, one usually chooses n_{iter} greater than or equal to the sparsity of the signal to be recovered. The difference between OMP (used in, e. g., [63]) and SOMP can be found in line 4, where SOMP jointly considers the amount of correlation between atoms and the delay products of *multiple* delays, while OMP would select the support of $\hat{\mathbf{r}}_x^{\nu_l}|_{l=1}^{n_\nu}$ for each l individually.

The support determined by the algorithm constitutes a set of cycle frequencies. To determine the observed band's occupancy status, we need to test for the presence of cyclostationarity at the support using the TDT. However, since only few of the coefficients of $\hat{\mathbf{R}}_x$ are recovered and all other coefficients are set to zero, it is not possible to estimate the covariance matrix $\hat{\mathbf{\Sigma}}_{xx^*}$ as part of the TDT as presented in Section 4.3. To tackle this problem, a modified TDT is presented in Section 4.7.

4.5 Dictionary Assisted CA Estimation

In Section 4.4 we have described a SOMP-based algorithm that estimates the cycle frequencies and the CA from fewer samples than required using the classic approach by taking into consideration the inherent sparsity of the CA. In this section we develop an algorithm that makes use of additional prior knowledge about the signal's structure in the form of structure dictionaries to further enhance the cycle frequency and CA estimation. Like SOBER, the new algorithm does not require the prior knowledge about the cycle frequencies contained in the signal.

One fact about the CA that could be exploited is that using a rectangular pulse shape, a linearly modulated signal's CA exhibits spikes not only at the signal's fundamental cycle frequency but also at the harmonics thereof. Another one is the symmetry of the CA around the DC component for certain types of signals. First steps in this direction showing promising results have been taken in [19]. The drawback of the solution proposed in [19] is that the convex optimization problem used to recover the CA becomes huge for practical parameter choices, which results in a prohibitively large computational complexity. To circumvent this we propose an OMP-based greedy algorithm that takes advantage of the additional prior knowledge while featuring a much smaller complexity than the optimization problem. In the following we introduce a structure dictionary accounting for the symmetry of the CA and describe the proposed dictionary assisted recovery algorithm. In the subsequent section we discuss a second structure dictionary

that can be used with the proposed algorithm, i.e., the dictionary containing the harmonic structure of the CA as well as its shape.

Let $\mathbf{D}_{\text{sym}}^{(\frac{N}{2})} \in \{0,1\}^{\frac{N}{2}\times\frac{N}{2}}$ denote the symmetry dictionary. Its columns represent possible cycle frequencies contained in the set $a \in \{1,\dots,\frac{N}{2}\}$. For simplicity, this set is chosen such that the frequencies contained in it lie at the center frequencies of the CA's DFT bins. An entry of the dictionary covers the elements 1 to $\frac{N}{2}$ of $\hat{\mathbf{r}}_x^{\nu}$ which is indexed from 0 to $N-1$. The symmetry dictionary is simply given by the identity matrix, i. e., $\mathbf{D}_{\text{sym}}^{(\frac{N}{2})} = \mathbf{I}_{\frac{N}{2}}$. To model the whole vector $\hat{\mathbf{r}}_x^{\nu}$, the dictionary is extended to include the DC component, which is set to zero, as well as the negative cycle frequencies. Note that the DC component is set to zero because its value is independent of the presence of cyclostationarity. The resulting *full* dictionary is exemplarily given by

$$\mathring{\mathbf{D}}_{\text{sym}}^{(3)} = \begin{pmatrix} 0 & 0 & 0 \\ 1 & 0 & 0 \\ 0 & 1 & 0 \\ 0 & 0 & 1 \\ 0 & 1 & 0 \\ 1 & 0 & 0 \end{pmatrix}. \tag{4.22}$$

The circle above the symbol indicates that it is the full version of the dictionary, i. e., the one spanning the whole frequency range. The *ones* in the matrix specify the locations of the non-zero coefficients in the CA fitting the format of (4.8).

Algorithm 3: Dictionary assisted CA estimator (DICE)

Input: $\mathbf{Y}_m, n_{\text{iter}}, \mathbf{A} = N\mathbf{M}\mathbf{F}_N^{-1}, \mathring{\mathbf{D}}_l^{(\frac{N}{2})}|_{l=1}^{n_\nu}$
Output: $\hat{\mathbf{R}}_x$

$\hat{\mathbf{R}}_x = \mathbf{0}, S_0 = \{0\}$;
for $i = 1,\dots,n_{iter}$ **do**
  for $l = 1,\dots,n_\nu$ **do**
    $\left[\mathring{\mathbf{C}}\right]_{l:} = \text{abs}\left((\mathbf{y}_m^{\nu_l} - \mathbf{A}\hat{\mathbf{r}}_x^{\nu_l})^{\text{H}}\mathbf{A}\right)\mathring{\mathbf{D}}_l^{(\frac{N}{2})}$;
  $S_i = S_{i-1} \cup \left\{ h \,\middle|\, [\mathring{\mathbf{D}}^{(\frac{N}{2})}]_{hj} \neq 0, j = \underset{j\in\{1,\dots,\frac{N}{2}\}}{\text{argmax}} \left\{\|\mathring{\mathbf{c}}_j\|_1\right\} \right\}$;
  for $k = 1,\dots,n_\nu$ **do**
    $\hat{\mathbf{r}}_x^{\nu_k} = \underset{\mathbf{z}\in\mathbb{C}^N}{\text{argmin}} \left\{\|\mathbf{y}_m^{\nu_k} - \mathbf{A}\mathbf{z}\|_2, \text{supp}(\mathbf{z}) \subset S_i\right\}$;

The DICE algorithm (Algorithm 3) follows the same idea as the SOBER algorithm (Algorithm 2) in that it iteratively determines the support of the sparse CA and subsequently recovers it by solving an overdetermined least-squares problem. However, in

contrast to SOBER, DICE facilitates the use of further prior knowledge in addition to the CA's sparsity in the recovery process.

Thus, in addition to the inputs received by SOBER, DICE needs a set of structure dictionaries $\mathring{\mathbf{D}}_l^{(\frac{N}{2})}|_{l=1}^{n_\nu}$; one dictionary for each delay value ν_l that is to be considered in the recovery process. In the case of the symmetry dictionary, all of these are identical, i. e., $\mathring{\mathbf{D}}_l^{(\frac{N}{2})}|_{l=1}^{n_\nu} = \mathring{\mathbf{D}}_{\text{sym}}^{(\frac{N}{2})}$. Since the structure dictionaries do not necessarily model the DC component of the CA, it is added to the support set in the initialization phase in DICE (line 1). Instead of working with the amount of correlation between the residuum and the atoms directly as in SOBER, the DICE algorithm computes combinations of these as dictated by the structure dictionaries in use (lines 3, 4). This way, the decision about the non-zero cycle frequencies (line 5) takes into account the structure of the CA. Additionally, instead of adding a single element to the support set per iteration, Algorithm 3 adds all indices to the support set that have a non-zero value in the selected dictionary word. The recovery step (cf. lines 6, 7) remains unchanged. Note that in Algorithm 3 the abs(·) operator stands for the element-wise absolute value of a matrix, while the selection operator $[\cdot]_{l:}$ denotes the l-th row of a matrix.

4.6 Asymptotic CA and Asymptotic Dictionary

The symmetry structure dictionary exploits one of the facts we know about the CA of certain types of signals. In order to explore an extreme in terms of prior knowledge we create a dictionary that contains the maximum possible amount of prior information about the CA, i. e., the one containing the asymptotic CA itself. This requires knowledge of the analytic expression for the discrete asymptotic CA vector, which we derive in the following.

To assess the performance of different CA estimation algorithms we employ common linearly modulated signals with symbol length T_s as described by the following equation [40, Eq. 73]

$$s(t) = \sum_{n=-\infty}^{\infty} c_n p\left(t - nT_s + \phi\right). \tag{4.23}$$

Here, $p\left(t\right)$ is a deterministic finite-energy pulse, ϕ represents a fixed pulse-timing phase parameter and c_n stands for the n-th symbol to be transmitted. We are now interested in an expression for the discrete asymptotic CA vector of the above signal type.

The fundamental cycle frequency of the built-in periodicity of the signal from (4.23) is $\frac{1}{T_s}$. Its continuous CA is given by [40, Eq. 81]

$$R_{s,T_s}^{\alpha}(\tau) = \begin{cases} 0 & \text{for } \alpha \neq \frac{k}{T_s} \\ \frac{1}{T_s} \sum\limits_{n=-\infty}^{\infty} R_c(nT_s) r_p^{\alpha}(\tau - nT_s) e^{j2\pi\alpha\phi} & \text{otherwise,} \end{cases} \tag{4.24}$$

where $k \in \mathbb{Z}$ and $r_p^\alpha(\tau)$ is defined as [40, Eq. 82]

$$r_p^\alpha(\tau) \triangleq \int_{-\infty}^{\infty} p\,(t+\tau/2)\,p^*\,(t-\tau/2)\,e^{-j2\pi\alpha t}\,\mathrm{d}t. \tag{4.25}$$

The symbol $\mathbb{Z}$ denotes the set of integers, i. e., $k \in \{\dots, \text{-}2, \text{-}1, 0, 1, 2, \dots\}$.

We consider the case where c_n is a purely stationary random sequence. Thus, its autocorrelation $R_c(nT_s) = R_c^0(nT_s)$ is non-zero only at $n = 0$ (cf. (4.1)), reducing (4.24) to

$$R_{s,T_s}^\alpha(\tau) = \begin{cases} 0 & \text{for } \alpha T_s \notin \mathbb{Z} \\ \frac{\sigma_c^2}{T_s} r_p^\alpha(\tau) e^{j2\pi\alpha\phi} & \text{otherwise,} \end{cases} \tag{4.26}$$

where σ_c^2 is the average power of c_n. In the following we assume a rectangular pulse shape of length T_s, i. e., $p\,(t) = \mathrm{rect}(\frac{t}{T_s})$, which leads to $p\left(t+\frac{\tau}{2}\right)p^*\left(t-\frac{\tau}{2}\right) = \mathrm{rect}\left(\frac{t}{T_s-|\tau|}\right)$. Thus, applying the Fourier transform to (4.25) yields

$$R_{s,T_s}^\alpha(\tau) = \begin{cases} 0 & \text{for } \alpha T_s \notin \mathbb{Z} \\ \sigma_c^2 \frac{T_s-|\tau|}{T_s} \operatorname{sinc}(\alpha(T_s-|\tau|)) e^{j2\pi\alpha\phi} & \text{otherwise,} \end{cases} \tag{4.27}$$

for $|\tau| \leq T_s$. We use the normalized version of the sinc function, i. e.,

$$\operatorname{sinc}(x) = \frac{\sin(\pi x)}{\pi x}. \tag{4.28}$$

Note that the use of the absolute value of the delay stems from the fact that for a real symmetric pulse shape $p\,(t)$, the expression $p\left(t+\frac{\tau}{2}\right)p^*\left(t-\frac{\tau}{2}\right)$ is symmetric with respect to τ.

Equation (4.27) represents the CA of the continuous-time signal described by (4.23). In the following we derive the CA of the sampled version of (4.23), i. e., the discrete asymptotic CA.

The relation between the CA of the continuous time-domain signal $s(t)$ and its sampled counterpart $\{s(nT_e)\}$ is given by [70, Ch. 11, Sec. C, Eq. 111]

$$R'^{\alpha}_{s,T_s}(\nu T_e) = \sum_{l=-\infty}^{\infty} R_{s,T_s}^{\alpha+\frac{l}{T_e}}(\nu T_e) e^{j\pi l\nu}. \tag{4.29}$$

The sum over l reflects the infinite aliasing caused by the sampling. In the next step, we insert (4.27) into (4.29). Also we express quantities in terms of the sampling period T_e, i. e., $T_s \to n_s T_e, \alpha \to \frac{a}{NT_e}, \phi \to d_\phi T_e$, with $n_s, a, N \in \mathbb{Z}$. This leads to

$$R'^{a}_{s,n_s}(\nu) = \begin{cases} 0 & \text{for } a \neq \frac{kN}{n_s} \\ \sigma_c^2 \frac{n_s-|\nu|}{n_s} e^{j2\pi\frac{a}{N}d_\phi} \sum\limits_{l=-\infty}^{\infty} e^{j\pi l\nu} & \\ \qquad \cdot e^{j2\pi l d_\phi} \operatorname{sinc}((\frac{a}{N}+l)(n_s-|\nu|)) & \text{otherwise,} \end{cases} \tag{4.30}$$

for $|\nu| \leq n_s$, where n_s is the oversampling factor.

In this step we used the fact that for our assumptions all aliases of the fundamental cycle frequency and its harmonics lie on top of the actual fundamental cycle frequency and its harmonics, i. e.,

$$(\alpha + \frac{l}{T_e})T_s \in \mathbb{Z} \text{ iff } \alpha T_s \in \mathbb{Z}. \tag{4.31}$$

Inserting the discrete quantities given above, we get

$$(\frac{a}{N} + l)n_s \in \mathbb{Z} \text{ iff } \frac{a}{N}n_s \in \mathbb{Z}. \tag{4.32}$$

Since $n_s \in \mathbb{Z}$ and $l \in \mathbb{Z}$, this always holds.

To rule out any spectral leakage, we choose N as an integer multiple of n_s, since then $a = k\frac{N}{n_s}$ is also an integer and thus the fundamental discrete cycle frequency and its harmonics hit center frequencies of frequency bins.

For $a = k\frac{N}{n_s}$ expression (4.30) can be shown to be

$$R'^{a}_{s,n_s}(\nu)\big|_{a=k\frac{N}{n_s}} = \sigma_c^2 \frac{\sin(\pi\frac{a}{N}(n_s - |\nu|))}{\pi n_s} e^{j2\pi\frac{a}{N}d_\phi} \sum_{l=-\infty}^{\infty} \frac{(-1)^l}{\frac{a}{N} + l}. \tag{4.33}$$

To obtain (4.33) we used the definition of the sinc and exploited the fact that

$$e^{j\pi k} = (-1)^k \text{ for } k \in \mathbb{Z} \tag{4.34}$$

as well as the fact that

$$\sin(x + k\pi) = (-1)^k \sin(x) \text{ for } k \in \mathbb{Z}. \tag{4.35}$$

The pulse timing phase parameter d_ϕ was set to $\frac{n_s+1}{2}$. This has the following reason. In order to simplify the numerical evaluation, we want to choose ϕ such that the beginning of the observed receiver signal is aligned with the rectangular pulse shapes, i. e., we would set $\phi = \frac{T_s}{2}$. However, doing so would lead to the need to sample at the discontinuities caused by the instant change in amplitudes at the transition between symbols. To avoid this we choose $\phi = \frac{T_s}{2} + \epsilon$, where $\epsilon \in (0, T_e)$. Note, that (4.33) is the same for any $\epsilon \in (0, T_e)$. In order to ease the derivation we can thus choose $\epsilon = \frac{T_e}{2}$, i. e., $d_\phi = \frac{n_s+1}{2}$.

The infinite series in (4.33) can be expressed as

$$\begin{aligned}\sum_{l=-\infty}^{\infty}\frac{(-1)^l}{\frac{a}{N}+l} &= \frac{N}{a}+\sum_{l=1}^{\infty}\frac{(-1)^l}{\frac{a}{N}+l}+\frac{(-1)^l}{\frac{a}{N}-l}\\ &= \frac{N}{a}+\frac{1}{2}\sum_{l=1}^{\infty}-\frac{1}{l+\frac{a}{2N}-\frac{1}{2}}+\frac{1}{l-\frac{a}{2N}-\frac{1}{2}}-\frac{1}{l-\frac{a}{2N}}+\frac{1}{l+\frac{a}{2N}}\\ &= \frac{N}{a}+\frac{1}{2}\sum_{l=1}^{\infty}-\frac{l+\frac{a}{2N}-\frac{1}{2}-\frac{a}{2N}+\frac{1}{2}}{l(l+\frac{a}{2N}-\frac{1}{2})}+\frac{l-\frac{a}{2N}-\frac{1}{2}+\frac{a}{2N}+\frac{1}{2}}{l(l-\frac{a}{2N}-\frac{1}{2})}\\ &\quad -\frac{l-\frac{a}{2N}+\frac{a}{2N}}{l(l-\frac{a}{2N})}+\frac{l+\frac{a}{2N}-\frac{a}{2N}}{l(l+\frac{a}{2N})}\\ &= \frac{N}{a}+\frac{1}{2}\sum_{l=1}^{\infty}\frac{\frac{a}{2N}-\frac{1}{2}}{l(l+\frac{a}{2N}-\frac{1}{2})}-\frac{-\frac{a}{2N}-\frac{1}{2}}{l(l-\frac{a}{2N}-\frac{1}{2})}\\ &\quad +\frac{-\frac{a}{2N}}{l(l-\frac{a}{2N})}-\frac{\frac{a}{2N}}{l(l+\frac{a}{2N})}.\end{aligned} \tag{4.36}$$

The digamma function, denoted by $\psi(z)$, possesses a series expansion given by [71, Eq. 6.3.16]

$$\psi(1+z) = \text{-}\gamma+\sum_{n=1}^{\infty}\frac{z}{n(n+z)} \text{ for } z\notin\{\text{-}1,\text{-}2,\text{-}3,\dots\}, \tag{4.37}$$

where γ denotes the Euler-Mascheroni constant. We can thus simplify (4.36) by expressing it in terms of the digamma function as

$$\begin{aligned}\sum_{l=-\infty}^{\infty}\frac{(-1)^l}{\frac{a}{N}+l} = \frac{N}{a}+\frac{1}{2}\Bigg(&\psi\left(\frac{1}{2}+\frac{a}{2N}\right)-\psi\left(\frac{1}{2}-\frac{a}{2N}\right)\\ &+\psi\left(1-\frac{a}{2N}\right)-\psi\left(1+\frac{a}{2N}\right)\Bigg).\end{aligned} \tag{4.38}$$

The reflection formula of the digamma function is given by [71, Eq. 6.3.7]

$$\psi(1-z)-\psi(z) = \pi\cot(\pi z). \tag{4.39}$$

Applying it we can write

$$\begin{aligned}\psi\left(\frac{1}{2}+\frac{a}{2N}\right)-\psi\left(\frac{1}{2}-\frac{a}{2N}\right) &= \psi\left(1-\left(\frac{1}{2}-\frac{a}{2N}\right)\right)-\psi\left(\frac{1}{2}-\frac{a}{2N}\right)\\ &= \pi\cot\left(\pi\left(\frac{1}{2}-\frac{a}{2N}\right)\right)\end{aligned} \tag{4.40}$$

The recurrence formula of the digamma function is given by [71, Eq. 6.3.5]

$$\psi(1+z) = \psi(z)+\frac{1}{z}. \tag{4.41}$$

Using the recurrence as well as the reflection formula we obtain

$$\begin{aligned}\psi\left(1-\frac{a}{2N}\right)-\psi\left(1+\frac{a}{2N}\right) &= \psi\left(1-\frac{a}{2N}\right)-\psi\left(\frac{a}{2N}\right)-2\frac{N}{a}\\ &= \pi\cot(\pi\frac{a}{2N})-2\frac{N}{a}.\end{aligned} \tag{4.42}$$

Inserting (4.40) and (4.42) into (4.38) results in

$$\begin{aligned}\sum_{l=-\infty}^{\infty}\frac{(-1)^l}{\frac{a}{N}+l} &= \frac{1}{2}\pi\left(\cot\left(\pi\left(\frac{1}{2}-\frac{a}{2N}\right)\right)+\cot\left(\pi\frac{a}{2N}\right)\right)\\ &= \frac{1}{2}\pi\left(\tan\left(\pi\frac{a}{2N}\right)+\cot\left(\pi\frac{a}{2N}\right)\right)\\ &= \frac{\pi}{\sin\left(\pi\frac{a}{N}\right)}.\end{aligned} \tag{4.43}$$

Finally, substituting (4.43) into (4.33) gives us the expression

$$R'^{a}_{s,n_s}(\nu)\big|_{a=k\frac{N}{n_s}} = \frac{\sigma_c^2}{n_s}\frac{\sin(\pi\frac{a}{N}(n_s-|\nu|))}{\sin\left(\pi\frac{a}{N}\right)}e^{j2\pi\frac{a}{N}d_\phi}, \tag{4.44}$$

which constitutes the CA of the sampled signal at its fundamental cycle frequency and the harmonics thereof.

The coefficients of the closed-form expression (4.44) together with the alternative case $R'^{a}_{s,n_s}(\nu)\big|_{a\neq k\frac{N}{n_s}} = 0$ at different discrete cycle frequencies a are arranged in a vector $\mathbf{r}^{\nu}_{s,n_s}[a]$ matching the format of the DFT matrix, such that

$$\mathbf{r}^{\nu}_{s,n_s}[a] = \begin{cases} R'^{a}_{s,n_s}(\nu) & \text{for } a\in\{0,\ldots,\frac{N}{2}\},\\ R'^{(a-N)}_{s,n_s}(\nu) & \text{for } a\in\{\frac{N}{2}+1,\ldots,N-1\}.\end{cases} \tag{4.45}$$

Note, that adding purely stationary noise to the signal $s(t)$ does not change its asymptotic CA (with the exception of $(a,\nu)=(0,0)$, at which point the CA's value is the average power of signal and noise, cf. (4.1)) since the noise exhibits no inherent periodic behavior. Due to this fact, (4.45) can also be used as a reference for the CA of signals contaminated with additive white Gaussian noise (AWGN) with the exception mentioned.

Given (4.45) we can now construct the asymptotic dictionary:

$$\mathring{\mathbf{D}}^{(\frac{N}{2})}_{\text{asy},l} = \left[\frac{\text{abs}\left(\mathbf{r}^{\nu_l}_{s,n_s=\frac{N}{1}}\right)}{\left\|\mathbf{r}^{\nu_l}_{s,n_s=\frac{N}{1}}\right\|_1},\ldots,\frac{\text{abs}\left(\mathbf{r}^{\nu_l}_{s,n_s=\frac{N}{N/2}}\right)}{\left\|\mathbf{r}^{\nu_l}_{s,n_s=\frac{N}{N/2}}\right\|_1}\right]. \tag{4.46}$$

Note, that in contrast to the single symmetry dictionary, there is a whole set of asymptotic dictionaries, one for each delay value of interest. The columns of the dictionaries

correspond to actual symbol lengths, i. e., actual cycle frequencies. Thus, each column contains the absolute value of the normalized asymptotic CA of a cycle frequency candidate where the discrete symbol lengths $n_s \in \left\{\frac{N}{1}, \ldots, \frac{N}{N/2}\right\}$ correspond to the discrete cycle frequencies $a \in \{1, \ldots, N/2\}$. It is worth noting that in addition to its role as the basis of the second structure dictionary for Algorithm 3, the expression (4.45) serves as a reference for the direct comparison of different CA estimation methods in Section 4.8.

4.7 Cyclostationarity Detection from Sparse Cyclic Spectra

Both, the SOMP-based (Algorithm 2) and the dictionary assisted CA estimation (Algorithm 3), are able to recover the CA without knowing which cycle frequencies are contained in the signal beforehand. However, although this makes for a good CA estimation, it is not directly compatible with the traditional TDT described in Section 4.3, since it only recovers the CA coefficients at the cycle frequencies, not the ones in between.

The TDT is a CFAR detector, i. e., the PDF of its test statistic under $\mathcal{H}_0$ is asymptotically independent of any signal parameters like, e. g., the noise power. To achieve this, the TDT first estimates the CA noise covariance and then rescales the original CA by this estimate so that the scaled CA follows a *standard* Gaussian distribution. This is where the problem occurs. Although, we are ultimately only interested in the CA coefficients that are located at the signal's cycle frequencies, for the estimation of the noise covariance we need the coefficients lying between the cycle frequencies, which only carry estimation noise. SOBER and DICE do not recover these. Thus, we propose an extension to the TDT, the sparse TDT, to bridge this gap, in the following.

To obtain optimal CA recovery performance one would choose the sensing matrix $\mathbf{A}$ with minimum structure, i. e., the selection of the m entries of the delay product would be completely random. However, to tackle the aforementioned problem we choose a combination of consecutive and random delay product elements. The consecutive part comprises the first $\lceil \beta m \rceil$ rows of $\mathbf{Y}_m$, where $\beta \in [0.01, 0.5]$ and $\lceil \cdot \rceil$ denotes the ceiling operation. The remainder of the rows of $\mathbf{Y}_m$ is a random selection of the remaining rows of $\mathbf{Y}_N$. The first step of the sparse TDT is to determine the classical CA estimation of the consecutive block of delay product elements. In the next step the cycle frequency of interest a_0 is determined using either Algorithm 2 or Algorithm 3. Next, the covariance matrix for the cycle frequency a_0 corresponding to the N-size CA $\left(\hat{\mathbf{\Sigma}}^{(N)}_{xx^*}(a_0)\right)$ needs to be determined, where the superscript (N) indicates the corresponding CA size. It is obtained as

$$\hat{\mathbf{\Sigma}}^{(N)}_{xx^*}(a_0) = \frac{\hat{\mathbf{\Sigma}}^{(\lceil \beta m \rceil)}_{xx^*}(\lceil \beta \frac{m}{N} a_0 \rceil)}{\sqrt{\beta \frac{m}{N}}}, \tag{4.47}$$

where $\hat{\mathbf{\Sigma}}^{(\lceil \beta m \rceil)}_{xx^*}$ is the covariance matrix corresponding to the $\lceil \beta m \rceil$-size CA estimated from the consecutive samples in the first step. The test statistic is subsequently evaluated

Table 4.1: Parameters

Parameter	Symbol	Value(s)
Size of the CA vector - CS methods	N	4000
# of known delay-product elements	m	1000
Size of the CA vector - classic method	m	1000
Discrete time delays	ν	$\{1, 2, 3, 4\}$
Modulation type		BPSK
Discrete symbol length	n_s	8
Signal to noise ratio	SNR	$\{-4, \ldots, 4\}$ dB
# of Monte Carlo instances		10000
Consecutive sample ratio	β	$\{0.01, \ldots, 0.5\}$
Covariance estimation window type	W	Kaiser
Kaiser window parameter	α_{Kaiser}	10
Kaiser window length	L	201

as (cf. (4.17))

$$\mathcal{T}_{xx^*}^{\text{sparse}} = N\hat{\mathbf{r}}_{xx^*}(a_0) \left(\frac{\hat{\mathbf{\Sigma}}_{xx^*}^{(\lceil \beta m \rceil)}(\lceil \beta \frac{m}{N} a_0 \rceil)}{\sqrt{\beta \frac{m}{N}}} \right)^{-1} \hat{\mathbf{r}}_{xx^*}^{\mathrm{T}}(a_0). \tag{4.48}$$

The consecutive sample ratio β is a trade-off parameter. The optimal sparse recovery performance is to be expected for the case that $\mathbf{A} = N\mathbf{M}\mathbf{F}_N^{-1}$ has the smallest possible amount of structure, which here corresponds to the case where the set of known delay product elements is chosen completely at random, i. e., for $\beta = 0$. Contrarily, the best estimation quality for the CA covariance matrix $\hat{\mathbf{\Sigma}}_{xx^*}$ is achieved when all known delay product elements are consecutive, i. e., for $\beta = 1$.

4.8 Numerical Evaluation

In this section we compare the performance of the methods presented in the preceding sections. The parameters used throughout this section are given in Table 4.1.

We begin by investigating the influence of the consecutive sample ratio β on the spectrum sensing performance. Figure 4.1 shows how the detection rate changes with β for an SNR of 0 dB and different false alarm rates. For all methods but the OMP, $\beta = 0.15$ is a good choice according to our numerical results. For the OMP the detection rate increases monotonically with β. However, as we can see below, even for the OMP, a high value for β is no good choice regarding other performance categories. Figure 4.2 and Figure 4.3 reinforce the choice of β. The choice of β seems to be independent of the SNR.

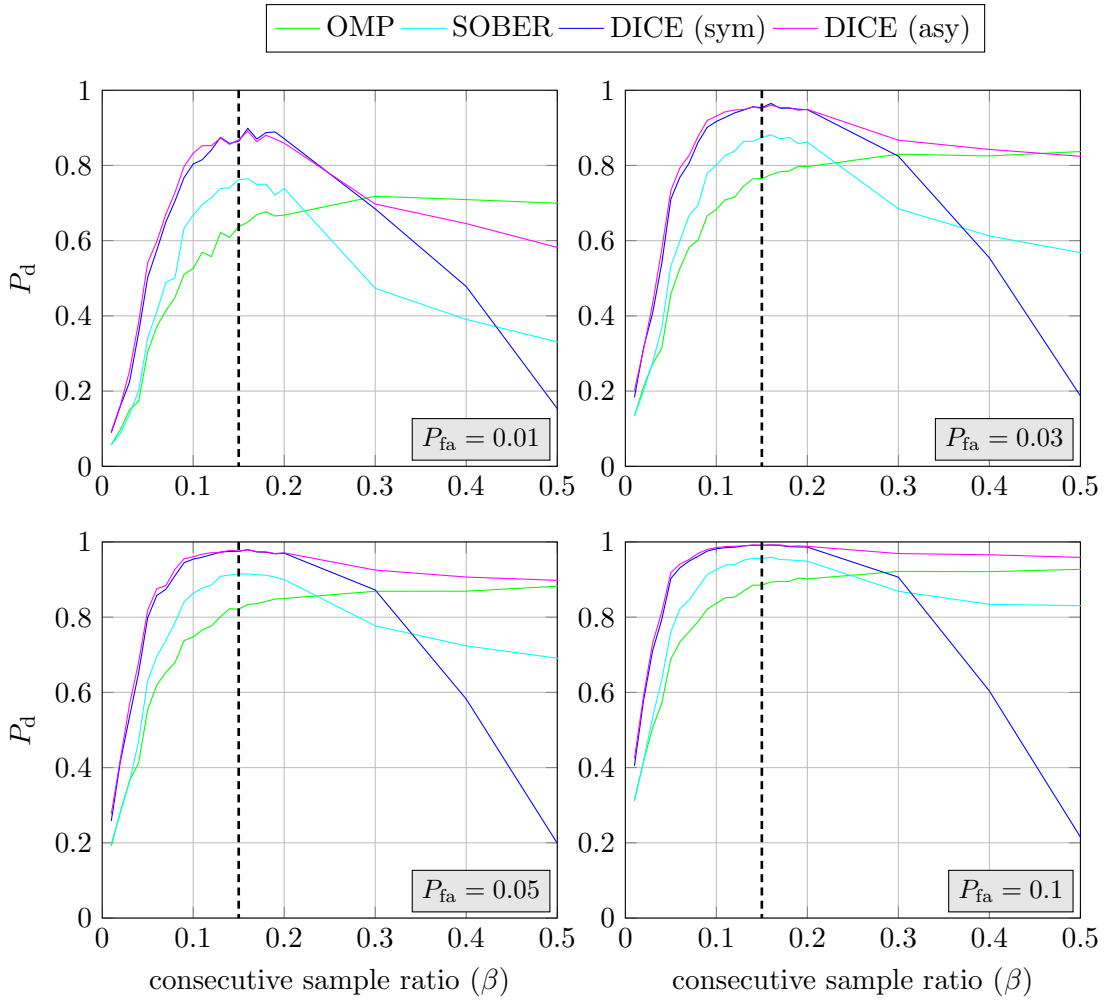

Figure 4.1: Detection rate over consecutive sample ratio for different false alarm rates at 0 dB SNR.

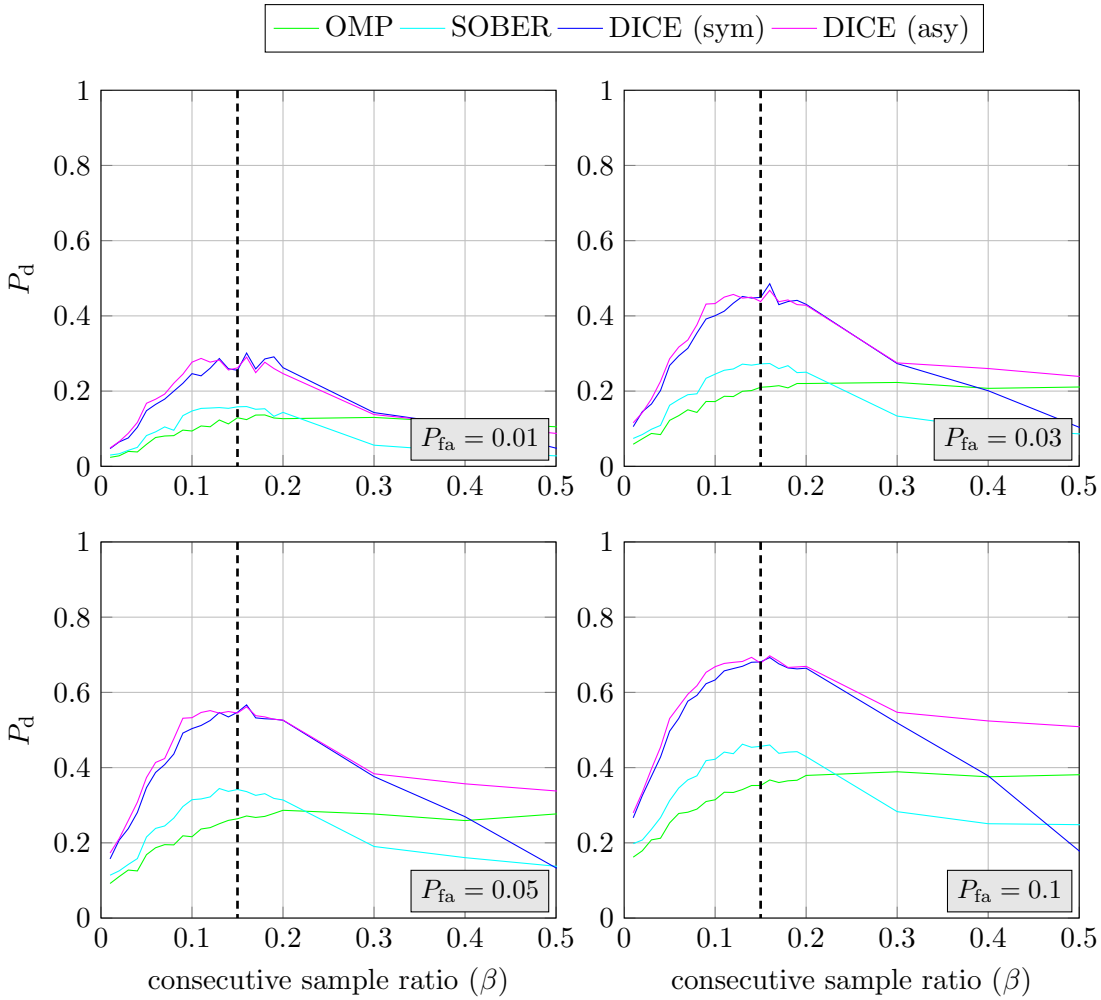

Figure 4.2: Detection rate over consecutive sample ratio for different false alarm rates at −3 dB SNR.

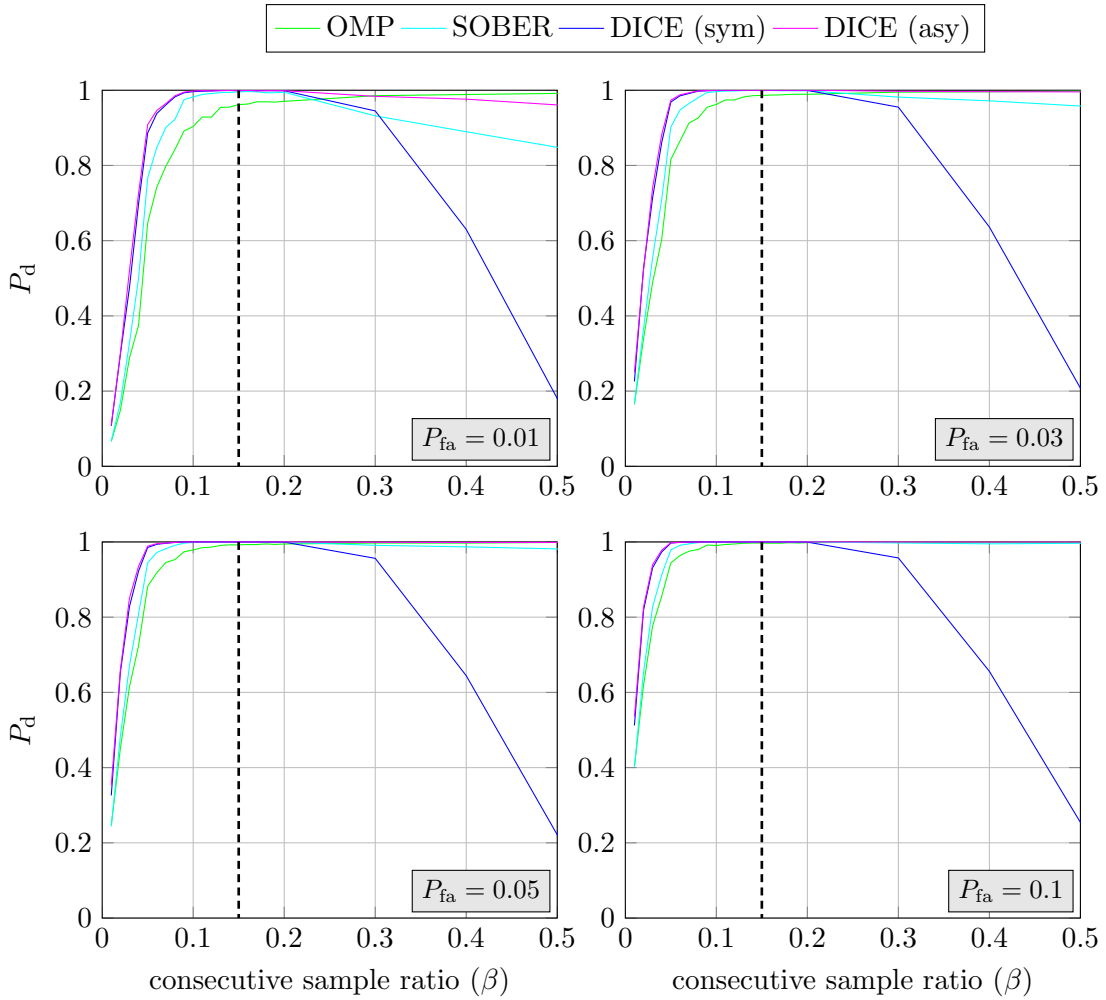

Figure 4.3: Detection rate over consecutive sample ratio for different false alarm rates at 3 dB SNR.

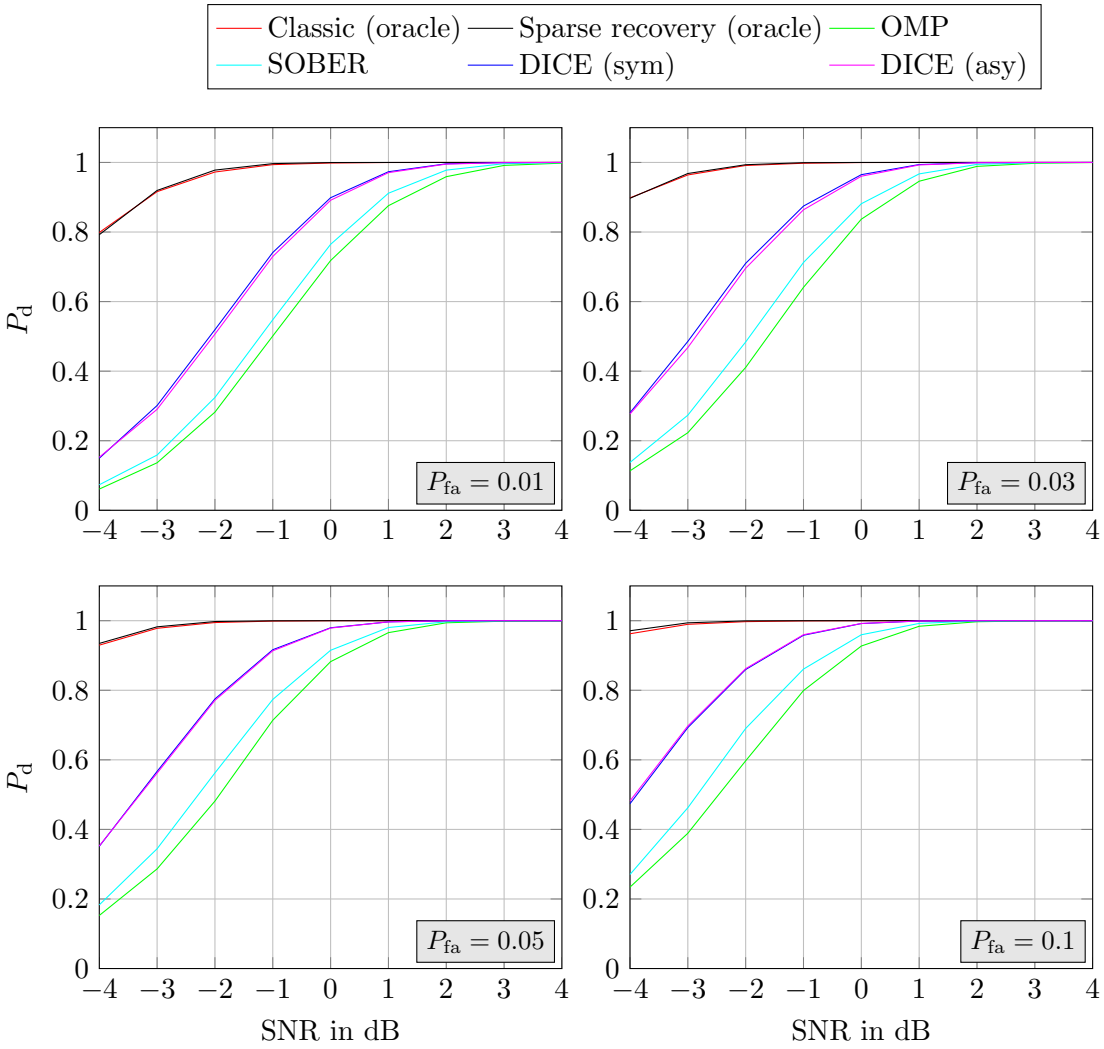

Figure 4.4: Maximum detection rate (optimal individual consecutive sample ratio selection) over SNR for different false alarm rates.

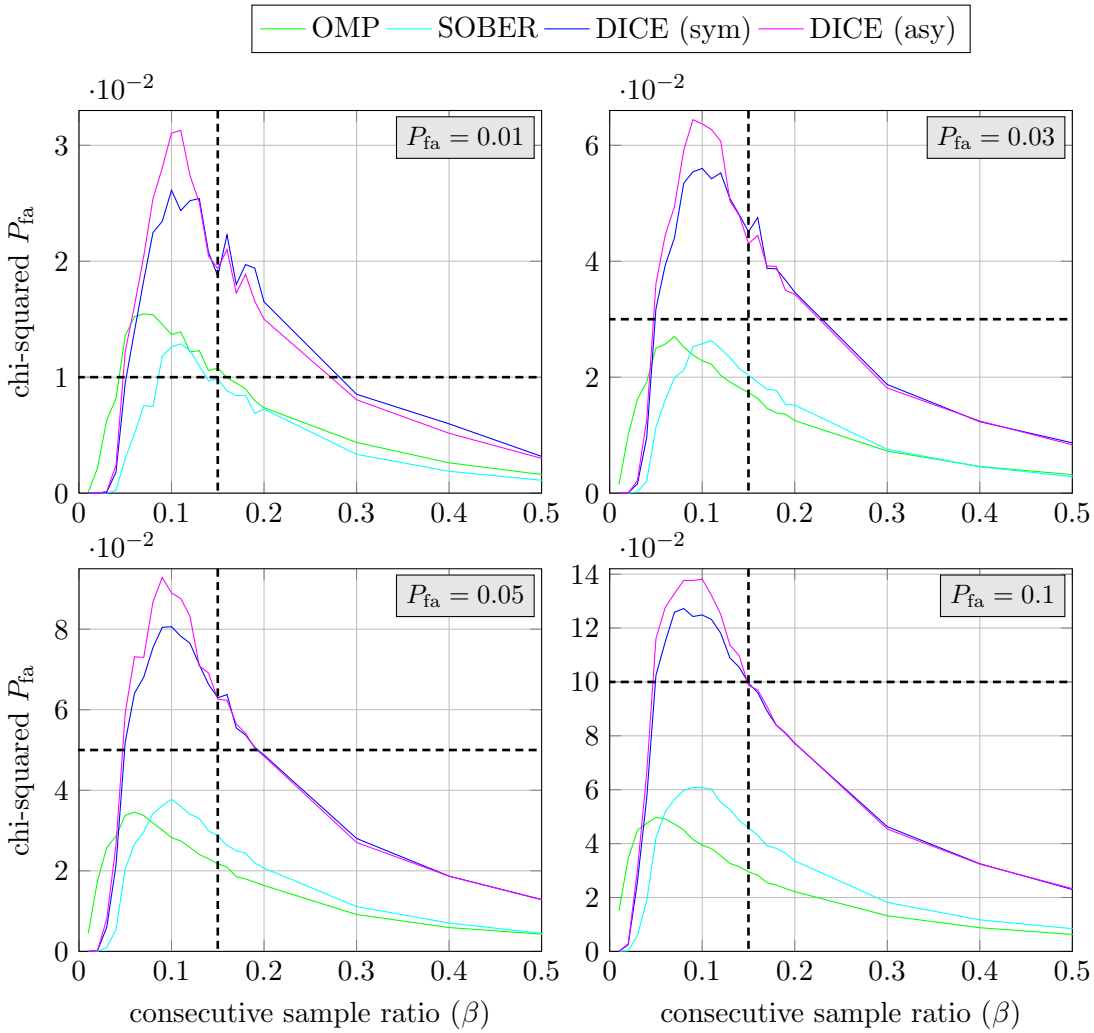

Figure 4.5: False alarm rate that has to be selected according to the chi-squared distribution to obtain different actual false alarm rates over the consecutive sample ratio.

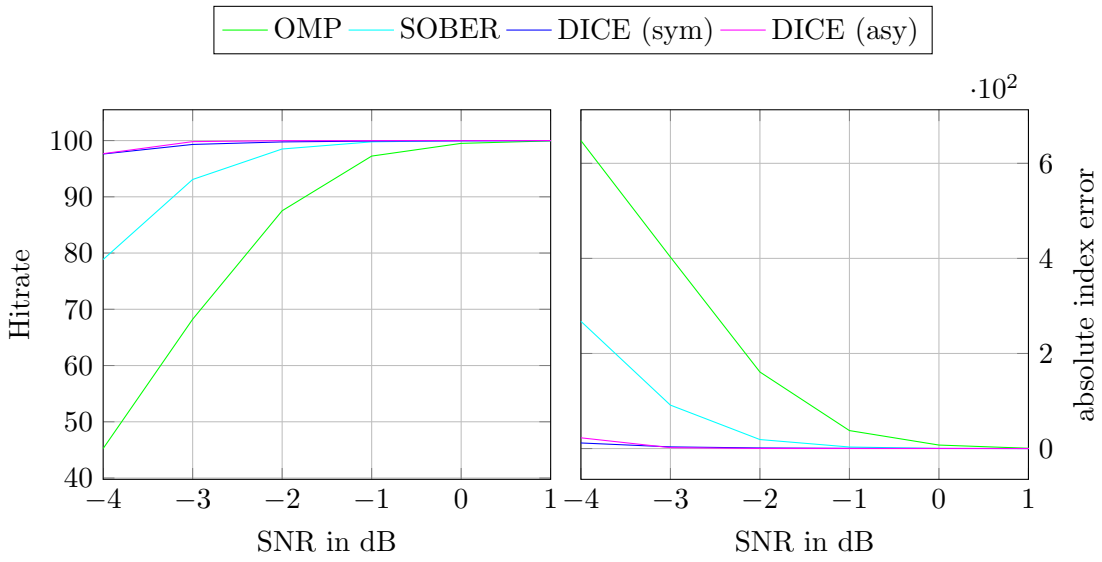

Figure 4.6: Left: Hitrate over SNR (in percent), right: absolute index error over SNR. Both at consecutive sample ratio 0.15.

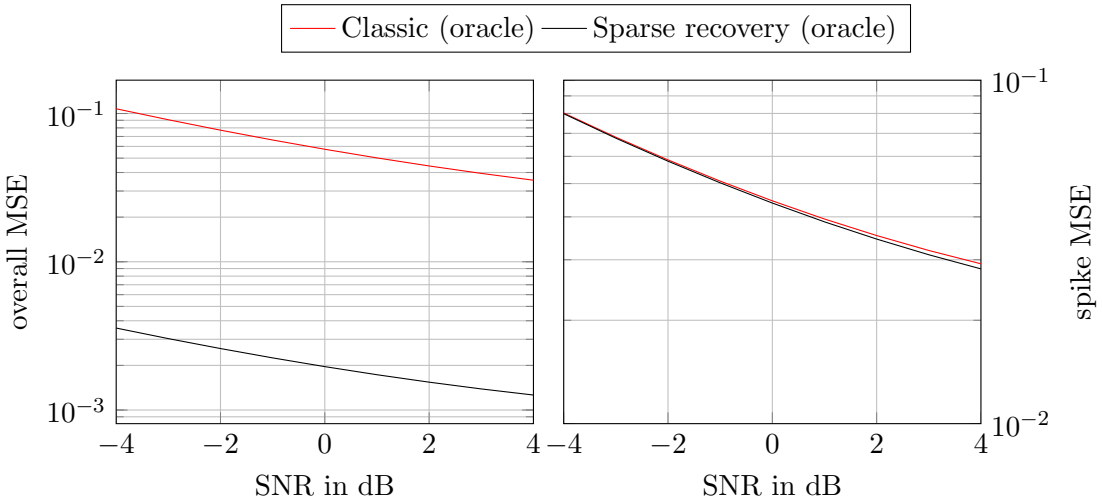

Figure 4.7: MSE between the CAF estimation and the actual (analytic) value. Left: over the whole support, right: at the cycle frequencies. Both at consecutive sample ratio 0.15.

In Figure 4.4 the best achievable detection rate, i. e., the detection rate for the individual best choice of β, of the different detectors is plotted over the receiver SNR for different false alarm rates. The term *oracle* expresses that a method has prior knowledge about the exact cycle frequencies contained in the signal. The classic method depends on this knowledge while for the sparse recovery, it reduces the CA recovery to solving the overdetermined least squares problem for the given support (cf. lines 5 and 6 in Algorithm 2 or lines 6 and 7 in Algorithm 3). As expected, the oracle methods outperform the methods which have to determine the CA support themselves by a large margin. Regarding the case of missing support knowledge, the DICE algorithm clearly outperforms the SOBER algorithm as well as OMP. It is to be noted that both, Figure 4.1 as well as Figure 4.4 do not show a significant performance advantage of exploiting the full knowledge of the asymptotic CA (DICE (asy)) over just exploiting its symmetry property (DICE (sym)) for a sensible choice of β.

The lines in Figure 4.5 show which false alarm rate according to the ideal chi-squared distribution has to be set in order to achieve 1, 3, 5, and 10 percent false alarm rate in the actual system. The dashed lines cross at the desired false alarm rate with $\beta = 0.15$. While the two DICE methods roughly keep within a one percent offset, OMP and SOBER show a decreasing degree of equivalence for an increasing false alarm rate. This indicates that using the chi-squared distribution for setting the decision threshold of the DICE algorithm is viable, which is an important observation. It means that in contrast to many other spectrum sensing algorithms, DICE approximately possesses a desirable feature called constant false alarm rate, i. e., its test statistic is independent of system parameters like the receiver noise power.

Figure 4.6 shows how well the support of the CA is recovered by the different methods. Since different types of communication signals feature different cycle frequencies, this information can be used for system identification. The hitrate is the chance of exactly recovering the correct support while the absolute index error is the mean recovery error in terms of CA bins. Obviously, the DICE methods have superior support recovery capabilities.

The final performance category we evaluate is the CA estimation quality achievable by sparse recovery methods measured by the mean squared error (MSE). In the left graph of Figure 4.7 the MSE over the whole CA is plotted while the right graph shows the MSE at the spikes of the CA, i. e., the MSE at the actual cycle frequencies. To determine the error, we use the analytic expression for the asymptotic CA vector as derived in Section 4.6, i. e., the MSE is defined as

$$\frac{\| \hat{\mathbf{R}}_x - \left[\mathbf{r}_{s,n_s}^{\nu_1}, \ldots, \mathbf{r}_{s,n_s}^{\nu_{n_\nu}} \right] \|_{\mathrm{F}}^2}{N n_\nu}, \tag{4.49}$$

where $\| \cdot \|_{\mathrm{F}}$ is the Frobenius norm. The sparse recovery method has a much lower *overall* MSE. This is caused by the fact that it sets all CA coefficients but the detected support to zero while the classical method results in a CA that features estimation noise

between the spikes. Regarding the *spike* MSE, both methods seem to perform roughly equivalently.

4.9 Conclusion

Blind operation and constant false alarm rate (CFAR) are desirable characteristics of spectrum sensing algorithms. Unfortunately, cyclostationarity-based approaches typically only feature either one or the other. We showed that this can be changed by using sparse recovery methods in the CA estimation. Subsequently, we developed a way to use further prior knowledge in addition to sparsity for superior CA estimation. We derived a closed-form expression of the CA of *sampled* linearly modulated signals with rectangular pulse shape to be used both as prior information for the CA estimation and as a reference for comparison. Finally, we extended a well known statistical test for cyclostationarity to accommodate sparse input. The results allow us to conclude that the proposed DICE algorithm in combination with the symmetric structure dictionary constitutes a viable alternative to the classical TDT for the case of missing prior information about the cycle frequencies contained in the signal.

5 Eigenvalue-Based Detection

Under the assumption that a sensor's received noise samples are i.i.d. with respect to time and that the noise experienced at different receivers is statistically independent of each other, the corresponding statistical covariance matrix contains only zero entries outside of its diagonal, while all diagonal entries contain the noise power. This, in turn, leads to the case where all eigenvalues of the covariance matrix have the same value. This property is exploited in the category of spectrum sensing algorithms called eigenvalue-based detection.

The idea is that while all eigenvalues have the same value when only i.i.d. noise is sensed, the eigenvalues are different if a PU signal is present in addition to the noise. This is true for both cases, the case where correlation between samples from different points in time at a single receiver are considered and the case where synchronized measurements from different receivers are under investigation.

Based on this premise, a rich literature has evolved, originating in the maximum-minimum-eigenvalue (MME) detector [16]. While the MME detector is based on the ratio between the largest and the smallest eigenvalue of the covariance matrix, i. e., its (standard) condition number, all kinds of different functions of the matrix's eigenvalues have been analyzed.

In this chapter we investigate how realistic the i.i.d. assumption of the receiver noise is and how important it is for the proper functioning of the MME detector. Furthermore, we propose two new eigenvalue-based test statistics for spectrum sensing and compare them to the most popular eigenvalue-based detectors.

Parts of the present chapter have been published in [20]. Other parts of the chapter are contained in [24], which is currently under review.

5.1 Model Uncertainties and SNR-Walls

Various spectrum sensing approaches have been shown to suffer from a so-called SNR-wall, an SNR value below which a detector cannot perform robustly no matter how many observations are used. Up to now, the eigenvalue-based MME detector has been a notable exception. For instance, the model uncertainty of imperfect knowledge of the receiver noise power, which is known to be responsible for the energy detector's fundamental limits, does not adversely affect the MME detector's performance. While

AWGN is a standard assumption in wireless communications, it is not a reasonable one for the MME detector. In fact, in this section we prove that uncertainty in the amount of noise coloring does lead to an SNR-wall for the MME detector. We derive a lower bound on this SNR-wall and evaluate it for example scenarios. The findings are supported by numerical simulations.

5.1.1 Motivation and Prior Work

The requirements spectrum sensing algorithms have to meet are quite demanding, e. g., the IEEE 802.22 standard for cognitive wireless regional area networks [72] states that an SU receiver should be able to reliably detect a PU signal at an SNR of -22 dB. There are good reasons for these demanding requirements, like, e. g., the hidden terminal problem [61, Ch. 14.3.3].

Under the ergodicity assumption, spectrum sensing algorithms are typically able to meet the above requirement, i. e., if enough samples are available, the PDFs of the test statistics are well separable. However, due to *model uncertainties* caused by, e. g., colored or non-stationary background noise, non-ideal filters and imperfectly estimated parameters, detection algorithms can exhibit so-called SNR-walls, i. e., SNR values, below which the detectors cannot robustly [73] decide between $\mathcal{H}_0$ and $\mathcal{H}_1$. The existence of SNR-walls has been established for the energy detector, the matched filter detector and the cyclostationarity detector [29, 30, 31]. A spectrum sensing algorithm that, to the best of our knowledge, has not been linked to the SNR-wall problem is the popular eigenvalue-based MME detector.

In this section, we identify noise coloring as a model uncertainty adversely affecting the MME detector. Then we show that uncertainty in the amount of noise coloring leads to an SNR-wall for the MME detector by using noise coloring to derive a lower bound on the SNR-wall of the MME detector. Finally, we support the analytical results with numerical simulations.

5.1.2 Signal Model and MME Test Statistic

Consider the discrete time complex baseband signal $x(n)$ observed at a secondary system receiver, where n denotes the discrete time index. As mentioned in Section 3.1, the task of a spectrum sensing algorithm is to decide between the following two hypotheses

$$\begin{aligned} \mathcal{H}_0 &: x(n) = \eta(n) \\ \mathcal{H}_1 &: x(n) = s(n) + \eta(n), \end{aligned} \tag{5.1}$$

where $s(n)$ represents a PU signal, while $\eta(n)$ stands for additive noise. For the sake of simplicity, no channel fading effects are taken into account in this section.

Throughout this section, the PU is assumed to transmit a linearly modulated signal with symbol length T_{symbol} exhibiting a rectangular pulse shape. The signal is oversampled at the receiver with an integer oversampling rate given by $M = \frac{T_{\text{symbol}}}{T_{\text{sample}}}$, where T_{sample} denotes the sampling period. The decision whether the band under observation is free ($\mathcal{H}_0$) or occupied ($\mathcal{H}_1$) is based on a block of N samples. In the decision process, samples from p different receivers are considered. The samples available at the fusion center at time instant n are given by

$$\begin{aligned}\mathbf{x}(n) = [&x_1(n), x_1(n-1), \ldots, x_1(n-Q),\\ &x_2(n), \ldots, x_p(n), \ldots, x_p(n-Q)]^{\mathrm{T}},\end{aligned} \tag{5.2}$$

where the subscript indicates, which receiver the samples are from. Each receiver contributes a consecutive set of $Q+1$ samples, where the quantity $Q+1$ is the so called smoothing factor [45]. The inclusion of samples from different receivers as well as samples from different points in time allows the MME detector to exploit correlation from both domains in the detection process. For simplicity, all receivers are assumed to experience the same SNR. The vectors $\mathbf{s}(n)$ and $\boldsymbol{\eta}(n)$ are defined analogous to $\mathbf{x}(n)$, leading to the concise representation

$$\mathbf{x}(n) = \mathbf{s}(n) + \boldsymbol{\eta}(n). \tag{5.3}$$

We consider a scenario with a single PU transmitter and multiple SU receivers. The receivers are assumed to be perfectly synchronized, i. e., $s_i(n)|_{i=1}^{p} = s(n)$. Signal and noise are generated by mutually independent stationary random processes. The PU signal $s(n)$ is zero-mean, has variance σ_s^2 and its symbols are independent, i. e., $s(n)$ and $s(n+M)$ are independent and identically distributed (i.i.d.). The receiver noise $\eta_i(n)$ is zero-mean and has variance σ_η^2 for all i. The noise vector $\boldsymbol{\eta}(n)$ is distributed according to a circularly-symmetric complex Gaussian distribution, i. e., $\boldsymbol{\eta}(n) \sim \mathcal{CN}_{p(Q+1)}(\mathbf{0}, \mathbf{R}_{\boldsymbol{\eta}})$.

Considering the fact that both the signal and the noise are zero-mean, the statistical covariance matrices can be obtained as

$$\begin{aligned}\mathbf{R}_{\mathbf{s}} &= \mathbb{E}\left[\mathbf{s}(n)\mathbf{s}(n)^{\mathrm{H}}\right]\\ \mathbf{R}_{\boldsymbol{\eta}} &= \mathbb{E}\left[\boldsymbol{\eta}(n)\boldsymbol{\eta}(n)^{\mathrm{H}}\right]\\ \mathbf{R}_{\mathbf{x}} &= \mathbb{E}\left[\mathbf{x}(n)\mathbf{x}(n)^{\mathrm{H}}\right]\\ &= \mathbf{R}_{\mathbf{s}} + \mathbf{R}_{\boldsymbol{\eta}},\end{aligned} \tag{5.4}$$

where $(\cdot)^{\mathrm{H}}$ denotes the complex conjugate transpose. We assume that the received signal $\mathbf{x}(n)$ is covariance ergodic [74, pp. 531], such that the sample covariance matrix

$$\hat{\mathbf{R}}_{\mathbf{x}}(N) = \frac{1}{N-Q}\sum_{n=Q}^{N-1}\mathbf{x}(n)\mathbf{x}(n)^{\mathrm{H}} \tag{5.5}$$

asymptotically converges to the statistical covariance matrix, i. e.,

$$\lim_{N\to\infty}\hat{\mathbf{R}}_{\mathbf{x}}(N) = \mathbf{R}_{\mathbf{x}}. \tag{5.6}$$

The analytic derivations in this section target the well-known MME detector [45]. Its test statistic is composed of the eigenvalues of the received signal's sample covariance matrix. The test statistic and its accompanying decision rule are given by

$$\Gamma_{\mathrm{MME}}(\mathbf{x}, N) = \frac{\lambda_{\max}(\hat{\mathbf{R}}_{\mathbf{x}}(N))}{\lambda_{\min}(\hat{\mathbf{R}}_{\mathbf{x}}(N))} \underset{\mathcal{H}_1}{\overset{\mathcal{H}_0}{\lessgtr}} \gamma, \tag{5.7}$$

where $\lambda_{\max}(\cdot)$ and $\lambda_{\min}(\cdot)$ denote the largest and smallest eigenvalue of a matrix respectively and γ stands for the predefined decision threshold. If $\Gamma_{\mathrm{MME}}(\mathbf{x}, N) < \gamma$, we decide $\mathcal{H}_0$, while for $\Gamma_{\mathrm{MME}}(\mathbf{x}, N) \geq \gamma$ we decide $\mathcal{H}_1$. Since both sample and statistical covariance matrices are positive-semidefinite and thus all of their eigenvalues are ≥ 0, the test statistic $\Gamma_{\mathrm{MME}}(\mathbf{x}, N)$ is always ≥ 1.

5.1.3 SNR Walls in Spectrum Sensing

Additive white Gaussian noise (AWGN) is a standard assumption in wireless communications research and for many problems in the field, it is a reasonable one. Indeed, a classical result from information theory states that additive Gaussian noise represents the worst case in point-to-point communication [75], which makes it a fair choice for performance evaluation. However, modeling the receiver noise as AWGN is only an approximation of reality and for eigenvalue-based spectrum sensing, where correlation in the received signal is the key to differentiability between the $\mathcal{H}_0$ and the $\mathcal{H}_1$ case, it does not embody the worst case. As is shown in the subsequent parts of this section, the assumption that the (Gaussian) noise samples are i.i.d. (and thus the noise is *white*) is a crucial prerequisite for the MME detector's optimal operation.

To take into consideration that different types of noise exist, we model $\eta(n)$ as having any distribution W from a set of possible distributions $\mathcal{W}$, all of which have the variance σ_η^2. The MME detector is a general spectrum sensing algorithm in the sense that it is capable of detecting different kinds of signals. Thus, we do not assume a fixed signal type but instead only make the assumption that the PU signal $s(n)$ has any distribution S from the set of possible distributions $\mathcal{S}$, all of which have the variance σ_s^2.

Given the sets $\mathcal{S}$ and $\mathcal{W}$ with the variances σ_s^2 and σ_η^2 respectively, we can now define the SNR as

$$\mathrm{SNR} = \frac{\sigma_s^2}{\sigma_\eta^2}. \tag{5.8}$$

Further, we define the probability of false alarm and the probability of missed detection as

$$\begin{aligned} P_{\mathrm{fa}}(W, N) &= P(\Gamma_{\mathrm{MME}}(\mathbf{x}, N) \geq \gamma \mid \mathcal{H}_0, W), \\ P_{\mathrm{md}}(W, S, N) &= P(\Gamma_{\mathrm{MME}}(\mathbf{x}, N) < \gamma \mid \mathcal{H}_1, W, S), \end{aligned} \tag{5.9}$$

respectively. In conformity with the definition in [30] (except that we do not consider a fading channel), we let a detector *robustly* achieve a pair $(P_{\text{fa}}, P_{\text{md}})$ consisting of a target false alarm probability P_{fa} and a target missed detection probability P_{md} if it satisfies

$$\begin{aligned} \sup_{W \in \mathcal{W}} P_{\text{fa}}(W, N) &\leq P_{\text{fa}}, \\ \sup_{W \in \mathcal{W}, S \in \mathcal{S}} P_{\text{md}}(W, S, N) &\leq P_{\text{md}}. \end{aligned} \tag{5.10}$$

The detector is called non-robust at a given SNR if at that SNR even with an arbitrarily high N, it cannot achieve any pair $(P_{\text{fa}}, P_{\text{md}})$ on the support $P_{\text{fa}} \in [0, 0.5], P_{\text{md}} \in [0, 0.5]$. The SNR-wall is finally defined as

$$\begin{aligned} \text{SNR}_{\text{wall}} = \sup\{\text{SNR}_t, \text{ s.t. the detector is non-robust} \\ \text{for all SNR} < \text{SNR}_t\}. \end{aligned} \tag{5.11}$$

For test statistics with symmetric PDFs, a definition of non-robustness equivalent to the above is that a detector is non-robust iff the sets of means of the test statistic $\Gamma(\mathbf{x}, N)$ under the two hypotheses overlap [30]. However, the $\mathcal{H}_0$ and $\mathcal{H}_1$ test statistic PDFs of the MME detector are not symmetric. Thus, we use a third definition of non-robustness, which states that a detector is non-robust iff the sets of medians of the test statistic $\Gamma(\mathbf{x}, N)$ under the two hypotheses overlap. This definition is equivalent to the first one, even for non-symmetric distributions. For symmetric distributions, it coincides with the second definition. We make use of the third version of the definition of an SNR-wall when deriving a lower bound on the SNR-wall for the MME detector, thus proving the existence of an SNR-wall for that detector, in Section 5.1.5.

5.1.4 Sources of Noise and Noise Coloring

As mentioned in Section 5.1.3, AWGN can only be considered an approximation of the actual noise experienced at a radio receiver. In this section we make the case for considering colored receiver noise, which is an assumption used in the subsequent parts of this section to prove the existence of an SNR-wall for the MME detector.

In [45] it is assumed that the receiver noise before processing is white and that the only source of noise coloring is the use of a receive filter. The receive filter is assumed to be known in advance and to be invertible, such that a pre-whitening filter can be used to re-whiten the received samples before including them in the computation of the test statistic. On close inspection, it seems to be problematic to remove all coloring, since perfect filter design is hardly achievable, which makes employing an exact inverse of the receive filter seem impossible.

Even if the coloring caused by the receiver architecture was perfectly reversible, the assumption that the external noise is white represents an oversimplification, which in the

case of the MME detector happens to be inappropriate, since for this detector uncorrelated noise is a requirement for proper functioning. In reality, the external noise is a superposition of different kinds of noise from various sources and although the impact of external noise decreases for higher frequencies [76], at moderate frequencies such as the ones used for television broadcasting, external noise is present and should be considered. Note that the television bands are of utmost interest for spectrum sensing, i. e., many spectrum sensing algorithms originated in the context of the IEEE 802.22 standard [72], which is concerned with communication in vacant television bands.

There are multiple different sources of realistic non-white external noise. One example is galactic radiation noise. The power spectral density (PSD) of such noise is proportional to $\frac{1}{f^{2.7}}$ [77], where f denotes the frequency, which makes it non-white. Another example is man-made noise [78]. The reason this kind of noise leads to correlation in the received samples under $\mathcal{H}_0$ is twofold. Firstly, it occurs in strong bursts that affect multiple receiver samples, which leads to time correlation. Secondly, when multiple receivers or multiple receive antennas are considered, the received noise is correlated in the case that multiple of them are in the range of the same man-made impulsive noise. The origin of man-made noise lies in, e. g., unintended radiation from electrical machinery or power transmission lines. Furthermore, nearly every electronic device creates it and thus, impulsive man-made noise is an effect that needs to be taken into account.

Given the above reasoning, it can arguably be expected that even in the absence of a PU signal in the observed band, a certain amount of correlation is present in the received samples.

5.1.5 SNR-Wall Lower Bound

In this section, we derive a lower bound on the SNR-wall of the MME detector, thus proving its existence. More specifically, following the definition of the SNR-wall from Section 5.1.3, we derive a lower bound on the SNR value below which the sets of medians of the test statistic $\Gamma(\mathbf{x}, N)$ under the two hypotheses ($\mathcal{H}_0$ and $\mathcal{H}_1$) overlap even in the asymptotic case ($N \to \infty$). To determine the location of the overlap we provide a lower bound on the test statistic under $\mathcal{H}_0$ and an upper bound on the test statistic under $\mathcal{H}_1$. The SNR below which the first of these two bounds has a higher value than the second one is the lower bound on the SNR-wall. Due to the fact that for $N \to \infty$, the PDFs of the test statistic under the two hypotheses both become degenerate distributions, such that the PDFs coincide with their medians, this is equivalent to the above definition of the SNR-wall.

Note, that in our system model the matrices $\mathbf{R_s}$ and $\mathbf{R}_{\boldsymbol{\eta}}$ are no Toeplitz matrices. The reason for this can be found in the composition of the vector $\mathbf{x}(n)$, i. e., the covariance matrices contain two types of correlation, time and receiver correlation (cf. (5.2)). The matrices are no Toeplitz matrices despite the facts that firstly, due to our asymptotic approach, the matrices are statistical covariance matrices and secondly, the underlying

noise processes are assumed to be stationary. The correlation coefficients associated with the entry in the i-th row and j-th column of $\mathbf{R_s}$ and $\mathbf{R}_{\boldsymbol{\eta}}$ are denoted by ρ^s_{ij} and ρ^{η}_{ij}, respectively. Bounds are denoted by a bar above the respective symbol.

Lower Bound on the Test Statistic Under $\mathcal{H}_0$ In the $\mathcal{H}_0$ case, $\mathbf{R_x} = \mathbf{R}_{\boldsymbol{\eta}}$, since no PU signal exists. For this case, we aim at finding a *lower* bound $\bar{\Gamma}^{\text{asym, lo}}_{\text{MME},\mathcal{H}_0}$ on the asymptotic test statistic, i. e.,

$$\frac{\bar{\lambda}^{\text{lo}}_{\max}(\mathbf{R}_{\boldsymbol{\eta}})}{\bar{\lambda}^{\text{up}}_{\min}(\mathbf{R}_{\boldsymbol{\eta}})} = \bar{\Gamma}^{\text{asym, lo}}_{\text{MME},\mathcal{H}_0} \leq \Gamma^{\text{asym}}_{\text{MME},\mathcal{H}_0} = \frac{\lambda_{\max}(\mathbf{R}_{\boldsymbol{\eta}})}{\lambda_{\min}(\mathbf{R}_{\boldsymbol{\eta}})}. \tag{5.12}$$

To obtain the lower bound $\bar{\Gamma}^{\text{asym, lo}}_{\text{MME},\mathcal{H}_0}$, we need to determine a lower bound on the largest eigenvalue ($\bar{\lambda}^{\text{lo}}_{\max}(\mathbf{R}_{\boldsymbol{\eta}})$) and an upper bound on the smallest eigenvalue ($\bar{\lambda}^{\text{up}}_{\min}(\mathbf{R}_{\boldsymbol{\eta}})$), i. e.,

$$\begin{aligned} \bar{\lambda}^{\text{lo}}_{\max}(\mathbf{R}_{\boldsymbol{\eta}}) &\leq \lambda_{\max}(\mathbf{R}_{\boldsymbol{\eta}}), \\ \bar{\lambda}^{\text{up}}_{\min}(\mathbf{R}_{\boldsymbol{\eta}}) &\geq \lambda_{\min}(\mathbf{R}_{\boldsymbol{\eta}}). \end{aligned} \tag{5.13}$$

According to the Courant-Fischer theorem, the maximum and minimum eigenvalues $\lambda_{\max}(\mathbf{H})$ and $\lambda_{\min}(\mathbf{H})$ of a hermitian matrix $\mathbf{H}$ can be obtained by solving the following optimization problems [79]

$$\begin{aligned} \lambda_{\max}(\mathbf{H}) &= \max_{\mathbf{z}:\mathbf{z}^{\text{H}}\mathbf{z}=1} \mathbf{z}^{\text{H}}\mathbf{H}\mathbf{z}, \\ \lambda_{\min}(\mathbf{H}) &= \min_{\mathbf{z}:\mathbf{z}^{\text{H}}\mathbf{z}=1} \mathbf{z}^{\text{H}}\mathbf{H}\mathbf{z}. \end{aligned} \tag{5.14}$$

From (5.14) it directly follows, that

$$\lambda_{\min}(\mathbf{H}) \leq \mathbf{z}^{\text{H}}\mathbf{H}\mathbf{z} \leq \lambda_{\max}(\mathbf{H}), \tag{5.15}$$

for an arbitrary normalized $\mathbf{z}$. This means, that we can obtain the bounds $\bar{\lambda}^{\text{lo}}_{\max}(\mathbf{R}_{\boldsymbol{\eta}})$ and $\bar{\lambda}^{\text{up}}_{\min}(\mathbf{R}_{\boldsymbol{\eta}})$ by simply evaluating $\bar{\lambda}^{\text{lo}}_{\max}(\mathbf{R}_{\boldsymbol{\eta}}) = \mathbf{z}_1^{\text{H}}\mathbf{R}_{\boldsymbol{\eta}}\mathbf{z}_1$ and $\bar{\lambda}^{\text{up}}_{\min}(\mathbf{R}_{\boldsymbol{\eta}}) = \mathbf{z}_2^{\text{H}}\mathbf{R}_{\boldsymbol{\eta}}\mathbf{z}_2$ using two arbitrary normalized vectors $\mathbf{z}_1$ and $\mathbf{z}_2$. However, an additional constraint we need to take care of when obtaining the bounds is that $\bar{\lambda}^{\text{lo}}_{\max}(\mathbf{R}_{\boldsymbol{\eta}}) \geq \bar{\lambda}^{\text{up}}_{\min}(\mathbf{R}_{\boldsymbol{\eta}})$ needs to hold. In the following, we construct a set of vectors $\mathbf{z}_1$ and $\mathbf{z}_2$ that guarantees that this property is satisfied.

Given a specific covariance matrix $\mathbf{R}_{\boldsymbol{\eta}}$, the vectors are constructed as to extract its largest correlation coefficient $\rho^{\eta}_{\max}$ with $|\rho^{\eta}_{\max}| \geq |\rho^{\eta}_{ij}| \,\forall\, i, j$ with $i \neq j$. For the below example, we assume that the largest correlation coefficient is located at the k-th column of the first row of the matrix. Given the hermitian structure of covariance matrices and the assumed stationarity of the noise processes, this assumption can be made without loss of generality. The considered covariance matrix has the following structure

$$\mathbf{R}_{\boldsymbol{\eta}} = \sigma^2_{\eta} \begin{pmatrix} 1 & \cdots & |\rho^{\eta}_{\max}|e^{j\phi} & \cdots \\ \vdots & \ddots & \cdots & \cdots \\ |\rho^{\eta}_{\max}|e^{-j\phi} & \cdots & 1 & \cdots \\ \vdots & \vdots & \vdots & \ddots \end{pmatrix}. \tag{5.16}$$

The accompanying vectors $\mathbf{z}_1$ and $\mathbf{z}_2$ are given by

$$\begin{aligned}\mathbf{z}_1 &= \frac{1}{\sqrt{2}}[1, 0, \ldots, 0, +e^{-j\phi}, 0, \ldots, 0]^{\mathrm{T}},\\ \mathbf{z}_2 &= \frac{1}{\sqrt{2}}[1, 0, \ldots, 0, -e^{-j\phi}, 0, \ldots, 0]^{\mathrm{T}},\end{aligned} \tag{5.17}$$

where $\pm e^{-j\phi}$ is the k-th element of the respective vector, coinciding with the position of $|\rho^{\eta}_{\max}|e^{\pm j\phi}$ in $\mathbf{R}_{\boldsymbol{\eta}}$. We can now obtain

$$\begin{aligned}\bar{\lambda}^{\mathrm{lo}}_{\max}(\mathbf{R}_{\boldsymbol{\eta}}) &= \mathbf{z}_1^{\mathrm{H}}\mathbf{R}_{\boldsymbol{\eta}}\mathbf{z}_1 = \sigma_\eta^2(1 + |\rho^{\eta}_{\max}|),\\ \bar{\lambda}^{\mathrm{up}}_{\min}(\mathbf{R}_{\boldsymbol{\eta}}) &= \mathbf{z}_2^{\mathrm{H}}\mathbf{R}_{\boldsymbol{\eta}}\mathbf{z}_2 = \sigma_\eta^2(1 - |\rho^{\eta}_{\max}|).\end{aligned} \tag{5.18}$$

Note that the above argument can be made for an arbitrary position of $\rho^{\eta}_{\max}$ by choosing $\mathbf{z}_1$ and $\mathbf{z}_2$ accordingly, leaving (5.18) unchanged. Note also, that $\bar{\lambda}^{\mathrm{lo}}_{\max}(\mathbf{R}_{\boldsymbol{\eta}}) \geq \bar{\lambda}^{\mathrm{up}}_{\min}(\mathbf{R}_{\boldsymbol{\eta}})$ holds. The lower bound on the test statistic under $\mathcal{H}_0$ is now given by

$$\bar{\Gamma}^{\text{asym, lo}}_{\mathrm{MME},\mathcal{H}_0} = \frac{1 + |\rho^{\eta}_{\max}|}{1 - |\rho^{\eta}_{\max}|}, \tag{5.19}$$

for $0 \leq |\rho^{\eta}_{\max}| < 1$. For the case of complete noise correlation, i. e., $|\rho^{\eta}_{\max}| = 1$ we get $0 \leq \lambda_{\min}(\mathbf{R}_{\boldsymbol{\eta}}) \leq \bar{\lambda}^{\mathrm{up}}_{\min}(\mathbf{R}_{\boldsymbol{\eta}}) = 0$, where the first inequality is due to the general positive semidefiniteness of covariance matrices. Since for $\lambda_{\min}(\mathbf{R}_{\boldsymbol{\eta}}) = 0$ detection becomes impossible (cf. (5.7)), we exclude the case of complete noise correlation.

Upper Bound on the Test Statistic Under $\mathcal{H}_1$ In the $\mathcal{H}_1$ case, $\mathbf{R}_{\mathbf{x}} = \mathbf{R}_{\mathbf{s}} + \mathbf{R}_{\boldsymbol{\eta}}$. For this case, we aim at finding an *upper* bound $\bar{\Gamma}^{\text{asym, up}}_{\mathrm{MME},\mathcal{H}_1}$ on the asymptotic test statistic, i. e.,

$$\frac{\bar{\lambda}^{\mathrm{up}}_{\max}(\mathbf{R}_{\mathbf{x}})}{\bar{\lambda}^{\mathrm{lo}}_{\min}(\mathbf{R}_{\mathbf{x}})} = \bar{\Gamma}^{\text{asym, up}}_{\mathrm{MME},\mathcal{H}_1} \geq \Gamma^{\text{asym}}_{\mathrm{MME},\mathcal{H}_1} = \frac{\lambda_{\max}(\mathbf{R}_{\mathbf{x}})}{\lambda_{\min}(\mathbf{R}_{\mathbf{x}})}. \tag{5.20}$$

To obtain the upper bound $\bar{\Gamma}^{\text{asym, up}}_{\mathrm{MME},\mathcal{H}_1}$, we need to determine an upper bound on the largest eigenvalue ($\bar{\lambda}^{\mathrm{up}}_{\max}(\mathbf{R}_{\mathbf{x}})$) and a lower bound on the smallest eigenvalue ($\bar{\lambda}^{\mathrm{lo}}_{\min}(\mathbf{R}_{\mathbf{x}})$), i. e.,

$$\begin{aligned}\bar{\lambda}^{\mathrm{up}}_{\max}(\mathbf{R}_{\mathbf{x}}) &\geq \lambda_{\max}(\mathbf{R}_{\mathbf{x}}),\\ \bar{\lambda}^{\mathrm{lo}}_{\min}(\mathbf{R}_{\mathbf{x}}) &\leq \lambda_{\min}(\mathbf{R}_{\mathbf{x}}).\end{aligned} \tag{5.21}$$

Let r_{ij} denote the entry of $\mathbf{R}_{\mathbf{x}}$ in the i-th row and j-th column. Given our assumptions from Section 5.1.2, we get

$$\begin{aligned}r_{ii} &= \sigma_\eta^2 + \sigma_s^2 = (1 + \mathrm{SNR})\sigma_\eta^2,\\ r_{ij} &= \sigma_\eta^2\rho^{\eta}_{ij} + \sigma_s^2\rho^{s}_{ij} = (\rho^{\eta}_{ij} + \mathrm{SNR}\,\rho^{s}_{ij})\sigma_\eta^2.\end{aligned} \tag{5.22}$$

According to the Gershgorin circle theorem [80], all eigenvalues $\lambda_k|_{k=1}^{g}$ of a matrix $\mathbf{A} \in \mathbb{C}^{g\times g}$, with $g = p(Q+1)$, lie within the union of the circular disks

$$\{z \in \mathbb{C} : |z - a_{ii}| \leq R_i\}, \tag{5.23}$$

where

$$R_i = \sum_{\substack{j=1 \\ j\neq i}}^{g} |a_{ij}|. \tag{5.24}$$

Since $\mathbf{R_x}$ is hermitian, all of its eigenvalues are real and thus the disks from (5.23) become intervals on the real axis. The value of r_{ii} is independent of i. Thus, an upper bound on the maximum eigenvalue of $\mathbf{R_x}$ can be obtained as

$$\begin{aligned} \bar{\lambda}_{\max}^{\text{up}}(\mathbf{R_x}) &= |r_{ii}| + \max_i R_i \\ &= \sigma_\eta^2(\text{SNR}+1 + \max_i \sum_{\substack{j=1 \\ j\neq i}}^{g} |(\rho_{ij}^{\eta} + \text{SNR}\,\rho_{ij}^{s})|) \\ &\geq \lambda_{\max}(\mathbf{R_x}). \end{aligned} \tag{5.25}$$

In analogy to (5.25), a lower bound on the minimum eigenvalue of $\mathbf{R_x}$ can be obtained as

$$\begin{aligned} \bar{\lambda}_{\min}^{\text{lo}}(\mathbf{R_x}) &= |r_{ii}| - \max_i R_i \\ &= \sigma_\eta^2(\text{SNR}+1 - \max_i \sum_{\substack{j=1 \\ j\neq i}}^{g} |(\rho_{ij}^{\eta} + \text{SNR}\,\rho_{ij}^{s})|) \\ &\leq \lambda_{\min}(\mathbf{R_x}). \end{aligned} \tag{5.26}$$

However, for (5.26) to be a valid bound in terms of the test statistic, we need to introduce an extra constraint. We need to make sure that $\bar{\lambda}_{\min}^{\text{lo}}(\mathbf{R_x}) > 0$, i. e., $|r_{ii}| - \max_i R_i > 0$, which leads to the constraint

$$1 + \text{SNR} > \max_i \sum_{\substack{j=1 \\ j\neq i}}^{g} |(\rho_{ij}^{\eta} + \text{SNR}\,\rho_{ij}^{s})|. \tag{5.27}$$

Combining (5.25) and (5.26) finally provides the upper bound on the asymptotic test statistic under $\mathcal{H}_1$ given by

$$\bar{\Gamma}_{\text{MME},\mathcal{H}_1}^{\text{asym, up}} = \frac{\text{SNR}+1 + \max_i \sum_{\substack{j=1 \\ j\neq i}}^{g} |(\rho_{ij}^{\eta} + \text{SNR}\,\rho_{ij}^{s})|}{\text{SNR}+1 - \max_i \sum_{\substack{j=1 \\ j\neq i}}^{g} |(\rho_{ij}^{\eta} + \text{SNR}\,\rho_{ij}^{s})|}. \tag{5.28}$$

Lower Bound on the SNR-Wall Combining (5.19) and (5.28), we can say that the MME detector is non-robust under the condition given by (5.27) and given that $\rho^{\eta}_{\max} < 1$ when $\bar{\Gamma}^{\text{asym, up}}_{\text{MME},\mathcal{H}_1} \leq \bar{\Gamma}^{\text{asym, lo}}_{\text{MME},\mathcal{H}_0}$, i. e.,

$$\frac{\text{SNR} + 1 + \max\limits_{i} \sum\limits_{\substack{j=1 \\ j\neq i}}^{g} |(\rho^{\eta}_{ij} + \text{SNR}\,\rho^{s}_{ij})|}{\text{SNR} + 1 - \max\limits_{i} \sum\limits_{\substack{j=1 \\ j\neq i}}^{g} |(\rho^{\eta}_{ij} + \text{SNR}\,\rho^{s}_{ij})|} \leq \frac{1 + |\varrho^{\eta}_{\max}|}{1 - |\varrho^{\eta}_{\max}|}. \tag{5.29}$$

Note, that the correlation coefficients in the $\mathcal{H}_0$ case are now denoted by ϱ instead of ρ to facilitate the distinction between the noise correlation in the $\mathcal{H}_0$ and the $\mathcal{H}_1$ case. For the interpretation of (5.29) it is important to note, that $\rho^{s}_{ij} \geq 0 \; \forall \; i, j$, i. e., the signal correlation coefficients never become negative. This follows from (5.2), (5.4) and the assumption that consecutive symbols are independent.

5.1.6 Examples of the Lower Bound on the SNR-Wall

Inequality (5.29) is quite involved and does not allow for easy interpretation. Since our goal is to prove the existence of an SNR-wall, we continue our investigation with examples that simplify (5.29), facilitating interpretation. We consider the case, where under $\mathcal{H}_1$ no noise correlation exists, i. e., $\rho^{\eta}_{ij} = 0 \; \forall \; i, j$ except $i = j$, while under $\mathcal{H}_0$, the noise is correlated, i. e., $\exists \; (i, j)$ with $i \neq j$ for which $\varrho^{\eta}_{ij} \neq 0$. This case occurs when the sources of noise coloring in the vicinity of the sensor are only present at certain times or if the sensor is used at different locations. Considering uncorrelated noise under $\mathcal{H}_1$, (5.27) can be simplified as follows

$$\begin{aligned} 1 + \text{SNR} &> \max_{i} \sum_{\substack{j=1 \\ j\neq i}}^{g} |(\rho^{\eta}_{ij} + \text{SNR}\,\rho^{s}_{ij})| \\ \Leftrightarrow 1 + \text{SNR} &> \text{SNR} \cdot \max_{i} \sum_{\substack{j=1 \\ j\neq i}}^{g} |\rho^{s}_{ij}| \\ \Leftrightarrow \text{SNR} &< \frac{1}{\kappa_{\max} - 1}, \end{aligned} \tag{5.30}$$

where

$$\kappa_{\max} = \max_{i} \sum_{\substack{j=1 \\ j\neq i}}^{g} |\rho^{s}_{ij}|. \tag{5.31}$$

This means, that the higher the correlation in the signal samples, the lower the SNR for which our lower bound is defined. For $\kappa_{\max} < 1$, the condition is never satisfied. In this case, we have to fall back to zero as a lower bound for $\lambda_{\min}$, which is guaranteed by

the properties of covariance matrices. This however leads to the test statistic under $\mathcal{H}_0$ taking the value infinity, which again rules out the possibility of giving a lower bound for an SNR-wall. For a more concise notation, let

$$\alpha_{\max} = \bar{\Gamma}^{\text{asym, lo}}_{\text{MME},\mathcal{H}_0} = \frac{1 + |\varrho^{\eta}_{\max}|}{1 - |\varrho^{\eta}_{\max}|}. \tag{5.32}$$

By assuming a minimal amount of noise coloring under $\mathcal{H}_0$ and excluding the case of complete noise correlation, we restricted the support of the largest noise correlation coefficient, such that $\varrho_{\max} \in (0, 1)$. As a consequence, it holds that $\alpha_{\max} > 1$. Using the definitions of $\kappa_{\max}$ and $\alpha_{\max}$, as well as the assumption that under $\mathcal{H}_1$ the noise is uncorrelated, (5.29) becomes

$$\frac{\text{SNR} + 1 + \kappa_{\max}\,\text{SNR}}{\text{SNR} + 1 - \kappa_{\max}\,\text{SNR}} \leq \alpha_{\max}, \tag{5.33}$$

or equivalently

$$\text{SNR} \leq \frac{\alpha_{\max} - 1}{1 + \kappa_{\max} + \alpha_{\max}(\kappa_{\max} - 1)}. \tag{5.34}$$

In order to obtain concrete numbers for the bound, we look at more specific examples in the following.

(A) Receiver Correlation ($Q = 0$, $p \geq 2$) In this example we consider a p-receiver setup with perfect signal correlation, i. e., $\rho^{s}_{ij} = 1 \;\forall\; i, j$. The maximum signal correlation in this case is $\kappa_{\max} = p - 1$ and thus the condition (5.30) becomes $\text{SNR} < \frac{1}{p-2}$. If the condition is satisfied, we can say that the MME detector becomes non-robust for

$$\text{SNR} \leq \frac{\alpha_{\max} - 1}{p + \alpha_{\max}(p - 2)}. \tag{5.35}$$

For $p = 2$ and a maximum noise correlation of $\varrho^{\eta}_{\max} = 0.05$, which we consider to be moderate noise coloring, we arrive at a lower bound of $\text{SNR} = 0.052632 = -12.788$ dB, which is considerably far away from -22 dB (cf. Section 5.1.1). This example is simple enough for us to obtain the actual statistical covariance matrices for an evaluation of the bound's tightness. They are given by

$$\begin{aligned} \mathbf{R}^{\mathcal{H}_0}_{\mathbf{x}} &= \mathbf{R}^{\mathcal{H}_0}_{\boldsymbol{\eta}} = \sigma^2_{\eta} \begin{pmatrix} 1 & 0.05 \\ 0.05 & 1 \end{pmatrix}, \\ \mathbf{R}^{\mathcal{H}_1}_{\mathbf{x}} &= \begin{pmatrix} \sigma^2_{\eta} + \sigma^2_{s} & \sigma^2_{s} \\ \sigma^2_{s} & \sigma^2_{\eta} + \sigma^2_{s} \end{pmatrix} \\ &= \sigma^2_{\eta} \begin{pmatrix} 1 + \text{SNR} & \text{SNR} \\ \text{SNR} & 1 + \text{SNR} \end{pmatrix}. \end{aligned} \tag{5.36}$$

With the above covariance matrices, the asymptotic test statistics evaluate to $\Gamma^{\text{asym}}_{\mathcal{H}_0} = 1.10503$ and $\Gamma^{\text{asym}}_{\mathcal{H}_1} = 1 + 2\,\text{SNR}$. This means, that for an SNR below $0.052632 = -12.788$ dB, $\Gamma^{\text{asym}}_{\mathcal{H}_1} < \Gamma^{\text{asym}}_{\mathcal{H}_0}$, such that the detector becomes non-robust, i. e., in this special case the bound is tight.

(B) Time Correlation ($p = 1$, $Q \geq 1$) To complement the receiver correlation example, we next investigate a case with only one receiver that examines the correlation of the received samples over time. In order to again obtain a bound via (5.34), the value of $\kappa_{\max}$ needs to be determined. Given an oversampling factor M and the independence of consecutive symbols, the autocorrelation function of the PU signal can be obtained as

$$\mathbb{E}\left[s^*(n)s(n \pm k)\right] = \begin{cases} \sigma_s^2(1 - \frac{k}{M}) & \text{if } |k| < M \\ 0 & \text{else.} \end{cases} \tag{5.37}$$

In our case, the row with the maximum off-diagonal correlation sum in $\mathbf{R_s}$ is the $\left\lfloor \frac{g+1}{2} \right\rfloor$-th one, where $g = Q + 1$ is the number of rows of $\mathbf{R_s}$ and $\lfloor \cdot \rfloor$ denotes the floor operation. This is illustrated in the following example for $Q = 3$ (assuming $M \geq 3$)

$$\mathbf{R_s} = \sigma_s^2 \begin{pmatrix} 1 & 1 - \frac{1}{M} & 1 - \frac{2}{M} & 1 - \frac{3}{M} \\ 1 - \frac{1}{M} & 1 & 1 - \frac{1}{M} & 1 - \frac{2}{M} \\ 1 - \frac{2}{M} & 1 - \frac{1}{M} & 1 & 1 - \frac{1}{M} \\ 1 - \frac{3}{M} & 1 - \frac{2}{M} & 1 - \frac{1}{M} & 1 \end{pmatrix}. \tag{5.38}$$

The further away from the diagonal, the smaller the value. Thus, the middle row has the highest sum.

In order to obtain $\kappa_{\max}$, three cases have to be distinguished. For $\left\lceil \frac{Q}{2} \right\rceil < M$ and Q even, we get

$$\begin{aligned} \kappa_{\max} &= 2 \sum_{j=1}^{\frac{Q}{2}} \left(1 - \frac{j}{M}\right) \\ &= Q - \frac{Q^2 + 2Q}{4M}, \end{aligned} \tag{5.39}$$

for $\left\lceil \frac{Q}{2} \right\rceil < M$ and Q odd, we get

$$\begin{aligned} \kappa_{\max} &= 2 \sum_{j=1}^{\frac{Q-1}{2}} \left(1 - \frac{j}{M}\right) + \left(1 - \frac{Q+1}{2M}\right) \\ &= Q - \frac{(Q+1)^2}{4M}, \end{aligned} \tag{5.40}$$

and for $\left\lceil \frac{Q}{2} \right\rceil \geq M$, we get

$$\kappa_{\max} = 2 \sum_{j=1}^{M-1} \left(1 - \frac{j}{M}\right) = M - 1, \tag{5.41}$$

where $\lceil \cdot \rceil$ denotes the ceiling operation. In this example we model the noise as a stationary auto-regressive process of order one (AR(1)). It is supposed to mimic white external

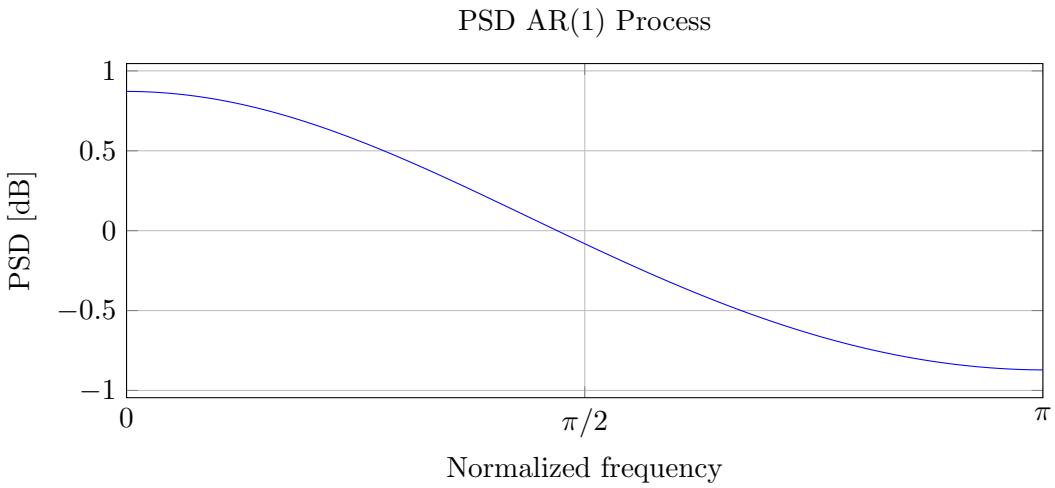

Figure 5.1: PSD of AR(1) process, which follows $\eta[n] = 0.1\eta[n-1] + \epsilon[n]$. The frequency is normalized to $f_{\text{samples}} = 2\pi$.

noise that has undergone filtering by a low-pass receive filter. The noise process is given by

$$\eta(n) = 0.1\eta(n-1) + \epsilon(n), \tag{5.42}$$

where $\epsilon(n)$ denotes an i.i.d. complex Gaussian random process with mean zero and variance 0.99. It is independent of $\eta(n-1)$, and has independent real and imaginary parts and $\mathbb{E}\left[|\eta[n]|^2\right] = 1$. Figure 5.1 shows the noise process's PSD to illustrate its characteristics. We consider the case of $Q = 3$ and $M = 4$, where the choice of Q leads to the noise covariance matrix

$$\mathbf{R}_{\boldsymbol{\eta}} = \begin{pmatrix} 1 & 0.1 & 0.1^2 & 0.1^3 \\ 0.1 & 1 & 0.1 & 0.1^2 \\ 0.1^2 & 0.1 & 1 & 0.1 \\ 0.1^3 & 0.1^2 & 0.1 & 1 \end{pmatrix} \tag{5.43}$$

and $\kappa_{\max} = 2$ (cf. (5.40)). Using (5.34), we again get a lower bound for the SNR-wall of -12.788 dB.

(C) Time and Receiver Correlation ($p > 1, Q > 0$) As a final example, we consider the case where both, time and receiver correlation, are exploited. Given our model assumption that the signal strength is equal for all receivers, we can combine the $\kappa_{\max}$ terms derived in the preceding subsections to obtain

$$\kappa_{\max} = p - 1 + p \cdot \kappa_{\max,\text{time}}, \tag{5.44}$$

where $\kappa_{\max,\text{time}}$ denotes the $\kappa_{\max}$ term for time correlation.

Table 5.1: Parameters

Parameter	Symbol	Value(s)
Modulation type		BPSK
Oversampling factor	M	4
Number of samples	N	$\{999, 9999, 999999\}$
# of Monte Carlo instances		2000
# of histogram bins		12

5.1.7 Numerical Evaluation

In this section we provide numerical results corresponding to examples A and B of Section 5.1.6. The parameters used in the simulations can be found in Table 5.1. For the $\mathcal{H}_1$ case we generate white Gaussian noise and an oversampled binary phase shift keying (BPSK) signal with a rectangular pulse shape and symbols that are independent of each other. For the $\mathcal{H}_0$ case we generate colored noise. The different noise types used for $\mathcal{H}_0$ and $\mathcal{H}_1$ represent the model uncertainty that has to be taken into account when designing spectrum sensing algorithms. When generating colored noise, our aim is to create a stationary, sampled Gaussian process with a predefined covariance matrix.

Receiver Correlation In the receiver correlation case, we use a matrix multiplication approach for generating colored noise. We start by generating the p-dimensional white Gaussian noise sample vector $\mathbf{w}(n) \sim \mathcal{CN}(\mathbf{0}, \mathbf{R}_\mathbf{w})$ for all time instances n, where $\mathbf{R}_\mathbf{w} = \mathbf{I}_{p\times p}$, while p is the number of receivers. That is, the vector $\mathbf{w}(n)$ is generated according to a p-dimensional zero-mean Gaussian distribution with the identity matrix as its covariance matrix. The colored noise vector $\boldsymbol{\eta}(n)$, which is experienced at the receiver in the $\mathcal{H}_0$ case, is subsequently obtained as $\boldsymbol{\eta}(n) = \mathbf{A}\mathbf{w}(n)$, where the matrix $\mathbf{A} \in \mathbb{C}^{p\times p}$ needs to be chosen such that the covariance matrix of $\boldsymbol{\eta}(n)$ equals the predefined $\mathbf{R}_{\boldsymbol{\eta}}$. This approach leads to the desired result due to the fact that linear combinations of Gaussian random variables are again distributed according to a Gaussian distribution. It is well known that the covariance matrix of $\mathbf{A}\mathbf{w}(n)$ is given by $\mathbf{A}^\mathrm{H}\mathbf{R}_\mathbf{w}\mathbf{A}$. Thus, the matrix $\mathbf{A}$ can be easily obtained by computing the Cholesky decomposition $\mathbf{R}_{\boldsymbol{\eta}} = \mathbf{A}^\mathrm{H}\mathbf{A}$.

Figure 5.2 shows the normalized histograms (PDF estimations) for the MME test statistic Γ_MME in the $\mathcal{H}_0$ case (black) and the $\mathcal{H}_1$ case (colored). For the $\mathcal{H}_1$ case, the test statistic histograms for different SNRs are shown. It can be observed that the estimation variance of the test statistic decreases with an increasing number of samples N, which is to be expected since asymptotically the sample covariance matrix converges to the statistical covariance matrix. What we can also see is that the mean of the estimated test statistic changes for an increasing N. This is a testimony to the biasedness of the estimator (5.7). Recall, that the lower bound on the SNR-wall for this scenario has been derived to be -12.788 dB. The simulation results confirm this bound. Indeed, when the SNR drops below the derived bound, the medians of the test statistics under $\mathcal{H}_1$ are

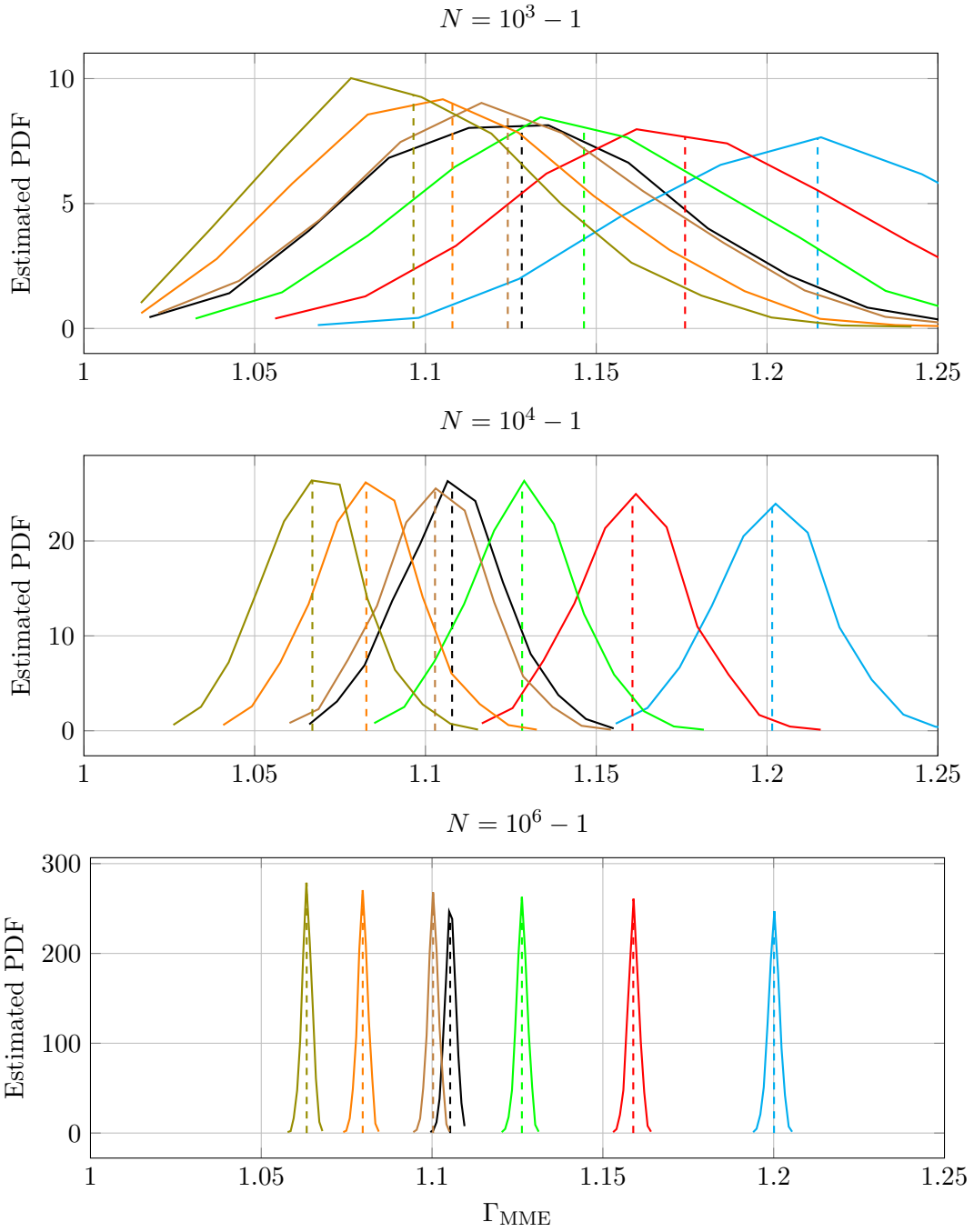

Figure 5.2: Estimated probability density function for receiver correlation ($p = 2, Q = 0$) and different N. Noise correlation factor $\varrho^{\eta}_{\max} = 0.05$. Solid lines represent the normalized histograms, while dashed lines depict the means. The $\mathcal{H}_0$ case result is shown in black, while the $\mathcal{H}_1$ case results are colored, where the SNR from right to left is given by $\{-10, -11, \ldots, -15\}$ dB.

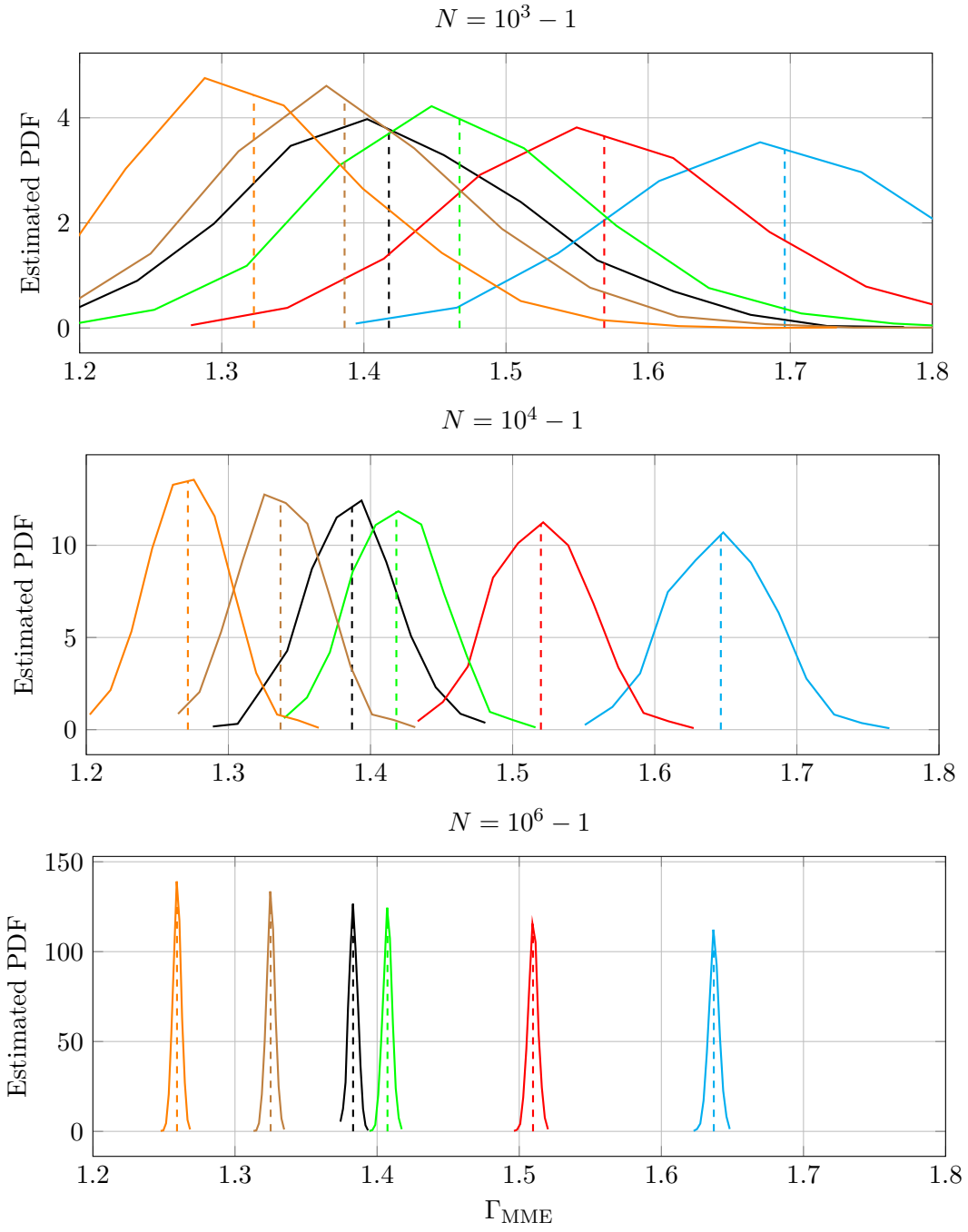

Figure 5.3: Estimated probability density function for time correlation ($p = 1$, $Q = 4$) and different N. Solid lines represent the normalized histograms, while dashed lines depict the means. The $\mathcal{H}_0$ case result is shown in black, while the $\mathcal{H}_1$ case results are colored, where the SNR from right to left is given by $\{-6, -7, \ldots, -10\}$ dB.

below the median of the test statistic under $\mathcal{H}_0$ for all inspected N, making the detector non-robust by definition.

A different point of view is assumed in Figure 5.4 ($P_{\text{fa}} = 0.01$), Figure 5.5 ($P_{\text{fa}} = 0.05$), Figure 5.6 ($P_{\text{fa}} = 0.10$) and Figure 5.7 ($P_{\text{fa}} = 0.50$). In these figures the missed detection rate P_{md} is plotted over the number of available samples N and the SNR for a fixed false alarm rate. A clear *wall* can be identified in all of them. We can see that below a certain SNR, detection is just not possible anymore, since the P_{md} goes to 1. Note however, that what we may intuitively make out as the wall in the figures is actually stronger than what we define as an SNR-wall. The actual SNR-wall as per definition can be found in Figure 5.7. The figure shows the missed detection rate for a fixed false alarm rate of 50%. The SNR-wall is the SNR value below which the missed detection rate P_{md} is above 0.5 for all N. In that figure we also see why it is important not to define the SNR-wall with 100% missed detection rate as may seem reasonable since only for $P_{\text{md}} = 1$ detection becomes truly *impossible*. For small numbers of samples, the PDFs of the test statistic under $\mathcal{H}_0$ and $\mathcal{H}_1$ become very wide, such that it is very unlikely that all of the $\mathcal{H}_1$ PDF is below the median of the $\mathcal{H}_0$ PDF. This can be easily seen in Figure 5.7. However, for a set $(P_{\text{fa}}, P_{\text{md}})$ worse than $(0.5, 0.5)$ the chances of making the right decision in the hypothesis test are worse than those of simply guessing, i. e., the chances are worse than those of a coin flip, such that using the test statistic does not make any sense in this regime.

Time Correlation Since in the previous example, the noise correlation only exists between the noise processes of different receivers but not between noise samples taken at a single receiver at different times, the matrix $\mathbf{A}$, which is used to color the noise, has a small dimension. This makes the matrix multiplication approach feasible for example A. To use the same method in the time correlation example, a coloring matrix of size $N \times N$ would be necessary, where in our simulations, N takes on values of up to 10^6. This renders the matrix multiplication approach infeasible for the current example. Thus, a different approach for generating colored noise has to be taken. First, we generate an autocorrelation with a real-valued PSD from an autoregressive model of order one. We then generate an N-dimensional vector distributed according to a zero-mean, unit-variance, complex, white Gaussian distribution, which serves as a frequency-domain noise basis. Its PSD is subsequently scaled by the PSD of the autocorrelation, after which it is transformed to the time-domain via the IDFT and scaled to variance σ_η^2. Here again, we use the fact, that a linear combination of Gaussian random variables is also distributed according to a Gaussian distribution.

Recall, that the lower bound on the SNR-wall for this scenario has been derived to be -12.788 dB. According to the numerical results (cf. Figure 5.3), in this scenario the MME detector exhibits an SNR-wall between -8 dB and -9 dB. While the lower bound cannot be called very tight for this example, it nevertheless proves the existence of an SNR-wall, which is guaranteed to be much higher than the desired -22 dB.

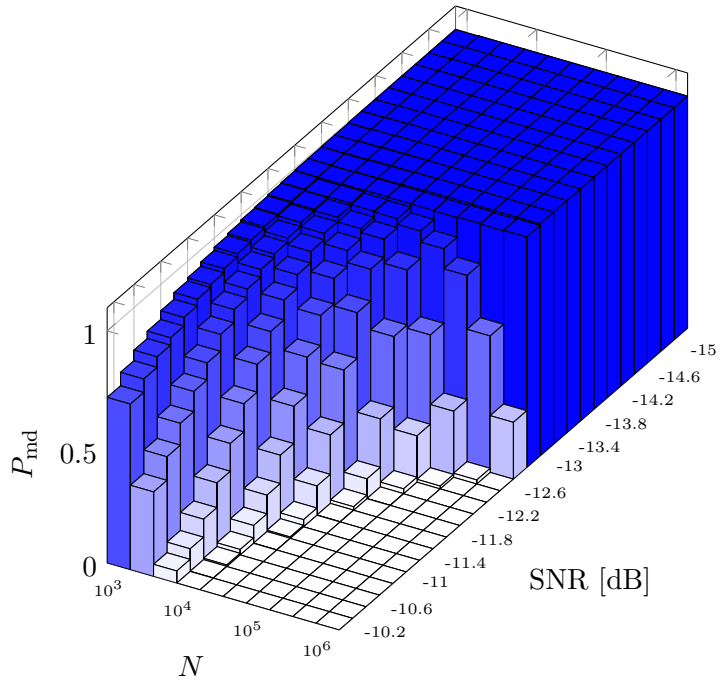

Figure 5.4: Missed detection rate (P_{md}) in the receiver correlation case ($p = 2$, $Q = 0$) for different numbers of samples and SNRs (in dB) at $P_{\mathrm{fa}} = 0.01$.

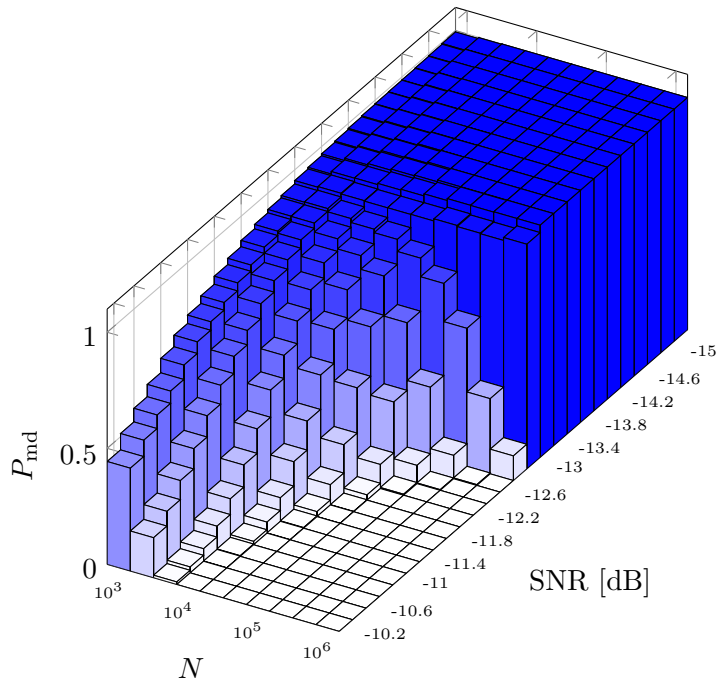

Figure 5.5: Missed detection rate (P_{md}) in the receiver correlation case ($p = 2$, $Q = 0$) for different numbers of samples and SNRs (in dB) at $P_{\mathrm{fa}} = 0.05$.

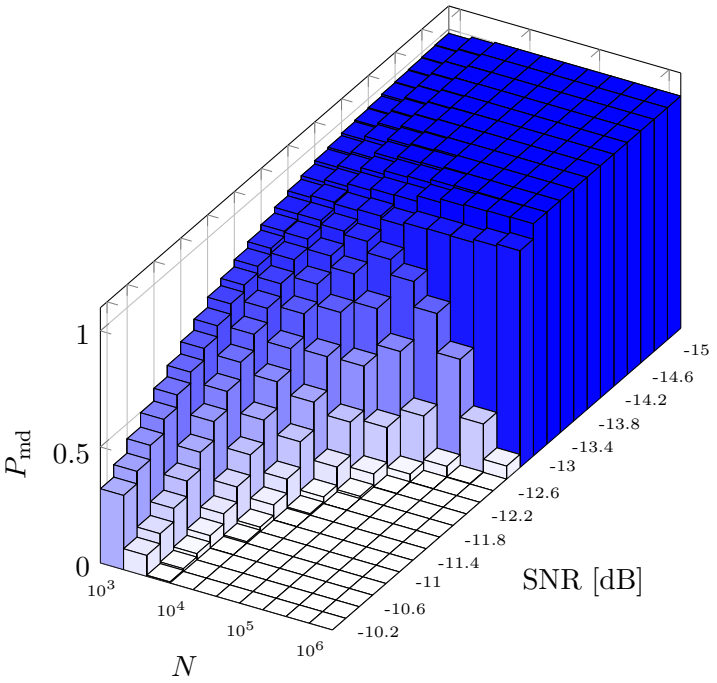

Figure 5.6: Missed detection rate (P_{md}) in the receiver correlation case ($p = 2$, $Q = 0$) for different numbers of samples and SNRs (in dB) at $P_{\text{fa}} = 0.1$.

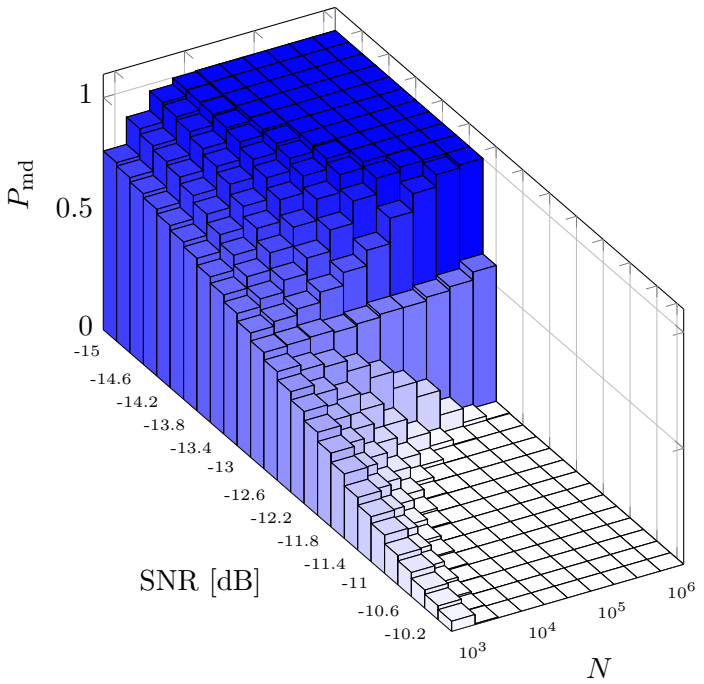

Figure 5.7: Missed detection rate (P_{md}) in the receiver correlation case ($p = 2$, $Q = 0$) for different numbers of samples and SNRs (in dB) at $P_{\text{fa}} = 0.5$.

5.1.8 Example of Noise Coloring: Impulsive Noise

In the preceding parts we have shown, that noise coloring, or more precisely, the amount of coloring contained in the noise at a SU receiver can lead to a so-called SNR-wall. As mentioned in Section 5.1.4, one of the sources of the potential noise coloring is the presence of impulsive noise in the vicinity of the receiver. To substantiate the claim, that impulsive noise leads to noise coloring, in this section we develop a noise model including impulsive noise and derive closed-form expressions for its influence on the autocorrelation of the receiver noise.

The presence of (man-made) impulsive noise in the vicinity of a SU receiver is a realistic assumption. The reason for this is the ubiquity of impulsive noise in all places frequented by humans. Indeed, it is caused by, e. g., non-linearities of electronic devices, by electronic devices being switched on or off and it can be unintended radiation from electrical machinery or power transmission lines. Nearly every electronic device or machine creates it. The strongest influence of such noise is found at lower frequencies, but even at frequencies around 500 MHz, the impact is significant [76]. Since this frequency band is used for terrestrial wireless television transmission, the effects of impulsive noise are to be taken into consideration in spectrum sensing.

Our noise model is based on a measurement campaign presented in [78], which reveals the characteristics of man-made impulsive noise. Two main observations have been made in the presence of a big number of impulsive noise emitting devices. The first one is, that the omnipresent white noise process, which consists of, e. g., thermal noise, has an increased power. The second observation is that strong peaks appear in the time domain. In [78], two types of impulsive noise are considered. Class A noise, which has a bandwidth that is comparable to that of the receiver or lower, and class B noise, which has a bandwidth much higher than that of the receiver. Since the authors of [78] state that class B noise is a valid representation for the impulsive noise in most measurements, we use it when building our noise model.

The usual way of modeling class B noise is given by [81, 78]

$$\eta(n) = \eta_{\mathrm{no}}(n) + c(n) \cdot \eta_{\mathrm{imp}}(n). \tag{5.45}$$

The white complex Gaussian base noise at time n is denoted by $\eta_{\mathrm{no}}(n)$, while the impulsive noise, which is often generated according to a Weibull distribution, is denoted by $\eta_{\mathrm{imp}}(n)$. The variable $c(n)$ follows a Bernoulli distribution and controls how often a noise impulse appears. Each of the three random processes are assumed to be i.i.d. with respect to n.

Due to the limited bandwidth, class A noise is bound to be correlated in time. While class B noise itself has a very high bandwidth, the receive filter of the sensor inevitably confines its bandwidth and thus introduces correlation in time. Since the authors of [78] state that the shape of the class B noise is mainly caused by the receive filter, we use the receive filter as a basis for the time correlation in our model.

The receive filter is modeled as a quasi-perfect lowpass filter with the time-constrained impulse response given by

$$h(n) = \begin{cases} \operatorname{sinc}(n) = \frac{\sin(\pi n)}{\pi n} & \text{if } |n| \leq F, \\ 0 & \text{else,} \end{cases} \tag{5.46}$$

where F determines the filter length of the lowpass filter. For $F \to \infty$, the filter is ideal.

Most of the white part of the noise is caused by internal imperfections of the receiver system, while the impulsive noise is external and traverses the receive filter before being sampled. Thus, we obtain the following expression for the overall receiver noise.

$$\boldsymbol{\eta}(n) = \boldsymbol{\eta}_{\mathrm{no}}(n) + \sum_{m=-F}^{F} c(n+m) \operatorname{sinc}\left(\frac{m + t(n+m)}{M}\right) \boldsymbol{\eta}_{\mathrm{imp}}(n+m). \tag{5.47}$$

Note, that instead of scalars, we now deal with vectors, which contain an entry for every receiver, i. e., $\boldsymbol{\eta}(n) = [\eta_1(n), \eta_2(n), \ldots, \eta_p(n)]^{\mathrm{T}}$, where the subscript indicates, which receiver the samples are from. The time shift between the continuous time noise impulse and the sampling clock is modeled by the random variable $t(n)$. The random variables are formally defined as follows:

- $\boldsymbol{\eta}_{\mathrm{no}}(n) \sim \mathcal{CN}(\mathbf{0}, \sigma_{\mathrm{no}}^2 \mathbf{I})$, i. e., it follows a circularly-symmetric complex Gaussian distribution with mean vector $\mathbf{0}$ and covariance matrix $\sigma_{\mathrm{no}}^2 \mathbf{I}$,
- $\boldsymbol{\eta}_{\mathrm{imp}}(n) \sim \mathcal{CN}(0, \mathbf{R}_{\mathrm{imp}})$ with power $k \cdot \sigma_{\mathrm{no}}^2$,
- $t(n) \sim \mathcal{U}(-0.5, 0.5)$, i. e., it is uniformly distributed on the interval $[-0.5, 0.5]$,
- $c(n) = \begin{cases} 1 & \text{with probability } \epsilon \\ 0 & \text{with probability } 1 - \epsilon, \end{cases}$
  i. e., it follows a Bernoulli distribution and has the power $\mathbb{E}\left[c(n)^2\right] = \epsilon$.

All four random processes are stochastically independent of each other, stationary and i.i.d. with respect to the time index n. The only source of time correlation in our model is the lowpass filter (5.46). Note, that $t(n)$ and $c(n)$ are scalar, such that an occurring impulse is always present at all receivers and exhibits the same time shift at all receivers. The amplitude of a pulse can differ from receiver to receiver, resulting in different receiver correlation values. This spatial correlation is represented by the values contained in $\mathbf{R}_{\mathrm{imp}}$. Since the maximum temporal distance between two dependent samples is finite ($2F + 1$, cf. (5.47)), the noise is still autocovariance ergodic.

In the following paragraphs, we derive closed-form expressions for the overall noise power as well as the noise correlation for the receiver correlation case, the time correlation case and the combination of the two based on our noise model (5.47). First we list some properties of our model that are useful for the subsequent derivations. Here, the symbol $\star$ is a wildcard, such that $\eta_\star$ stands for both, η_{no} and η_{imp}, while the additional subscript i or j indicates which receiver is meant.

$$\mathbb{E}\left[\eta^*_{\mathrm{no},i}(n)\cdot\eta_{\mathrm{no},j}(n)\right]=0 \quad \forall i\neq j. \tag{5.48}$$

$$\mathbb{E}\left[\eta^*_{\star,i}(m)\cdot\eta_{\star,i}(n)\right]=0 \quad \forall m\neq n. \tag{5.49}$$

$$\mathbb{E}\left[\eta^*_{\mathrm{no},i}(m)\cdot\eta_{\mathrm{imp},j}(n)\right]=0 \quad \forall m,n,i,j. \tag{5.50}$$

$$\mathbb{E}\left[\eta^*_{\mathrm{imp},i}(m)\cdot\eta_{\mathrm{imp},j}(n)\right]=0 \quad \forall m\neq n,\ i\neq j. \tag{5.51}$$

While (5.48) is due to the uncorrelatedness of the internal white noise of different receivers, the relation (5.49) expresses that the internal white noise as well as the external impulsive noise before filtering at a single receiver are uncorrelated over time. Equation (5.50) uses the fact that the internal white noise and the external impulsive noise are always independent of each other. Lastly, (5.51) expresses that the external impulsive noise at different receivers and different points in time is uncorrelated.

We can now obtain the overall noise power as

$$\begin{aligned}
&\mathbb{E}\left[\eta_i^*(n)\cdot\eta_i(n)\right]\\
&=\mathbb{E}\left[\left(\eta_{\mathrm{no},i}(n)+\sum_{m=-F}^{F}c(n+m)\,\mathrm{sinc}\left(\frac{m+t(n+m)}{M}\right)\eta_{\mathrm{imp},i}(n+m)\right)^*\right.\\
&\qquad\left.\left(\eta_{\mathrm{no},i}(n)+\sum_{m=-F}^{F}c(n+m)\,\mathrm{sinc}\left(\frac{m+t(n+m)}{M}\right)\eta_{\mathrm{imp},i}(n+m)\right)\right]\\
&\overset{(a)}{=}\mathbb{E}\left[|\eta_{\mathrm{no},i}(n)|^2\right]+\mathbb{E}\left[\left(\sum_{m=-F}^{F}c(n+m)\,\mathrm{sinc}\left(\frac{m+t(n+m)}{M}\right)\eta_{\mathrm{imp},i}(n+m)\right)^*\right.\\
&\qquad\left.\left(\sum_{m=-F}^{F}c(n+m)\,\mathrm{sinc}\left(\frac{m+t(n+m)}{M}\right)\eta_{\mathrm{imp},i}(n+m)\right)\right]\\
&\overset{(b)}{=}\sigma^2_{\mathrm{no}}+\mathbb{E}\left[\sum_{m=-F}^{F}c(n+m)^2\,\mathrm{sinc}^2\left(\frac{m+t(n+m)}{M}\right)|\eta_{\mathrm{imp},i}(n+m)|^2\right]\\
&=\sigma^2_{\mathrm{no}}+\sum_{m=-F}^{F}\mathbb{E}\left[c(n+m)^2\right]\cdot\mathbb{E}\left[|\eta_{\mathrm{imp},i}(n+m)|^2\right]\cdot\mathbb{E}\left[\mathrm{sinc}^2\left(\frac{m+t(n+m)}{M}\right)\right]\\
&=\sigma^2_{\mathrm{no}}+k\sigma^2_{\mathrm{no}}\epsilon\sum_{m=-F}^{F}\int_{-0.5}^{0.5}\mathrm{sinc}^2\left(\frac{m+t}{M}\right)\mathrm{d}t\\
&=\sigma^2_{\mathrm{no}}+k\sigma^2_{\mathrm{no}}\epsilon\underbrace{\int_{-F-0.5}^{F+0.5}\mathrm{sinc}^2\left(\frac{t}{M}\right)\mathrm{d}t}_{:=D_1(F,M)}\\
&=\sigma^2_{\mathrm{no}}+k\sigma^2_{\mathrm{no}}\,\epsilon\,D_1(F,M).
\end{aligned} \tag{5.52}$$

In (a), we use the fact that exploiting (5.50) we obtain,

$$\mathbb{E}\left[\eta^*_{\mathrm{no},i}(n)\sum_{m=-F}^{F} c(n+m)\,\mathrm{sinc}\left(\frac{m+t(n+m)}{M}\right)\eta_{\mathrm{imp},i}(n+m)\right]=0 \tag{5.53}$$

and

$$\mathbb{E}\left[\eta_{\mathrm{no},i}(n)\sum_{m=-F}^{F} c(n+m)\,\mathrm{sinc}\left(\frac{m+t(n+m)}{M}\right)\eta^*_{\mathrm{imp},i}(n+m)\right]=0. \tag{5.54}$$

In (b), we use property (5.49), which leads to

$$\begin{aligned}\mathbb{E}\Bigg[\sum_{m=-F}^{F}\sum_{\substack{l=-F\\ l\neq m}}^{F} c(n+m)\,\mathrm{sinc}\left(\frac{m+t(n+m)}{M}\right)\eta^*_{\mathrm{imp},i}(n+m)\\ c(n+l)\,\mathrm{sinc}\left(\frac{l+t(n+l)}{M}\right)\eta_{\mathrm{imp},i}(n+l)\Bigg]=0.\end{aligned} \tag{5.55}$$

As mentioned before, the value of F determines the quality of the receive filter. For large F, i. e., a good filter quality, the function $D_1(F,M)$ converges to M. A closed-form expression for the function $D_1(F,M)$ is given by

$$\begin{aligned}D_1(F,M)&=\int_{-F-0.5}^{F+0.5}\mathrm{sinc}^2\left(\frac{t}{M}\right)\mathrm{d}t\\ &=\left[\frac{M\left(\pi t\cdot\mathrm{Si}\left(\frac{2\pi t}{M}\right)-M\cdot\sin^2\left(\frac{\pi t}{M}\right)\right)}{\pi^2 t}\right]_{t=-F-0.5}^{t=F+0.5},\end{aligned} \tag{5.56}$$

where

$$\mathrm{Si}(x)=\int_0^x\frac{\sin(\zeta)}{\zeta}\mathrm{d}\zeta. \tag{5.57}$$

From (5.52), we can see that the overall noise power directly depends on the ratio k between the power of the internal white noise and the power of the external impulsive noise. Also, it becomes clear that the contribution of the impulsive noise is linearly scaled by the noise impulse occurrence frequency ϵ.

In the next step we derive the unnormalized *overall spatial* correlation coefficient. It represents the amount of correlation between two sensors which are located at different positions. We can normalize it by dividing it by the overall noise power, which was derived above. The *impulsive noise spatial* correlation coefficient between receiver i and receiver j is predefined and is given by

$$\mathbb{E}\left[\eta^*_{\mathrm{imp},i}[n]\eta_{\mathrm{imp},j}[n]\right]=\rho_{\mathrm{rec}}k\sigma^2_{\mathrm{no}}\quad\text{for } i\neq j. \tag{5.58}$$

The *overall spatial* correlation coefficient is given by

$$\begin{aligned}
&\mathbb{E}\left[\eta_i^*(n)\cdot\eta_j(n)\right]\\
&=\mathbb{E}\left[\left(\eta_{\mathrm{no},i}(n)+\sum_{m=-F}^{F}c(n+m)\,\mathrm{sinc}\left(\frac{m+t(n+m)}{M}\right)\eta_{\mathrm{imp},i}(n+m)\right)^*\right.\\
&\qquad\left.\left(\eta_{\mathrm{no},j}(n)+\sum_{m=-F}^{F}c(n+m)\,\mathrm{sinc}\left(\frac{m+t(n+m)}{M}\right)\eta_{\mathrm{imp},j}(n+m)\right)\right]\\
&\overset{(c)}{=}\mathbb{E}\left[\left(\sum_{m=-F}^{F}c(n+m)\,\mathrm{sinc}\left(\frac{m+t(n+m)}{M}\right)\eta_{\mathrm{imp},i}^*(n+m)\right)\right.\\
&\qquad\left.\left(\sum_{m=-F}^{F}c(n+m)\,\mathrm{sinc}\left(\frac{m+t(n+m)}{M}\right)\eta_{\mathrm{imp},j}(n+m)\right)\right]\\
&\overset{(d)}{=}\sum_{m=-F}^{F}\mathbb{E}\left[c(n+m)^2\right]\cdot\mathbb{E}\left[\eta_{\mathrm{imp},i}^*(n+m)\eta_{\mathrm{imp},j}(n+m)\right]\\
&\qquad\cdot\mathbb{E}\left[\mathrm{sinc}^2\left(\frac{m+t(n+m)}{M}\right)\right]\\
&=\epsilon k\sigma_{\mathrm{no}}^2\rho_{\mathrm{rec}}\,D_1(F,M).
\end{aligned}\tag{5.59}$$

In (c), we use the two properties given in (5.48) and (5.50). Due to (5.48), we get

$$\mathbb{E}\left[\eta_{\mathrm{no},i}^*(n)\eta_{\mathrm{no},j}(n)\right]=0,\tag{5.60}$$

while (5.50) gives us

$$\mathbb{E}\left[\eta_{\mathrm{no},i}^*(n)\sum_{m=-F}^{F}c(n+m)\,\mathrm{sinc}\left(\frac{m+t(n+m)}{M}\right)\eta_{\mathrm{imp},j}(n+m)\right]=0\tag{5.61}$$

and

$$\mathbb{E}\left[\eta_{\mathrm{no},j}(n)\sum_{m=-F}^{F}c(n+m)\,\mathrm{sinc}\left(\frac{m+t(n+m)}{M}\right)\eta_{\mathrm{imp},i}^*(n+m)\right]=0.\tag{5.62}$$

For (d), cf. (5.51).

The normalized version of the overall spatial correlation coefficient is given by

$$\frac{\mathbb{E}\left[\eta_i^*(n)\cdot\eta_j(n)\right]}{\mathbb{E}\left[\eta_i^*(n)\cdot\eta_i(n)\right]}=\frac{\rho_{\mathrm{rec}}\epsilon k D_1(F,M)}{1+\epsilon k D_1(F,M)}.\tag{5.63}$$

It depends on ϵ and k and since these parameters can change with the location of the sensor, we can say that uncertainty is introduced into the test statistic used for PU detection when employing receiver correlation.

Subsequently, we derive the unnormalized *overall time* correlation coefficient. It represents the amount of correlation between samples taken at a single sensor at different times ($q \neq 0$). It is given by

$$
\begin{aligned}
&\mathbb{E}\left[\eta_i^*(n) \cdot \eta_i(n-q)\right] \\
&= \mathbb{E}\left[\left(\eta_{\mathrm{no},i}(n) + \sum_{m=-F}^{F} c(n+m)\,\mathrm{sinc}\left(\frac{m+t(n+m)}{M}\right)\eta_{\mathrm{imp},i}(n+m)\right)^*\right. \\
&\qquad \left(\eta_{\mathrm{no},i}(n-q) + \sum_{m=-F}^{F} c(n-q+m)\right. \\
&\qquad\qquad \left.\left.\cdot\,\mathrm{sinc}\left(\frac{m+t(n-q+m)}{M}\right)\eta_{\mathrm{imp},i}(n-q+m)\right)\right] \\
&\overset{(e)}{=} \mathbb{E}\left[\left(\sum_{m=-F}^{F} c(n+m)\,\mathrm{sinc}\left(\frac{m+t(n+m)}{M}\right)\eta^*_{\mathrm{imp},i}(n+m)\right)\right. \\
&\qquad \left.\left(\sum_{m=-F}^{F} c(n-q+m)\,\mathrm{sinc}\left(\frac{m+t(n-q+m)}{M}\right)\eta_{\mathrm{imp},i}(n-q+m)\right)\right] \\
&= \mathbb{E}\left[\left(\sum_{m=-F}^{F} c(n+m)\,\mathrm{sinc}\left(\frac{m+t(n+m)}{M}\right)\eta^*_{\mathrm{imp},i}(n+m)\right)\right. \\
&\qquad \left.\left(\sum_{m=-F-q}^{F-q} c(n+m)\,\mathrm{sinc}\left(\frac{m+q+t(n+m)}{M}\right)\eta_{\mathrm{imp},i}(n+m)\right)\right] \\
&\overset{(f)}{=} \mathbb{E}\left[\sum_{m=-F}^{F-q} c^2(n+m)|\eta_{\mathrm{imp},i}(n+m)|^2\right. \\
&\qquad \left.\mathrm{sinc}\left(\frac{m+t(n+m)}{M}\right)\mathrm{sinc}\left(\frac{m+q+t(n+m)}{M}\right)\right] \\
&= \epsilon k \sigma_{\mathrm{no}}^2 \underbrace{\int_{-F-0.5}^{F-q+0.5} \mathrm{sinc}\left(\frac{t}{M}\right)\mathrm{sinc}\left(\frac{q+t}{M}\right) dt}_{:=D_2(F,M,q)} \\
&= \epsilon k \sigma_{\mathrm{no}}^2\, D_2(F,M,q).
\end{aligned}
\tag{5.64}
$$

For (e), cf. (5.49) and (5.50). For (f), cf. (5.49). Note, that $D_2(F,M,q) = D_1(F,M)$ for $q = 0$. However, we are only interested in the case $q \neq 0$. For $q \geq 2F$, $D_2 = 0$, since for these values of q, the time shift is bigger than the span of the cut receive filter. A closed-form expression for $D_2(F,M,q)$ does exist and can easily be determined using modern symbolic mathematical software. It is omitted here because it is quite lengthy and does not add to the discussion.

The normalized version of the overall time correlation coefficient is given by

$$\frac{\mathbb{E}\left[\eta_i^*(n)\cdot\eta_i(n-q)\right]}{\mathbb{E}\left[\eta_i^*(n)\cdot\eta_i(n)\right]}=\frac{\epsilon k D_2(F,M,q)}{1+\epsilon k D_1(F,M)}. \tag{5.65}$$

As the overall *spatial* correlation coefficient, the overall *time* correlation coefficient depends on ϵ and k, which means that employing time correlation for PU detection also makes us prone to uncertainty in the test statistic.

Lastly, the noise correlation coefficient for the case where receiver *and* time correlation is exploited is determined. Since the derivation is analogous to (5.64), it is skipped. The resulting unnormalized correlation coefficient is given by

$$\mathbb{E}\left[\eta_i^*(n)\cdot\eta_j(n-q)\right]=\epsilon k\sigma_{\mathrm{no}}^2\, D_2(F,M,q)\rho_{\mathrm{rec}}, \tag{5.66}$$

while its normalized version is obtained as

$$\frac{\mathbb{E}\left[\eta_i^*(n)\cdot\eta_j(n-q)\right]}{\mathbb{E}\left[\eta_i^*(n)\cdot\eta_i(n)\right]}=\frac{\rho_{\mathrm{rec}}\epsilon k D_2(F,M,q)}{1+\epsilon k D_1(F,M)}. \tag{5.67}$$

So far, we have shown that no matter if the employed detection method is based on the receiver correlation or the time correlation alone, or if it exploits both, receiver and time correlation, it is always prone to uncertainty in the noise correlation, i. e., the noise coloring, because the exact parameters of the location-dependent external impulsive noise cannot be known by the sensor. Since we have shown above, that uncertainty about the noise coloring can make a detector non-robust, we can now say, that the uncertainty about external impulsive noise can lead to an SNR-wall.

To round off the impulsive noise example, we now present lower bounds on the SNR-walls caused by impulsive noise using (5.29) as well as a set of reasonable parameters. The parameters are chosen such that they are in line with the measurement campaigns documented in [81, 78]. In the latter, two different measurement settings, one at quiet park and the other near a motorway road junction, are investigated. For the spatial correlation we choose a setup with two receivers ($p = 2$), which are close to each other, e. g., two antennas of the same device. We further choose a relatively low correlation value from the measurements dome in [81], i. e., $\rho_{\mathrm{rec}} = 0.2$. The full set of parameters are given in Table 5.2.

Table 5.2: Parameters

Parameter	Symbol	Value
Impulse occurrence probability	ϵ	$2\cdot10^{-4}$
Oversampling factor	M	4
Receive filter impulse response length	F	20
Number of receive antennas	p	2
Spatial correlation coefficient	ρ_{rec}	0.2

Given the above parameter set we can numerically determine the following function values

$$\begin{aligned} D_1(20,4) &= 3.9193, \\ D_2(20,4,1) &= 3.5441, \\ D_2(20,4,2) &= 2.5485, \\ D_2(20,4,3) &= 1.2637, \end{aligned} \tag{5.68}$$

as well as the overall noise power, which using (5.52) can be evaluated to

$$\mathbb{E}\left[\eta_i^*(n) \cdot \eta_i(n)\right] = \sigma_{\text{no}}^2(1 + 0.07839). \tag{5.69}$$

Note, that the correlation matrices given below are normalized by the overall noise power.

The first example is receiver correlation ($p = 2, Q = 0$). Using (5.59), the noise correlation matrix for the road junction, which represents the $\mathcal{H}_0$ case, can be obtained as

$$\mathbf{R}_{\boldsymbol{\eta},\text{rec}}^{\mathcal{H}_0} = \mathbb{E}\left[\begin{bmatrix} \eta_1(n) \\ \eta_2(n) \end{bmatrix} [\eta_1(n), \eta_2(n)]^*\right] = \begin{pmatrix} 1 & 0.01454 \\ 0.01454 & 1 \end{pmatrix}. \tag{5.70}$$

The corresponding value of the test statistic is given by $\Gamma_{\mathcal{H}_0}^{\text{asym}} = \alpha_{\max} = 1.0295$, leading to a lower bound on the SNR-wall according to (5.35) and assuming white Gaussian noise under $\mathcal{H}_1$ of

$$\text{SNR} \leq 1.47 \cdot 10^{-2} = -18.327 \text{ dB}. \tag{5.71}$$

The next example is time correlation ($p = 1, Q = 1$). Using (5.64), the noise correlation matrix for this case under $\mathcal{H}_0$ can be obtained as

$$\mathbf{R}_{\boldsymbol{\eta},\text{time}}^{\mathcal{H}_0} = \mathbb{E}\left[\begin{bmatrix} \eta_1(n) \\ \eta_1(n-1) \end{bmatrix} [\eta_1(n), \eta_1(n-1)]^*\right] = \begin{pmatrix} 1 & 0.06573 \\ 0.06573 & 1 \end{pmatrix}. \tag{5.72}$$

The corresponding value of the test statistic is given by $\Gamma_{\mathcal{H}_0}^{\text{asym}} = \alpha_{\max} = 1.1407$. From (5.40), we can obtain the maximum signal correlation value $\kappa_{\max} = 0.75$. Inserting $\alpha_{\max}$ and $\kappa_{\max}$ in (5.34) provides us with the lower bound on the SNR-wall given by

$$\text{SNR} \leq 9.6052 \cdot 10^{-2} = -10.175 \text{ dB}. \tag{5.73}$$

As we can see in the two above examples, introducing impulsive noise into a spectrum sensing scenario even using mild parameters leads to uncertainty regarding the noise coloring, causing bounds on the SNR-wall for the MME detector that are clearly above the demanded -22 dB (cf. Section 5.1.1).

5.1.9 Conclusion

In this section, we have proven the existence of an SNR-wall for the eigenvalue-based MME spectrum sensing algorithm. The SNR-wall is caused by uncertainty about the coloring of the receiver noise. A lower bound on the SNR-wall is derived and is complemented by time and receiver correlation examples. For these examples, we give concrete SNR values, below which the MME detector is non-robust and provide numerical results that support the analytical ones.

To support the claim that (man-made) impulsive noise in the sensors' surroundings can lead to uncertainty in the noise coloring strong enough to cause relevant SNR-walls, a model for impulsive noise is developed and the corresponding SNR-walls are evaluated. The results corroborate the claim.

One possible direction for future work is the derivation of tighter bounds on the SNR-wall. Also, it would be of great value if the results could be generalized to arbitrary eigenvalue-based spectrum sensing algorithms.

5.2 New Eigenvalue-Based Detectors

In this section we propose two new eigenvalue-based detection algorithms, the maximum-minus-minimum-eigenvalue (MMME) detector and the difference-of-means-of-eigenvalues (DME) detector. We give an intuition of their respective inner workings and discuss the choice of the second detector's parameter. Subsequently, we analyze their performance in comparison to other known eigenvalue-based detectors via numerical simulation.

5.2.1 System Model

The system model used in this work is a close adaptation of the model introduced in [45], which is beneficial regarding comparability of the results. For completeness, we shortly introduce it in the following.

Consider a system of P primary users, each transmitting a signal $s_j(t)$, with $j \in \{1, \ldots, P\}$. The secondary system receives a noise-contaminated superposition of these primary user signals after the effects of path loss, multipath fading and time dispersion. The noise mixed into the received signal is assumed to be zero-mean, i.i.d. and circularly-symmetric complex Gaussian with variance σ^2. The secondary system oversamples the symbols of the PU signal by the factor M, which here means that either there is one cognitive radio (CR) possessing M receive antennas or there are M collaborating CRs.

The samples acquired in the discrete time-domain during one symbol duration are given by

$$\mathbf{x}(n) = [x_1(n), x_2(n), \ldots, x_M(n)]^{\mathrm{T}} \tag{5.74}$$

for the n-th symbol.

We define the channel between the j-th PU and the respective receive antennas of the CR at the time of symbol n as

$$\mathbf{h}_j(n) = [h_{1j}(n), h_{2j}(n), \ldots, h_{Mj}(n)]^{\mathrm{T}}, \tag{5.75}$$

while the additive noise corrupting the reception of symbol n is denoted by

$$\boldsymbol{\eta}(n) = [\eta_1(n), \eta_2(n), \ldots, \eta_M(n)]^{\mathrm{T}}. \tag{5.76}$$

We consider sets of L consecutive outputs, which we express as

$$\begin{aligned}
\hat{\mathbf{x}}(n) =& [\mathbf{x}^{\mathrm{T}}(n), \mathbf{x}^{\mathrm{T}}(n-1), \ldots, \mathbf{x}^{\mathrm{T}}(n-L+1)]^{\mathrm{T}}, \\
\hat{\boldsymbol{\eta}}(n) =& [\boldsymbol{\eta}^{\mathrm{T}}(n), \boldsymbol{\eta}^{\mathrm{T}}(n-1), \ldots, \boldsymbol{\eta}^{\mathrm{T}}(n-L+1)]^{\mathrm{T}} \text{ and} \\
\hat{\mathbf{s}}(n) =& [s_1(n), s_1(n-1), \ldots, s_1(n-N_c-L+1), \ldots, \\
& s_P(n), s_P(n-1), \ldots, s_P(n-N_c-L+1)]^{\mathrm{T}},
\end{aligned} \tag{5.77}$$

where the n-th symbol of the j-th PU is denoted by $s_j(n)$ and N_c stands for the order of the channel, i. e., the length of the channel impulse response. L is a so-called smoothing factor.

Given the above definitions, we can write

$$\hat{\mathbf{x}}(n) = \mathbf{H}\hat{\mathbf{s}}(n) + \hat{\boldsymbol{\eta}}(n), \tag{5.78}$$

with $\mathbf{H} = [\mathbf{H}_1, \mathbf{H}_2, \ldots, \mathbf{H}_P]$, where

$$\mathbf{H}_j = \begin{bmatrix} \mathbf{h}_j(0) & \ldots & \ldots & \mathbf{h}_j(N_c) & & 0 \\ & \ddots & & & \ddots & \\ 0 & & \mathbf{h}_j(0) & \ldots & \ldots & \mathbf{h}_j(N_c) \end{bmatrix}. \tag{5.79}$$

The statistical covariance matrix of the received signal can now be written as

$$\begin{aligned}
\mathbf{R}_x &= \mathrm{E}(\hat{\mathbf{x}}(n)\hat{\mathbf{x}}^{\mathrm{H}}(n)) \\
&= \mathbf{H}\mathbf{R}_s\mathbf{H}^{\mathrm{H}} + \mathbf{R}_\eta \\
&= \mathbf{H}\mathbf{R}_s\mathbf{H}^{\mathrm{H}} + \sigma^2\mathbf{I},
\end{aligned} \tag{5.80}$$

with $\mathbf{R}_s = \mathrm{E}(\hat{\mathbf{s}}(n)\hat{\mathbf{s}}^{\mathrm{H}}(n))$ and $\mathbf{R}_\eta = \mathrm{E}(\hat{\boldsymbol{\eta}}(n)\hat{\boldsymbol{\eta}}^{\mathrm{H}}(n))$ being the statistical covariance matrices of the PU signals and the additive noise respectively and $\mathbf{I}$ denoting the identity matrix. Note that the last step in (5.80) is due to the noise being i.i.d.

Since we are not able to acquire an infinite amount of samples, we cannot come by the statistical covariance matrix and have to settle for its estimation, the $ML \times ML$ *sample* covariance matrix, which for our signal model is obtained as

$$\hat{\mathbf{R}}_x(N_s) = \frac{1}{N_s} \sum_{n=L-1}^{L-2+N_s} \hat{\mathbf{x}}(n)\hat{\mathbf{x}}^{\mathrm{H}}(n), \tag{5.81}$$

with N_s being the number of collected symbols.

5.2.2 Prior Work

Several spectrum sensing algorithms exploiting the properties of the covariance matrix can be found in the literature. Some of these are employed in a performance evaluation of the two new eigenvalue-based detectors in Section 5.2.4. They are shortly covered in the following. For each of the detectors, a test-statistic T is given such that for some threshold γ, the detector decides on the occupancy status of the spectral resource according to the following test:

$$T \underset{\mathcal{H}_0}{\overset{\mathcal{H}_1}{\gtrless}} \gamma, \tag{5.82}$$

i. e., if the test statistic is higher than the threshold γ, the detector decides that a PU signal is present. If it is lower, the detector decides that there is no PU signal present.

Maximum-Minimum-Eigenvalue (MME) Detector We denote the maximum - and minimum eigenvalue of $\hat{\mathbf{R}}_x(N_s)$ as $\hat{\lambda}_{\max}$ and $\hat{\lambda}_{\min}$ respectively. The MME detector as introduced in [16] is given by

$$T_{\mathrm{MME}} = \frac{\hat{\lambda}_{\max}}{\hat{\lambda}_{\min}} \underset{\mathcal{H}_0}{\overset{\mathcal{H}_1}{\gtrless}} \gamma_{\mathrm{MME}}. \tag{5.83}$$

Maximum-Eigenvalue-Trace (MET) Detector The MET detector has initially been introduced in [46]. It can be written as

$$T_{\mathrm{MET}} = \frac{\hat{\lambda}_{\max}}{\mathrm{Tr}(\hat{\mathbf{R}}_x(N_s))} \underset{\mathcal{H}_0}{\overset{\mathcal{H}_1}{\gtrless}} \gamma_{\mathrm{MET}}, \tag{5.84}$$

where $\mathrm{Tr}(\cdot)$ stands for the trace operation. Note, that for a square matrix $\mathbf{A}$,

$$\mathrm{Tr}(\mathbf{A}) = \sum_i a_{ii} = \sum_i \lambda_i(\mathbf{A}). \tag{5.85}$$

Cholesky-Factorization-Squares (CFS) Detector Considering the Cholesky factorization $\hat{\mathbf{R}}_x(N_s) = \hat{\mathbf{Q}}^{\mathrm{T}}\hat{\mathbf{Q}}$, the CFS detector introduced in [47] is defined as

$$T_{\mathrm{CFS}} = \frac{\sum_{1\le i\le j\le ML} \hat{q}_{ij}^2}{\sum_{1\le i\le ML} \hat{q}_{ii}^2} \underset{\mathcal{H}_0}{\overset{\mathcal{H}_1}{\gtrless}} \gamma_{\mathrm{CFS}}, \tag{5.86}$$

where $\hat{q}_{ij}$ is the (i,j)-th element of $\hat{\mathbf{Q}}$.

Quadratic Sphericity Test (QST) Given the ordered eigenvalues of $\hat{\mathbf{R}}_x(N_s)$ as

$$\hat{\lambda}_{\max} = \hat{\lambda}_1 \geq \hat{\lambda}_2 \geq \cdots \geq \hat{\lambda}_{ML} = \hat{\lambda}_{\min}, \tag{5.87}$$

the QST as described in [48] is given as

$$T_{\mathrm{QST}} = \frac{\sqrt{\sum_{1\leq i\leq ML} \hat{\lambda}_i^2}}{\sum_{1\leq i\leq ML} \hat{\lambda}_i} \underset{\mathcal{H}_0}{\overset{\mathcal{H}_1}{\gtrless}} \gamma_{\mathrm{QST}}. \tag{5.88}$$

5.2.3 Introduction of MMME and DME

In this section we propose two new eigenvalue-based test statistics for spectrum sensing.

Maximum-Minus-Minimum-Eigenvalue (MMME) Detector Consider the ordered eigenvalues $\lambda_1, \ldots, \lambda_{ML}$ of the *statistical* covariance matrix $\mathbf{R}_x$ as well as the ordered eigenvalues $\rho_1, \ldots, \rho_{ML}$ of $\mathbf{H}\mathbf{R}_s\mathbf{H}^{\mathrm{H}}$ analogous to (5.87). The MME detector (5.83) is based on the idea that since $\lambda_n = \rho_n + \sigma^2$, it holds that $\frac{\lambda_1}{\lambda_{ML}} = 1$ for $\mathcal{H}_0$ (if no PU signal is present, $\rho_i = 0|_{i=1}^{ML}$) and $\frac{\lambda_1}{\lambda_{ML}} > 1$ for $\mathcal{H}_1$.

As the authors of [45] find, choosing L large enough leads to $\rho_{ML} = 0$ even if a PU signal is present. Taking this into account and including the estimation noise caused by the *finite* amount of samples gathered, we can express the detector's test statistic as

$$\begin{aligned} T_{\mathrm{MME},\mathcal{H}_1} &= \frac{\hat{\lambda}_1}{\hat{\lambda}_{ML}} = \frac{\rho_1 + \sigma^2 + \epsilon_1}{\sigma^2 + \epsilon_2} = \frac{\sigma^2 + \epsilon_1}{\sigma^2 + \epsilon_2} + \frac{\rho_1}{\sigma^2 + \epsilon_2}, \\ T_{\mathrm{MME},\mathcal{H}_0} &= \frac{\hat{\lambda}_1}{\hat{\lambda}_{ML}} = \frac{\sigma^2 + \epsilon_3}{\sigma^2 + \epsilon_4}, \end{aligned} \tag{5.89}$$

where $-\epsilon \leq \epsilon_i \leq \epsilon|_{i\in\{1,2,3,4\}}$ models the perturbation of the eigenvalues. The estimation noise vanishes for high N_s, i. e., $\lim\limits_{N_s\to\infty} \epsilon = 0$. Thus, we can see that on top of the estimation noise, the MME detector is affected by the SNR. The lower the SNR, the lower ρ_1/σ^2.

To tackle this disadvantage, we propose the MMME detector as a modification of the MME detector. Its test statistic is given as

$$T_{\mathrm{MMME}} = \ln\left(\frac{e^{\hat{\lambda}_{\max}}}{e^{\hat{\lambda}_{\min}}}\right) = \hat{\lambda}_{\max} - \hat{\lambda}_{\min} \underset{\mathcal{H}_0}{\overset{\mathcal{H}_1}{\gtrless}} \gamma_{\mathrm{MMME}} \tag{5.90}$$

Note that the $\ln(\cdot)$ has no influence on the detector's performance. Investigating this detector, we find that

$$\begin{aligned} T_{\mathrm{MMME},\mathcal{H}_1} &= \ln\left(\frac{e^{\hat{\lambda}_1}}{e^{\hat{\lambda}_{ML}}}\right) = \ln\left(\frac{e^{\rho_1+\sigma^2+\epsilon_1}}{e^{\sigma^2+\epsilon_2}}\right) = \rho_1 + \epsilon_1 - \epsilon_2, \\ T_{\mathrm{MMME},\mathcal{H}_0} &= \ln\left(\frac{e^{\hat{\lambda}_1}}{e^{\hat{\lambda}_{ML}}}\right) = \ln\left(\frac{e^{\sigma^2+\epsilon_3}}{e^{\sigma^2+\epsilon_4}}\right) = \epsilon_3 - \epsilon_4, \end{aligned} \tag{5.91}$$

which shows that asymptotically ($\epsilon_i \to 0|_{i\in\{1,2,3,4\}}$), the detector is independent of the SNR.

Difference-of-Means-of-Eigenvalues (DME) Detector A typical strategy to diminish noise is to average over multiple values. Neither the MME -, nor the MMME detector exploits this. Both only make use of two of the ML available eigenvalues. Building on the idea of the MMME detector, we implement this concept by proposing the DME detector as

$$T_{\mathrm{DME}}(N_1) = \frac{1}{N_1}\sum_{i=1}^{N_1}\hat{\lambda}_i - \frac{1}{ML-N_1}\sum_{i=N_1+1}^{ML}\hat{\lambda}_i \underset{\mathcal{H}_0}{\overset{\mathcal{H}_1}{\gtrless}} \gamma_{\mathrm{DME}}. \tag{5.92}$$

The choice of N_1 comes down to a tradeoff between multiple objectives. In order to achieve a good detection performance, it would generally be favorable to minimize the overlap between the PDF of $T_{\mathrm{DME},\mathcal{H}_0}$ and the PDF of $T_{\mathrm{DME},\mathcal{H}_1}$. In fact, if the overlap of the two PDFs was zero and a way of setting the correct decision threshold was known, perfect detection could be achieved. When setting N_1, we are thus interested in minimizing the mean of $T_{\mathrm{DME},\mathcal{H}_0}$ as well as maximizing the mean of $T_{\mathrm{DME},\mathcal{H}_1}$. We should also try to minimize the respective variances of $T_{\mathrm{DME},\mathcal{H}_0}$ and $T_{\mathrm{DME},\mathcal{H}_1}$. An empirical evaluation of these objectives is given in Section 5.2.4.

5.2.4 Numerical Evaluation

For the simulation, we consider a scenario exhibiting the parameters given in Table 5.3. For each of the Monte Carlo realizations, a random BPSK signal for each PU, a random Gaussian distributed channel and random noise is generated.

In Figure 5.8, the mean of T_{DME} over the Monte Carlo realizations is plotted for different SNRs in the case where a PU signal is present ($\mathcal{H}_1$) as well as in the case where no PU signal is present ($\mathcal{H}_0$). Recall that while making the choice of N_1 we try to minimize T_{DME} in the case of $\mathcal{H}_0$, but try to maximize it in the case of $\mathcal{H}_1$.

What we can see in Figure 5.8 is that the lower the SNR, the closer the $\mathcal{H}_1$-curve comes to the $\mathcal{H}_0$-curve. We also see, that the lower the SNR, the more closely the $\mathcal{H}_1$-curve resembles the $\mathcal{H}_0$-curve in its shape. These effects are brought along by the decreasing influence of the signal eigenvalues in the test statistic caused by a decreasing SNR. The

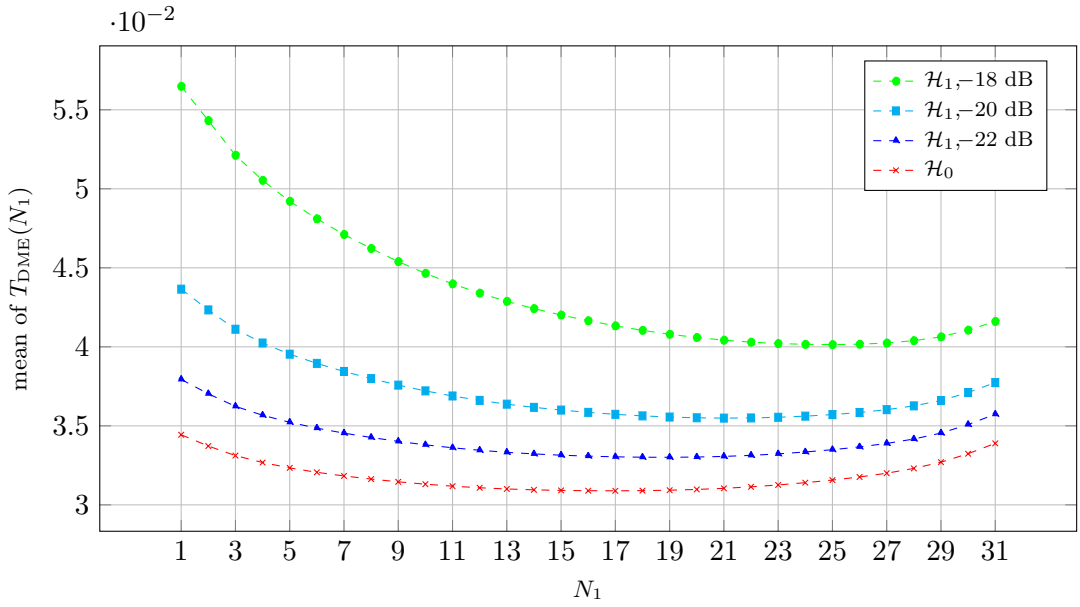

Figure 5.8: Mean of $T_{\mathrm{DME}}(N_1)$ over 10^4 Monte Carlo realizations for different SNRs in the case of a present PU signal ($\mathcal{H}_1$) as well as in the case of noise only ($\mathcal{H}_0$).

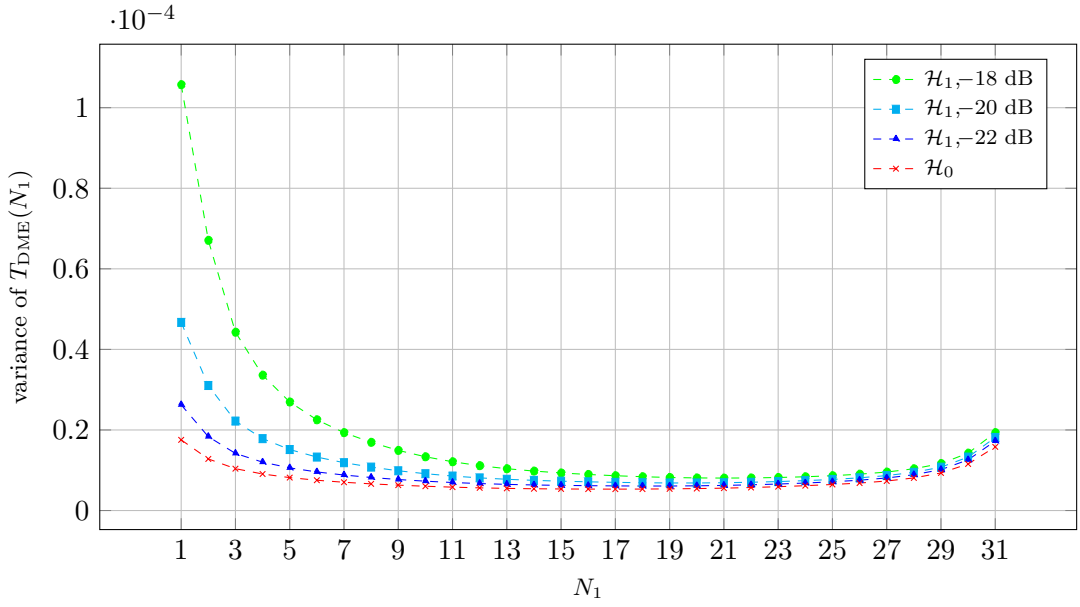

Figure 5.9: Variance of $T_{\mathrm{DME}}(N_1)$ over 10^4 Monte Carlo realizations for different SNRs in the case of a present PU signal ($\mathcal{H}_1$) as well as in the case of noise only ($\mathcal{H}_0$).

Table 5.3: Scenario parameters

Parameter	Symbol	Value(s)
Number of PUs	P	2
Number of receive antennas / collab. CRs	M	4
Channel order	N_c	9
Smoothing factor	L	8
Number of symbols	N_s	10^5
Number of Monte Carlo realizations		10^4

figure gives us a clear picture of the forces, which have to be traded off against each other. In order to minimize $T_{\mathrm{DME},\mathcal{H}_0}$, N_1 would have to be chosen to be roughly $\frac{ML}{2}$. However, even for low SNRs N_1 has to be set to 1 to maximize $T_{\mathrm{DME},\mathcal{H}_1}$.

As we can see in Figure 5.9, minimizing the variance of $T_{\mathrm{DME},\mathcal{H}_0}$ can again be achieved by choosing $N_1 \approx \frac{ML}{2}$. Regarding the minimization of the variance of $T_{\mathrm{DME},\mathcal{H}_1}$, the higher the SNR, the higher N_1 has to be chosen. For very low SNRs it is approximately the same as for $T_{\mathrm{DME},\mathcal{H}_0}$.

The right choice of N_1 has a large effect on the performance of the DME detector. Thus, it would be advantageous to have an analytic way of setting it optimally.

In Figure 5.10, the performance of the two new detectors is compared against other detectors from the literature. For the scenario used in the simulation, the optimal choice of N_1 empirically turned out to be 8. The figure shows the receiver operating characteristic (ROC) of the detectors at an SNR of -20 dB. We observe, that the DME detector shows the highest probability of detection (P_{d}) for all probabilities of false alarm (P_{fa}). What can also be seen, is that although the MMME detector is weaker than the top contenders, it clearly outperforms the MME detector.

5.2.5 Conclusion

In this section, we have introduced two new eigenvalue-based detectors for spectrum sensing, the maximum-minus-minimum-eigenvalue (MMME) detector and the difference-of-means-of-eigenvalues (DME) detector. We have discussed the respective ideas behind them and have investigated the tradeoff leading to an optimal parameter choice for the DME test statistic. Finally, we have numerically evaluated the performance of the two new detectors in comparison to other detectors. Based on the MME detector, the MMME detector improves upon the performance of its origin, while the DME detector shows the best performance of all considered detectors.

Since the choice of the DME detector's parameter heavily influences its performance, an interesting research direction would be to find an analytic way of obtaining the optimal parameter. It would also be of great value to have analytic expressions for the new

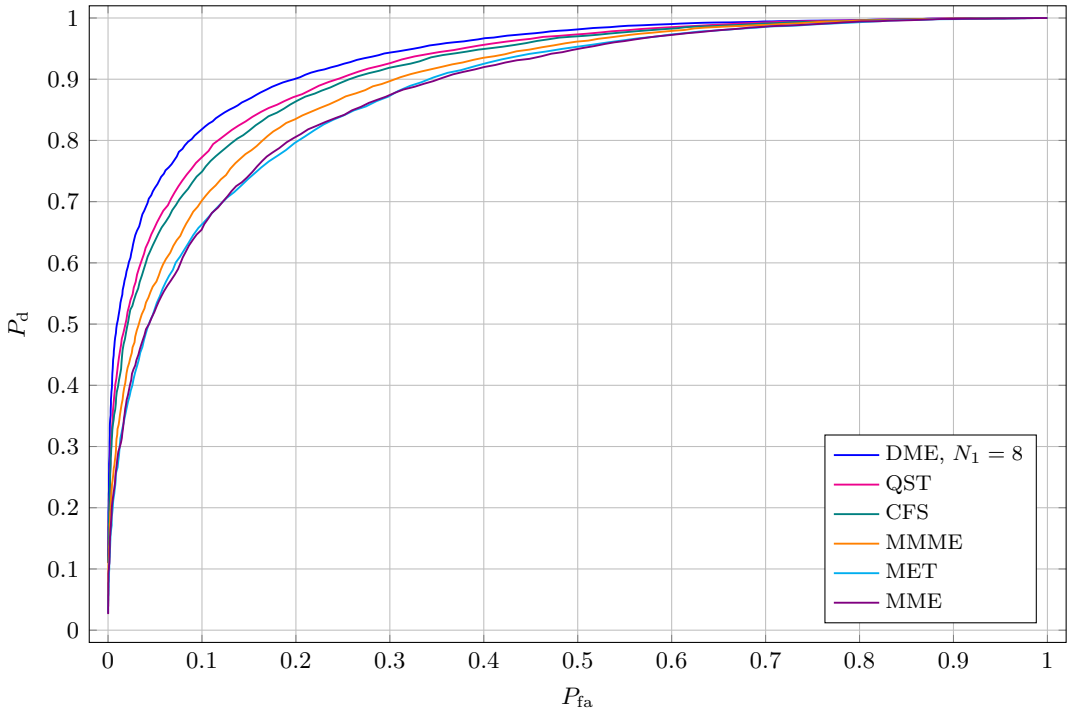

Figure 5.10: Receiver operating characteristics of DME (5.92) with $N_1 = 8$, QST (5.88), CFS (5.86), MMME (5.90), MET (5.84) and MME (5.83) at an SNR of -20 dB.

detectors' PDFs under $\mathcal{H}_0$. For MMME, this has been accomplished in [22], while for DME this is still an open problem.

6 Energy Detection

The energy detector, also called radiometer is one of the earliest and most basic spectrum sensing algorithms. Its analysis dates back to at least 1967, when Harry Urkowitz published the landmark paper [36]. The detector consists of measuring the energy contained in a received signal and comparing it to a fixed threshold. Depending on the receiver noise characteristics, the $\mathcal{H}_0$ PDF, which is used for setting the threshold according to a desired false alarm rate, is assumed to follow a chi-squared or a Gaussian distribution. The detector's biggest drawback is its performance degradation under noise uncertainty, as analyzed in [29].

In this chapter, we consider the problem of sensing a sparsely occupied wideband spectrum utilizing a set of spatially distributed sensing nodes as well as a fusion center. Exchange of measurement data between the sensing nodes and the fusion center takes up parts of the scarce radio spectrum and thus, methods for reducing the minimum amount of measurements still ensuring a reliable reconstruction of the spectrum at the fusion center are needed. To this end we propose two approaches in the form of convex optimization problems to tackle the problem. The first approach applies classic compressed sensing, while the second one improves the optimization problem such that the measurements from all sensors, which have been acquired in a distributed manner, can be taken into consideration in a single spectrum recovery operation. This makes it possible to exploit the inherent diversity gain stemming from the spatial distribution of the sensors.

Parts of the present chapter have been published in [18].

6.1 Motivation and Prior Work

As pointed out in Section 3.3, reliable spectrum sensing can only be accomplished in a distributed manner due to the effects of path loss and fading as experienced in all wireless communication settings. Distributed spectrum sensing makes it necessary to share either local sensor decisions or measurement data, which in turn claims some of the spectral resources that are to be used by actual wireless services. In this chapter we consider the case of measurement sharing. Our goal is to minimize the number of measurements, which have to be shared for reliable spectrum sensing.

Due to the underutilization of the wireless spectrum [3, 4], a wideband signal acquired for the purpose of spectrum sensing can be assumed to be only sparsely occupied in the

frequency domain, which can be taken advantage of in the process of signal acquisition by the means of CS. In the present application, the advent of CS means that a sparse frequency spectrum can be acquired by taking an amount of time-domain samples drastically smaller than necessary when conducting traditional Nyquist-rate sampling and recovering the signal of interest from these.

A rich literature exists in the field of spectrum sensing via compressed sensing. One example of this is the paper by Tian [82] in which the author proposes a system of spatially distributed CRs that undersample the spectrum in the time domain and exchange measurement data in a one-hop fashion to benefit from the spatial diversity gain which helps increase the reliability of the system and fight channel fading effects. Making use of the distributed average consensus algorithm presented in [83], each CR is in possession of the collective view of the spectrum after a number of iterations. In [17] the authors have proposed a spectrum sensing algorithm based on a method called matrix completion (MC) [84, 85], a data acquisition scheme similar to CS that exploits the low-rank property of matrices to recover them from incomplete data. Their system assumes the spectrum occupation to change only slowly in time and takes advantage of this by introducing a sliding window algorithm that takes measurements of previous sensing cycles into account during the recovery of the current signal.

In this chapter, two approaches for recovering the spectrum from an incomplete set of measurements are introduced. The first one is similar to the one introduced in [82] and serves as a benchmark for the second approach. It employs classic compressive sampling and subsequent signal fusion. In contrast to [82], our first approach only considers a single transmitter emitting a signal instead of several ones. In order to reduce the necessary amount of known samples even further while still guaranteeing a reliable spectrum recovery, we propose a novel approach. It consists of an optimization problem for recovering the spectrum in a way that makes it possible to take into account the measurements of all collaborating CRs in a single recovery operation. This unleashes the diversity gain inherent in the samples supplied by the spatially distributed sensing nodes and thus allows us to make optimal use of the available knowledge. Another substantial difference to [82] is, that we evaluate the case where the channel coefficients are known to the system sensing the spectrum. While the authors of [82] also mention this case, they focus on the scenario where the collaborating CRs are not in possession of any channel knowledge.

6.2 Signal Model

A wide frequency-band containing n_{sc} non-overlapping sub-channels is considered. The sub-channels occupy equal parts of the band. These parts are narrow and thus, the frequency-selective fading can be considered to be flat for each of them.

The licensee of the spectrum, transmits a frequency-domain signal $\mathbf{f} \in \mathbb{C}^{n_{\mathrm{sc}}}$ containing one coefficient per sub-channel. The signal is k-sparse, meaning that only k of its n_{sc}

entries are non-zero. The sparsity represents the underutilization of the spectrum. While the partitioning of the band is fixed and known, the amplitudes and phases on the subchannels change over time.

A set of n_{cr} geographically distributed cognitive radios is deployed to sense the signal so that a fusion center (FC) can reconstruct the signal $\mathbf{f}$, as observed at the transmitter, as accurately as possible from the CRs' measurements.

The signal sensed by CR i for $i = 1, ..., n_{\text{cr}}$ is given by

$$\tilde{\mathbf{f}}_i = \mathbf{H}_i \mathbf{f} + \mathbf{n}_i, \tag{6.1}$$

where $\mathbf{H}_i \in \mathbb{C}^{n_{\text{sc}} \times n_{\text{sc}}}$ is a diagonal channel matrix, the entries of which are distributed according to a Rayleigh distribution. The entry $[\mathbf{H}_i]_{jj}$ represents the signal attenuation that CR i experiences on channel j. The entries of the noise vector $\mathbf{n}_i$ are independent and identically distributed (i.i.d.) Gaussian random variables with mean zero and variance σ^2. The CRs are assumed to have knowledge of their respective channel matrix $\mathbf{H}_i$.

In order to keep the amount of sampled data which has to be sent to the FC as small as possible, the CRs employ CS, meaning that they undersample the spectrum in the time domain, i. e., CR i takes $m \ll n_{\text{sc}}$ randomly distributed samples of the time-domain signal vector

$$\tilde{\mathbf{t}}_i = \mathbf{F}_{n_{\text{sc}}}^{-1} \tilde{\mathbf{f}}_i, \tag{6.2}$$

where $\mathbf{F}_{n_{\text{sc}}}^{-1}$ stands for the IDFT matrix of size $n_{\text{sc}} \times n_{\text{sc}}$. Each CR transmits m time-domain samples to the FC. These are selected in the following way:

$$\hat{\mathbf{t}}_i = \mathbf{M}_i \tilde{\mathbf{t}}_i, \tag{6.3}$$

where $\mathbf{M}_i \in \{0, 1\}^{m \times n_{\text{sc}}}$ denotes the selection matrix consisting of m randomly chosen rows of the $n_{\text{sc}} \times n_{\text{sc}}$ identity matrix. Note, that all matrices $\mathbf{M}_i$ are known to the FC.

The setup is illustrated in Figure 6.1.

6.3 Optimization Problems

To accomplish the collective objective, i. e., reconstruct $\mathbf{f}$ from the measurements, we propose two approaches, both of which employ ℓ_1-minimization.

6.3.1 First Approach: Separate Reconstruction and Fusion

In the first approach, the basic compressive sampling problem is solved for the measurements of each CR separately. This approach is similar to the one proposed in [82]. In

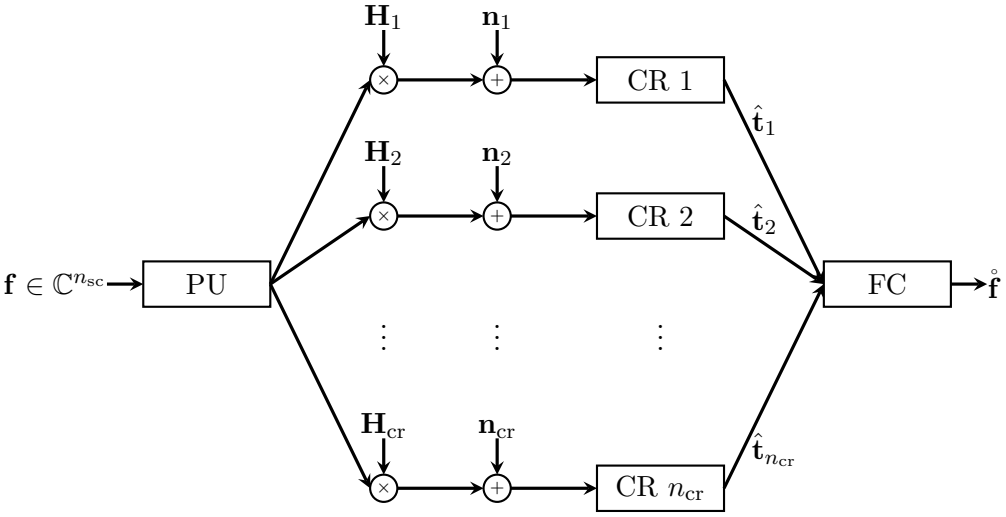

Figure 6.1: System model.

the present chapter, it serves as a benchmark against which our novel approach is compared. For the data received from CR i, the FC solves the following convex optimization problem:

$$\begin{aligned} \underset{\mathring{\mathbf{f}}_i}{\text{minimize}} \quad & \left\| \mathring{\mathbf{f}}_i \right\|_1 \\ \text{subject to} \quad & \left\| \mathbf{M}_i \mathbf{F}_{n_{\mathrm{sc}}}^{-1} \mathbf{H}_i \mathring{\mathbf{f}}_i - \hat{\mathbf{t}}_i \right\|_2 \leq \epsilon_{\mathrm{s}}, \end{aligned} \tag{6.4}$$

where $\|\cdot\|_1$ is the ℓ_1-norm defined by

$$\|\mathbf{z}\|_1 = \sum_{j=1}^{n_{\mathrm{z}}} |z_j| \tag{6.5}$$

given some vector $\mathbf{z} \in \mathbb{C}^{n_{\mathrm{z}}}$ and $\|\cdot\|_2$ stands for the ℓ_2-norm, i. e.,

$$\|\mathbf{z}\|_2 = \sum_{j=1}^{n_{\mathrm{z}}} |z_j|^2. \tag{6.6}$$

The constant ϵ_{s} bounds the amount of expected noise energy in the signal.

The reconstructed spectra $\mathring{\mathbf{f}}_i^{\star}$ are subsequently fused by the means of equal gain combining:

$$\mathring{\mathbf{f}} = \frac{1}{n_{\mathrm{cr}}} \sum_{i=1}^{n_{\mathrm{cr}}} \mathring{\mathbf{f}}_i^{\star}. \tag{6.7}$$

Here, the star $\star$ marks the solution to an optimization problem, i. e., $\mathring{\mathbf{f}}_i^{\star}$ is the solution to (6.4). The vector $\mathring{\mathbf{f}}$ is the reconstruction of the frequency-domain signal as observed at the transmitter, i. e., in a scenario with $\mathbf{n}_i = \mathbf{0}$ for all i, a perfect reconstruction would yield $\mathring{\mathbf{f}} = \mathbf{f}$.

6.3.2 Second Approach: Combined Reconstruction

In the new approach, all available measurements are taken into account in a single combined reconstruction of the spectrum in order to make better use of the diversity gain inherent in the available data due to the spatial distribution of the sensors. Instead of solving the optimization problem separately for each CR's data, the optimization problem is modified so that the ℓ_1-minimization directly recovers the primary user's signal from all measurements the FC has received.

In order to do so, we first define the matrix of time domain samples given by

$$\tilde{\mathbf{T}} = [\tilde{\mathbf{t}}_1, ..., \tilde{\mathbf{t}}_{n_{\mathrm{cr}}}], \tag{6.8}$$

in which each column represents the time-domain signal observed at one of the CRs. Furthermore, we define the sampling set Ω. It has the cardinality m and is comprised of the indices of the entries of $\tilde{\mathbf{T}}$ that are to be sampled by the respective CRs. We define the sampling operator $\mathcal{P}_\Omega : \mathbb{C}^{n_{\mathrm{sc}} \times n_{\mathrm{cr}}} \to \mathbb{C}^{n_{\mathrm{sc}} \times n_{\mathrm{cr}}}$ as follows. Given a matrix $\mathbf{X}$,

$$[\mathcal{P}_\Omega(\mathbf{X})]_{ij} = \begin{cases} [\mathbf{X}]_{ij} & \text{if } (i,j) \in \Omega, \\ 0 & \text{otherwise.} \end{cases} \tag{6.9}$$

Making use of the previous definitions, the measurements available at the FC can be written as

$$\hat{\mathbf{T}} = \mathcal{P}_\Omega(\tilde{\mathbf{T}}). \tag{6.10}$$

Finally, we define the concatenated channel matrix as

$$\bar{\mathbf{H}} = [\mathbf{H}_1, ..., \mathbf{H}_{n_{\mathrm{cr}}}]. \tag{6.11}$$

The resulting convex optimization problem which has to be solved by the FC is given by

$$\begin{aligned} \underset{\mathring{\mathbf{f}}}{\text{minimize}} \quad & \left\| \mathring{\mathbf{f}} \right\|_1 \\ \text{subject to} \quad & \left\| \mathcal{P}_\Omega(\mathbf{F}_{n_{\mathrm{sc}}}^{-1} \bar{\mathbf{H}} (\mathbf{I}_{n_{\mathrm{cr}}} \otimes \mathring{\mathbf{f}})) - \hat{\mathbf{T}} \right\|_2 \leq \epsilon_{\mathrm{c}}, \end{aligned} \tag{6.12}$$

where $\mathbf{I}_{n_{\mathrm{cr}}}$ is the identity matrix of size n_{cr} and $\otimes$ denotes the Kronecker product. Note that since this optimization problem takes into account the measurements of all CRs, no fusion is necessary and $\mathring{\mathbf{f}}$ is the final reconstruction of the primary user's signal.

Since both optimization problems are convex, the solution can be computed efficiently. Note that, for a single cognitive radio, the optimization problems of the two approaches are equivalent.

6.4 Numerical Evaluation

In this section, the two approaches are compared via simulation, employing the parameters given in Table 6.1. For the purpose of solving the convex optimization problems, the `CVX` software package [86] has been used.

The non-zero entries of $\mathbf{f}$ are generated randomly according to a zero-mean circularly-symmetric complex Gaussian distribution. The channel coefficients are distributed according to a Rayleigh distribution with standard deviation $\gamma = 1$ and the noise vectors contain entries which are distributed according to a circularly-symmetric complex standard Gaussian distribution. The variance of the signal values is defined by the respective SNR, where the SNR is defined as the signal energy of the wideband signal over the entire spectrum divided by the overall noise energy (again over the entire spectrum).

Table 6.1: Scenario parameters

Parameter	Symbol	Value(s)
Number of frequency subchannels	n_{sc}	100
Number of occupied subchannels	k	10
Number of CRs	n_{cr}	$\{1, 3, 5, 7, 9\}$
Signal to noise ratio (SNR)	SNR	$\{0, 5, 10, ..., 40\}$ dB
Undersampling factor	$\frac{m}{n_{\text{sc}}}$	$\{3, 5, 7, 10, 20, 30, 40, 50\}\%$
Number of Monte Carlo instances		1000

We define the normalized root mean squared error (NRMSE) as

$$e_{\text{NRMSE}} = \frac{\sqrt{\frac{\left\|\mathbf{f}-\hat{\mathbf{f}}\right\|_2^2}{n_{\text{sc}}}}}{\sqrt{\frac{\|\mathbf{f}\|_2^2}{n_{\text{sc}}}}} = \frac{\left\|\mathbf{f}-\mathring{\mathbf{f}}\right\|_2}{\|\mathbf{f}\|_2}. \tag{6.13}$$

The NRMSE caused by undersampling the signal with 20 and 50 of the 100 Nyquist-rate samples respectively is depicted in Figure 6.2 and Figure 6.3.

The two figures show the resulting NRMSE for various numbers of collaborating CRs with respect to the SNR. Note that the two approaches are equivalent for the case where only a single cognitive radio is utilized and that therefore the corresponding curves in the graph completely overlap.

As expected, decreasing the amount of noise in the system yields a better reconstruction result in all situations since the reconstruction is compared to the original noiseless primary user signal. However, in the heavily undersampled case, i. e., 20 samples per signal recovery, the NRMSE resulting from applying the separate reconstruction and subsequent fusion decreases much slower for decreasing noise than the NRMSE of the second approach. The more samples are available, the smaller the difference in performance between the two methods.

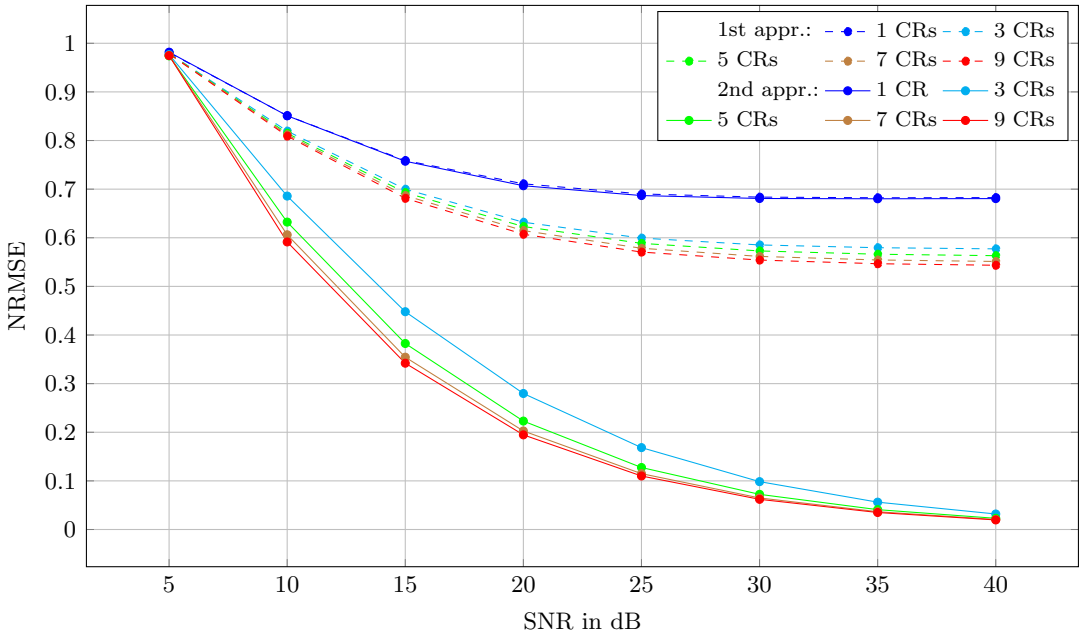

Figure 6.2: NRMSE of reconstructing the primary user's signal utilizing various numbers of collaborating CRs taking 20 ($= \frac{n_{\text{sc}}}{5}$) samples each.

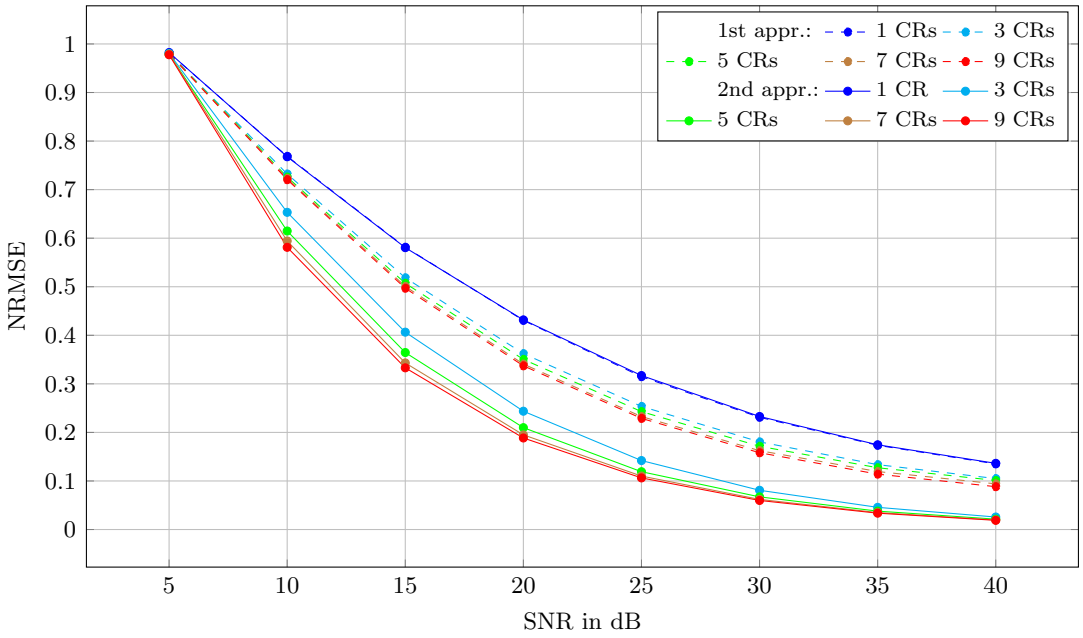

Figure 6.3: NRMSE of reconstructing the primary user's signal utilizing various numbers of collaborating CRs taking 50 ($= \frac{n_{\text{sc}}}{2}$) samples each.

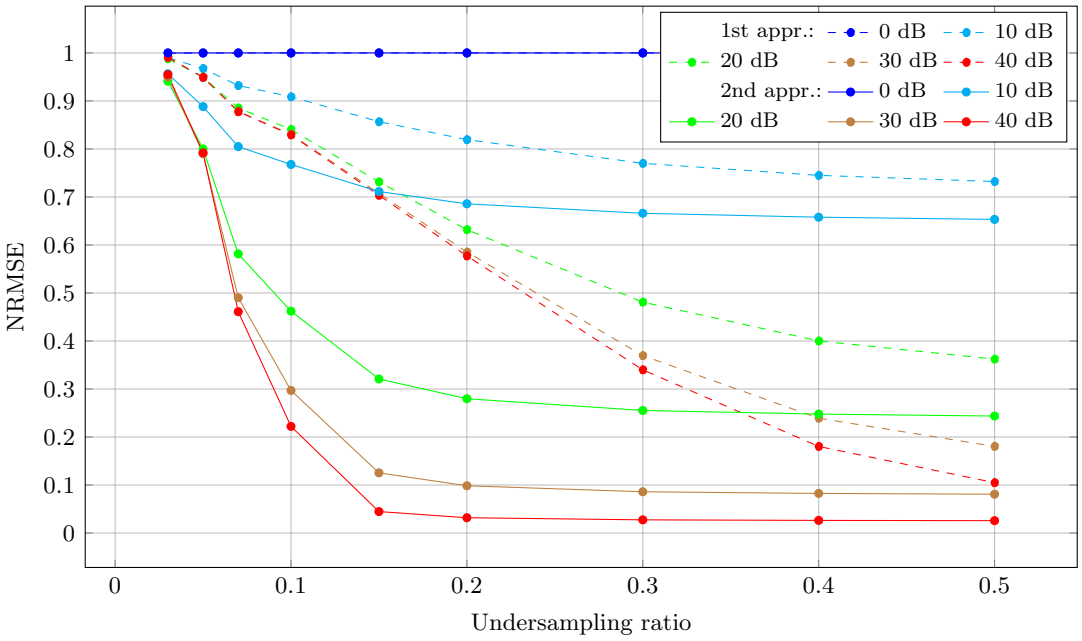

Figure 6.4: NRMSE of reconstructing the primary user's signal for various SNRs utilizing 3 collaborating CRs.

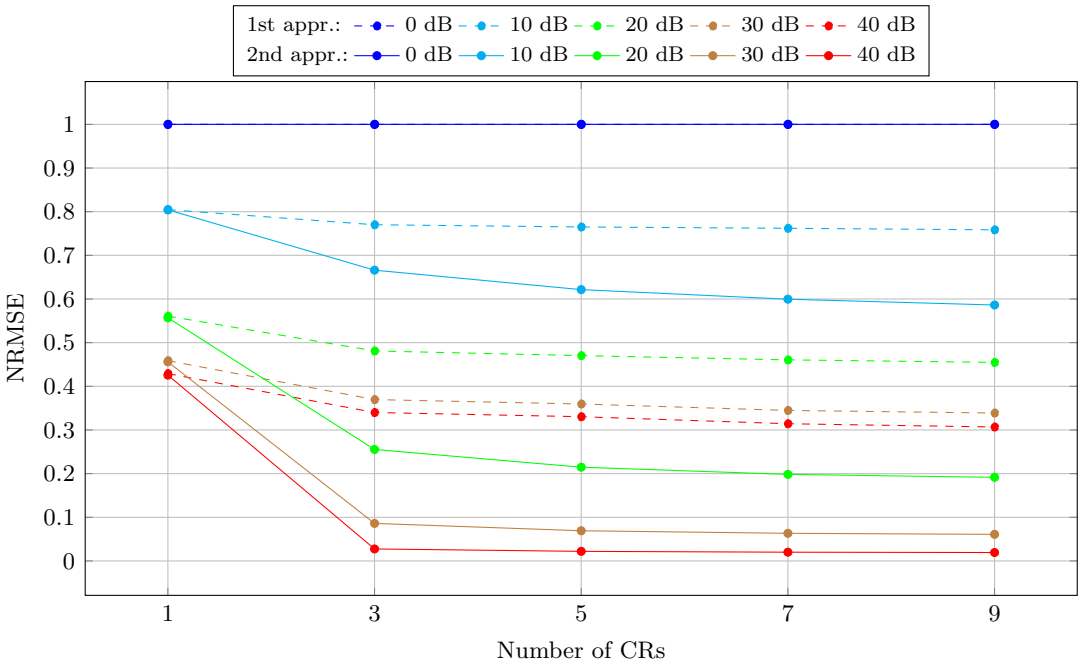

Figure 6.5: NRMSE of reconstructing the primary user's signal for various SNRs taking 30 ($= 0.3\, n_{\mathrm{sc}}$) samples per CR.

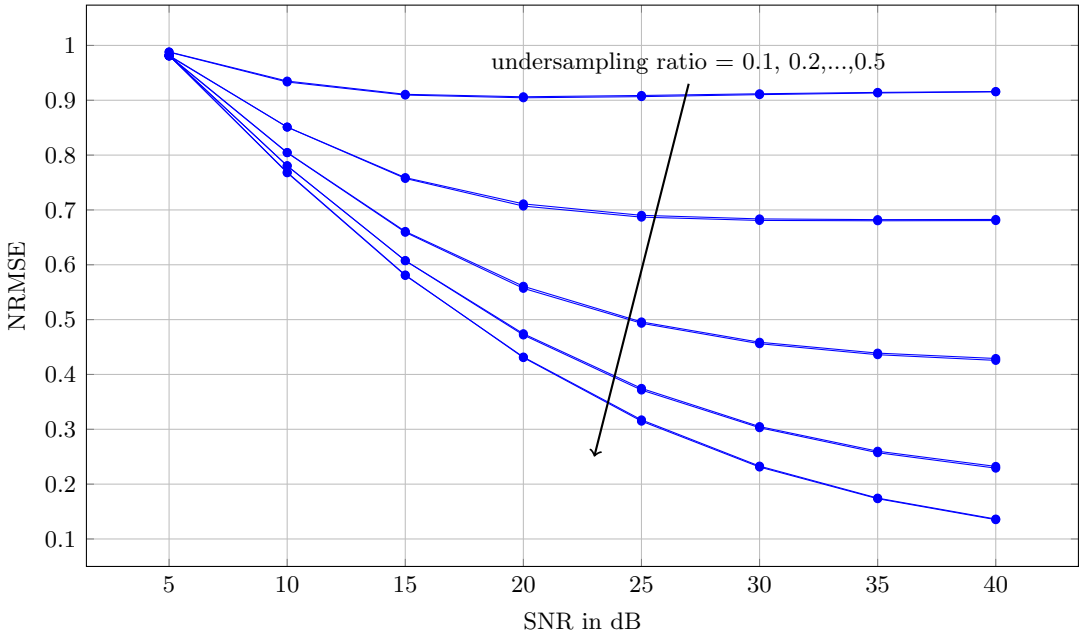

Figure 6.6: NRMSE of reconstructing the primary user's signal from the measurements of a single CR utilizing various numbers of samples.

In Figure 6.4 we observe how the error-behavior of recovering the primary user's signal depends on the number of samples that are taken into consideration per CR. For this we use a fixed number of cognitive radios and different signal to noise ratios. We can see that the combined recovery approach makes much better use of the samples available at the FC.

Figure 6.5 shows how the two approaches perform when the number of collaborating CRs changes while the number of samples per CR is fixed at 30. Again, since the two methods are equal for a single cognitive radio, their error performance is the same in this case. However, when the number of collaborating CRs is increased, the method employing the combined reconstruction constantly outperforms the method doing the reconstruction separately.

Another interesting effect is found in the observations depicted in Figure 6.6. The figure shows the error performance of the reconstruction from measurement data of a single CR in different SNR regions. As one would obviously expect, increasing the number of samples available for the signal recovery decreases the RMSE. However, an interesting observation directly visible in the figure is, that in terms of decreasing the RMSE, the more samples we take into consideration the less gain we experience from every additional sample. Although the number of samples used for the signal recovery increases by the same amount from line to line, the distance between two adjacent lines becomes smaller as the number of samples goes up.

In reverse this means, that the first samples are the most *valuable* ones.

The reconstruction of the spectral coefficients using the combined knowledge of all CRs yields a high diversity gain in contrast to the separate reconstruction and subsequent fusion. The reason for this is that in the separate reconstruction, the diversity gain is only exploited at the fusion stage, while in the combined reconstruction the whole recovery process gains from all available information.

6.5 Conclusion

In this chapter we have proposed two approaches for the purpose of reducing signaling overhead between a set of spatially distributed cognitive radios and a fusion center which collaboratively try to estimate a signal transmitted by a primary user for subsequent use in a detection algorithm. Both recovery algorithms have been formulated as convex optimization problems in order to make the signal reconstruction from a small subset of time-domain samples tractable, where the first approach applies actual compressive sampling and the second approach consists of a modified optimization problem designed to reduce the number of necessary samples even further. Both approaches have been shown to be viable through a numerical simulation, the results of which have been discussed for their different dimensions. Finally, the outcomes are explained.

7 Spectrum Sensing Simulation Framework

In this chapter we present the software framework that is used for most numerical evaluations presented in this thesis. In order to ensure flexibility and code reusability we chose an object-oriented architecture. As a programming environment MATLAB was selected. The reason for this is twofold: first, the syntax of the MATLAB programming language provides a concise way of implementing math-heavy applications, especially ones that contain a lot of linear algebra; second, MATLAB has an extensive ecosystem, including the Communications System Toolbox, which simplifies standard tasks in the development of spectrum sensing simulations.

The initial idea for the framework was to be modular such that monolithic code bases are avoided, since they are hard to extend and maintain. The advantages gained by the choice of a modular approach become apparent in the course of the chapter. The framework consists of different types of building blocks, which we call components. These components can be configured with different parameters and subsequently be put together to build a complete spectrum sensing simulation. An overview of the different software entities involved is given in Figure 7.1. Detailed descriptions of the purpose and features of those entities is provided in the following sections.

7.1 Components

The components contain the simulation specific functionality of the framework. In order to run a spectrum sensing simulation, different types of components, like, e. g., a signal source and a detection algorithm are necessary. An in-depth explanation of these different types of components is given in the following subsections.

7.1.1 Source

The framework's main purpose is to provide a reconfigurable system for doing Monte Carlo simulations that assess the performance of block-based spectrum sensing algorithms. Block-based spectrum sensing means that a sensor collects a block of consecutive time-domain samples, calculates a test statistic value from these and compares this value against a pre-specified threshold to decide between the two hypotheses, the one that a spectral band is free and can be utilized ($\mathcal{H}_0$), and the one that a PU signal is present in the band of interest such that the SU should refrain from accessing it ($\mathcal{H}_1$).

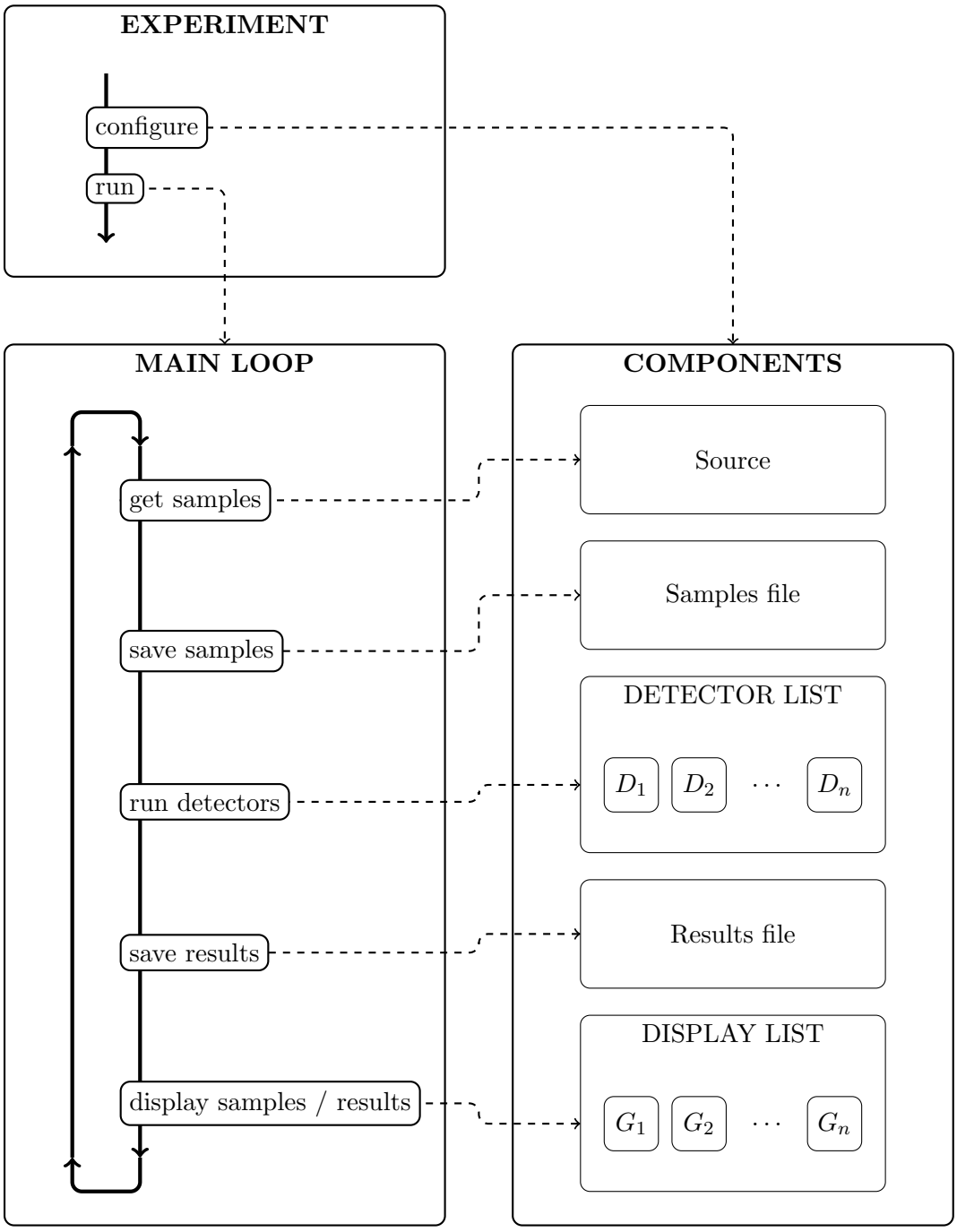

Figure 7.1: Block diagram providing an overview of the inner workings of the spectrum sensing simulation framework.

In the framework, the blocks of samples that are to be processed by the sensors are provided by the source component. Different sources can be implemented to reflect the different types of signal models considered in wireless communications. The sources can differ regarding the signal waveform, e. g., linearly modulated, orthogonal frequency-division multiplexing (OFDM), spread-spectrum coding, the implementation of a channel model, the type of receiver noise and signal properties like the modulation space and pulse shapes.

The source is expected to be configurable regarding the number of samples per block and the SNR of the emitted signal at the receiver(s) as well as a random number generator seed, which guarantees that simulations can be reproduced exactly.

The typical source generates the receiver signal randomly. However, two special sources that have been implemented are an exception to this rule. The first one is the Universal Software Radio Peripheral (USRP) source. It acts as an interface between the framework and a USRP device, which provides the source with the blocks of samples it emits. The source supports configuring the different run-time parameters of the USRP hardware, such as the center frequency of the sensed band. The second special source is the playback source. The framework supports saving the blocks of samples emitted by a source to a file. This file can be played back at a later simulation such that situations can be exactly reproduced, which is especially useful when working with samples from the USRP.

7.1.2 Detector

The detector component is the place where the actual spectrum sensing algorithms are implemented. For each block of samples that is provided to a detector, it computes a test statistic and compares it to a pre-defined threshold. Subsequently, it assembles a set of results consisting of everything that might be of interest for an eventual performance analysis and returns it.

The detector benefits from the object-oriented architecture of the framework, since detectors that are similar to each other can share code, e. g., signal processing routines, in a common parent class.

7.1.3 Display

The display component provides the user of the framework with real-time information about a simulation at run-time. It is provided with the results of all detectors as well as with the block of samples such that it has access to all relevant information regarding the simulation.

One example of a display is one that simply displays the PSD of the current block of samples. Another one calculates the cyclic autocorrelation (CA) of the block of samples and displays it for different time delays. An example of a display that provides the user

with information gained from the detectors' results is one that shows the histograms of the empirical test statistics of the different detectors and updates them for each new block of samples that is processed.

Using these displays, the user of the framework can quickly experiment with different parameters before starting a long-running Monte Carlo simulation or check if the USRP system is working as expected.

7.2 Main Loop

The main loop is the part of the framework that connects all components and routes the data to the places where it is processed. Each iteration of the main loop stands for one block of samples, i. e., one Monte Carlo instance of the spectrum sensing simulation.

For each block of samples it first lets the source generate the actual samples. Depending on the simulation configuration it then saves the block to a file for later reproduction of the simulation. A simulation can be set up to compare multiple different spectrum sensing algorithms, which are represented by objects in a detector list. The main loop lets each of these detectors run their detection routine on the same block of samples. This ensures that when comparing the performance of different detectors, they are not only assessed with input that was generated from the same model with the same statistical properties but with the exact same data. After saving the results of all detectors to files for later evaluation, it provides each of the displays in the display list with the data from the current iteration, i. e., the block of raw samples as well as the results of the detectors, such that the displays have access to all information necessary to update what is shown to the user.

The main loop defines a fixed process that is executed in every spectrum sensing simulation. Its implementation is fixed and should not need to be changed from simulation to simulation. One of the advantages of this concept is that the basic course of actions all spectrum sensing simulations go through does not have to be implemented or adapted for each simulation anew, which saves time and reduces the potential for bugs in the code. Another benefit of its fixed nature is that interfaces stay fixed over a long time, which makes the existing components like detectors and sources more long-lived.

7.3 Experiments

An experiment describes a simulation. While the main loop and the components are configurable, the experiment contains all the necessary parameters. In the first part of an experiment, the components that are to be used in the simulation are selected and configured with a set of parameters. In the second part, the main loop is executed with these settings.

This architecture makes it very easy to reuse already written code and compare different algorithms or signal models. For instance, adding a detector to the comparison or changing the signal that is to be detected each is a change of a single line in the experiment and does not touch the actual implementation of said components. Separating the algorithms, i. e., the components and the main loop, from the parameters and the configuration, i. e., the experiment, facilitates the reusability of the code and reduces the potential for making errors when modifying code. To run a simulation with a given set of parameters to compare the performance of a given set of detectors on a given type of signal, the only file that has to be edited is the experiment, which facilitates the overall stability of the simulation code. This also means that especially when working together in a team, it is easy to track which persons made changes to which part of the simulation, again reducing the potential for making mistakes. When a new detector or a new source is implemented, this is independent of all other parts of the code.

Another advantage of experiments is that they can be archived, which enhances reproducibility. To test a new set of parameters, one can create a new experiment, leaving past experiments intact.

7.4 Conclusion

A spectrum sensing simulation framework has been developed to facilitate the numerical evaluation of the algorithms proposed in this thesis. It has a modular architecture, which benefits the code stability by dividing the code in small logical units, such that when a component is created or modified, most files belonging to the simulation are left unchanged. Another benefit of the modular nature of the framework is that the code of components, like signal sources or detection algorithms, is made highly reusable. The separation of algorithms and data as well as the configurability facilitated by the use of experiment files leads to ease of comparison of different spectrum sensing algorithms and different parameter sets.

8 Conclusions

8.1 Summary

Reliable spectrum sensing is the main enabler for opportunistic access to the underutilized wireless spectrum. The task of a spectrum sensing algorithm is to decide between two hypotheses, the one that the spectral band under observation is free and can be used by a secondary system ($\mathcal{H}_0$), and the one that the primary system is transmitting on the band, such that the secondary system needs to refrain from accessing it ($\mathcal{H}_1$). The goal in the design of spectrum sensing algorithms is to maximize the probability of detecting a present primary system transmission (probability of detection P_d) given a fixed probability of wrongly determining the band under observation to be occupied when it is not (probability of false alarm P_fa). In the case of a missed detection, i. e., when the primary system is transmitting but the spectrum sensing algorithm decides that the band is free, the secondary system might also start a transmission, by which it might disturb the primary system. When a false alarm happens, the secondary system misses a chance to use the spectrum. In this thesis, contributions have been made to three types of spectrum sensing algorithms.

The first type of spectrum sensing we consider is cyclostationarity detection. Cyclostationarity is a stochastic feature present in all man-made signals, e. g., wireless communication signals, but is absent in pure stationary noise. Due to this property it can be used to decide between $\mathcal{H}_0$ and $\mathcal{H}_1$, which makes it a good fit for spectrum sensing. The problem arising is that in order to determine the presence or absence of cyclostationarity in a received signal, it has to be known beforehand which cycle frequency is affected. In blind spectrum sensing it is assumed that the secondary system possesses no knowledge about the primary system signal, which, for the above reasons, rules out the use of cyclostationarity. Based on methods from the field of compressed sensing, two algorithms for tackling this problem are proposed. In a second step, a modification of the time-domain test (TDT) is devised to estimate the test statistic. This modification is necessary to work around the problem that when using the compressed sensing CA estimation algorithms, information required for estimating the spectrum sensing test statistic is lost. Furthermore, to assess the CA estimation performance of the aforementioned algorithms, a closed-form expression of the discrete-time cyclic autocorrelation of linearly modulated signals with a rectangular pulse shape is derived.

Eigenvalue-based spectrum sensing builds on the idea that a communication signal induces either correlation in time or correlation between different receivers, while pure

i.i.d. noise does not. The eigenvalues of a received signal's covariance matrix are used to define various test statistics for spectrum sensing. One of these is the condition number used in the maximum-minimum-eigenvalue (MME) detector. The MME detector is independent of uncertainty regarding the receiver noise power. In contrast, this uncertainty has been shown to lead to an SNR-wall in the energy detector. An SNR-wall constitutes the SNR-value that separates the regime where a detector can robustly detect a primary system signal and the regime where it cannot. Obviously, not exhibiting an SNR-wall is a desired feature of spectrum sensing algorithms. Unfortunately, the MME detector does not possess this feature. Indeed, in this work we show that the MME detector suffers from an SNR-wall induced by uncertainty regarding the amount of coloring of the receiver noise. A lower bound on this SNR-wall is derived and examples for different types of covariance matrices are given. Moreover, it is shown that low amounts of man-made impulsive noise already lead to enough uncertainty in the noise coloring that an SNR-wall considerably far above the desired regime of operation is brought about. Furthermore, two new test statistics for spectrum sensing based on the eigenvalues of the received signal's covariance matrix are proposed.

One of the oldest test statistics used in spectrum sensing is the received signal power. The corresponding method goes by the name of energy detection. It consists of measuring the received energy in a spectral band and comparing it to a predefined threshold. One of the problems occurring in spectrum sensing is the so-called hidden terminal problem, which leads to an SNR between the active node of the primary system and the secondary system sensor that is too low for reliable detection. In order to avoid the problem, a set of spatially distributed sensors is deployed. To exploit the spatial diversity, the sensors have to transmit either a local decision on the spectrum occupancy or their measurement data to a fusion center for combined analysis and decision making. To minimize the resulting overhead in spectrum usage, compressed sensing methods are utilized.

Finally, the architecture of the simulation framework used for most numerical evaluations presented in this work is described. It facilitates the reuse of code and benefits its stability.

8.2 Outlook

One task of special interest for future research is proving the existence of SNR-walls for new kinds of spectrum sensing algorithms. While the literature has seen proofs for the energy detector, the matched filter detector, the cyclostationarity detector, and (in this thesis) the eigenvalue-based MME detector, it is conjectured that all spectrum sensing algorithms suffer from this shortcoming. Facing this problem and analyzing the severity of these deficiencies would greatly benefit the comparability of the algorithms.

Another topic that should be considered is the derivation of closed-form expressions for the cyclic autocorrelation of different types of signals. While there is a rich literature on

the topic, it is not comprehensive. These closed-form solutions are crucial for assessing the performance of CA estimation algorithms.

The use of compressed sensing in spectrum sensing is still in its infancy. Thus, all areas of the field should be investigated regarding a possible beneficial application of CS. While bounds for the performance of compressed sensing in the estimation step of spectrum sensing are known, it would be interesting to have bounds that span the whole spectrum sensing process, e. g., it would be interesting to have a bound that directly links the detection performance to the compression rate.

Acronyms

AWGN	additive white Gaussian noise.
BP	basis pursuit.
BPDN	basis pursuit denoising.
BPSK	binary phase shift keying.
CA	cyclic autocorrelation.
CFAR	constant false alarm rate.
CoSaMP	compressive sampling matching pursuit.
CR	cognitive radio.
CS	compressed sensing.
DC	direct current.
DFT	discrete Fourier transform.
DICE	dictionary assisted CA estimator.
DME	difference-of-means-of-eigenvalues.
FC	fusion center.
FSS	fixed sample size.
GLR	generalized likelihood ratio.
HTP	hard thresholding pursuit.
IDFT	inverse discrete Fourier transform.
IHT	iterative hard thresholding.
IoT	Internet of Things.
JPEG	Joint Photographic Experts Group.
M2M	machine to machine.
MC	matrix completion.
MME	maximum-minimum-eigenvalue.
MMME	maximum-minus-minimum-eigenvalue.
MPEG	Moving Picture Experts Group.
MSE	mean squared error.

MWC	modulated wideband converter.
NRMSE	normalized root mean squared error.
NSP	null space property.
OFDM	orthogonal frequency-division multiplexing.
OMP	orthogonal matching pursuit.
OSA	opportunistic spectrum access.
PD	probability distribution.
PDF	probability density function.
PSD	power spectral density.
PU	primary user.
QCBP	quadratically constrained basis pursuit.
QD	quickest detection.
RIP	restricted isometry property.
ROC	receiver operating characteristic.
SC	spectral correlation.
SCM	slot comparison method.
SM	symmetry method.
SNR	signal-to-noise ratio.
SOBER	SOMP-based CA estimator.
SOMP	simultaneous orthogonal matching pursuit.
SP	spectrum pooling.
SU	secondary user.
TDT	time-domain test.
USRP	Universal Software Radio Peripheral.

Bibliography

[1] National Telecommunications & Information Administration - United States Department of Commerce, "United States Frequency Allocation Chart," Aug. 2011. [Online]. Available: http://www.ntia.doc.gov/page/2011/united-states-frequency-allocation-chart

[2] Bundesnetzagentur, "Frequenznutzungsplan," Jan. 2014. [Online]. Available: http://www.bundesnetzagentur.de/DE/Sachgebiete/Telekommunikation/Unternehmen_Institutionen/Frequenzen/Grundlagen/Frequenzplan/frequenzplan-node.html

[3] FCC Spectrum Policy Task Force, "Report of the Spectrum Efficiency Working Group," Federal Communications Commission (FCC), Tech. Rep., Nov. 2002. [Online]. Available: http://www.fcc.gov/sptf/reports.html

[4] V. Valenta, R. Maršálek, G. Baudoin, M. Villegas, M. Suarez, and F. Robert, "Survey on spectrum utilization in Europe: Measurements, analyses and observations," in *International Conference on Cognitive Radio Oriented Wireless Networks Communications (CROWNCOM)*, Jun. 2010, pp. 1–5.

[5] R. Raji, "Smart networks for control," *IEEE Spectrum*, vol. 31, no. 6, pp. 49–55, Jun. 1994.

[6] L. Atzori, A. Iera, and G. Morabito, "The Internet of Things: A survey," *Computer Networks*, vol. 54, no. 15, pp. 2787–2805, Oct. 2010.

[7] J. Holler, V. Tsiatsis, C. Mulligan, S. Avesand, S. Karnouskos, and D. Boyle, *From Machine-to-Machine to the Internet of Things: Introduction to a New Age of Intelligence*. Academic Press, 2014.

[8] I. F. Akyildiz and M. C. Vuran, *Wireless sensor networks*. John Wiley & Sons, 2010.

[9] Q. Zhao and B. Sadler, "A Survey of Dynamic Spectrum Access," *IEEE Signal Processing Magazine*, vol. 24, no. 3, pp. 79–89, May 2007.

[10] J. Mitola, "Cognitive radio for flexible mobile multimedia communications," in *IEEE International Workshop on Mobile Multimedia Communications (MoMuC)*, Nov. 1999, pp. 3–10.

[11] J. Mitola and G. Q. J. Maguire, "Cognitive radio: making software radios more personal," *IEEE Personal Communications*, vol. 6, no. 4, pp. 13–18, Aug. 1999.

[12] S. Haykin, "Cognitive Radio: Brain-Empowered Wireless Communications," *IEEE Journal on Selected Areas in Communications*, vol. 23, no. 2, pp. 201–220, Feb. 2005.

[13] Y. Pati, R. Rezaiifar, and P. Krishnaprasad, "Orthogonal matching pursuit: recursive function approximation with applications to wavelet decomposition," in *Asilomar Conference on Signals, Systems and Computers*, Nov. 1993, pp. 40–44.

[14] S. Mallat and Z. Zhang, "Matching pursuits with time-frequency dictionaries," *IEEE Transactions on Signal Processing*, vol. 41, no. 12, pp. 3397–3415, Dec. 1993.

[15] A. V. Dandawate and G. B. Giannakis, "Statistical Tests for Presence of Cyclostationarity," *IEEE Transactions on Signal Processing*, vol. 42, no. 9, pp. 2355 –2369, Sep. 1994.

[16] Y. Zeng and Y.-C. Liang, "Maximum-Minimum Eigenvalue Detection for Cognitive Radio," in *IEEE International Symposium on Personal, Indoor and Mobile Radio Communications (PIMRC)*, Sep. 2007, pp. 1–5.

[17] S. Corroy, A. Bollig, and R. Mathar, "Distributed sensing of a slowly time-varying sparse spectrum using matrix completion," in *International Symposium on Wireless Communication Systems (ISWCS)*, Nov. 2011.

[18] A. Bollig, S. Corroy, and R. Mathar, "Joint Sparse Spectrum Reconstruction and Information Fusion via ℓ_1-Minimization," in *IEEE Vehicular Technology Conference (VTC) Spring*, May 2012.

[19] A. Bollig and R. Mathar, "Dictionary-based reconstruction of the cyclic autocorrelation via ℓ_1-minimization," in *IEEE International Conference on Acoustics, Speech and Signal Processing (ICASSP)*, May 2013.

[20] ——, "MMME and DME: Two new eigenvalue-based detectors for spectrum sensing in cognitive radio," in *IEEE Global Conference on Signal and Information Processing (GlobalSIP)*, Dec. 2013.

[21] A. Lavrenko, A. Bollig, and R. S. Thomä, "Compressive Energy Detection for Blind Coarse Wideband Sensing: Comparative Performance Study," in *International Symposium on Wireless Communication Systems (ISWCS)*, Aug. 2015.

[22] M. Arts, A. Bollig, and R. Mathar, "Analytical test statistic distributions of the MMME eigenvalue-based detector for spectrum sensing," in *International Symposium on Wireless Communication Systems (ISWCS)*, Aug. 2015.

[23] A. Bollig, M. Arts, A. Lavrenko, and R. Mathar, "Compressive Cyclostationary Spectrum Sensing with a Constant False Alarm Rate," 2016, submitted for review. [Online]. Available: https://arxiv.org/abs/1610.04027

[24] A. Bollig, C. Disch, M. Arts, and R. Mathar, "SNR-Walls in Eigenvalue-based Spectrum Sensing," 2016, submitted for review. [Online]. Available: https://arxiv.org/abs/1610.03892

[25] S. Foucart and H. Rauhut, *A Mathematical Introduction to Compressive Sensing.* Springer, 2013.

[26] A. Wald, *Sequential analysis.* John Wiley & Sons, 1947.

[27] H. V. Poor and O. Hadjiliadis, *Quickest detection.* Cambridge University Press, 2008.

[28] M. Basseville, I. V. Nikiforov, and others, *Detection of abrupt changes: theory and application.* Prentice Hall Englewood Cliffs, 1993.

[29] A. Sonnenschein and P. Fishman, "Radiometric detection of spread-spectrum signals in noise of uncertain power," *IEEE Transactions on Aerospace and Electronic Systems*, vol. 28, no. 3, pp. 654–660, Jul. 1992.

[30] R. Tandra and A. Sahai, "SNR Walls for Signal Detection," *IEEE Journal of Selected Topics in Signal Processing*, vol. 2, no. 1, pp. 4–17, Feb. 2008.

[31] ——, "SNR Walls for Feature Detectors," in *IEEE International Symposium on New Frontiers in Dynamic Spectrum Access Networks (DySPAN)*, Apr. 2007, pp. 559–570.

[32] S. M. Kay, *Fundamentals of Statistical Signal Processing, Vol. II: Detection Theory.* Prentice Hall, 1998.

[33] T. Yücek and H. Arslan, "A Survey of Spectrum Sensing Algorithms for Cognitive Radio Applications," *IEEE Communications Surveys Tutorials*, vol. 11, no. 1, pp. 116 –130, Mar. 2009.

[34] Y. Zeng, Y.-C. Liang, A. T. Hoang, and R. Zhang, "A Review on Spectrum Sensing for Cognitive Radio: Challenges and Solutions," *EURASIP Journal on Advances in Signal Processing*, vol. 2010, Jan. 2010.

[35] E. Axell, G. Leus, E. Larsson, and H. Poor, "Spectrum Sensing for Cognitive Radio : State-of-the-Art and Recent Advances," *IEEE Signal Processing Magazine*, vol. 29, no. 3, pp. 101–116, May 2012.

[36] H. Urkowitz, "Energy Detection of Unknown Deterministic Signals," *Proceedings of the IEEE*, vol. 55, no. 4, pp. 523–531, Apr. 1967.

[37] J. Neyman and E. S. Pearson, "On the Problem of the Most Efficient Tests of Statistical Hypotheses," *Philosophical Transactions of the Royal Society of London A: Mathematical, Physical and Engineering Sciences*, vol. 231, no. 694-706, pp. 289–337, Jan. 1933.

[38] A. Sahai, N. Hoven, and R. Tandra, "Some fundamental limits on cognitive radio," in *Allerton Conference on Communication, Control, and Computing.* Monticello, Illinois, Sep. 2004, pp. 1662–1671.

[39] E. Larsson and M. Skoglund, "Cognitive radio in a frequency-planned environment: some basic limits," *IEEE Transactions on Wireless Communications*, vol. 7, no. 12, pp. 4800–4806, Dec. 2008.

[40] W. A. Gardner, "Exploitation of Spectral Redundancy in Cyclostationary Signals," *IEEE Signal Processing Magazine*, vol. 8, no. 2, pp. 14 –36, Apr. 1991.

[41] ——, "Signal Interception: A Unifying Theoretical Framework for Feature Detection," *IEEE Transactions on Communications*, vol. 36, no. 8, pp. 897 –906, Aug. 1988.

[42] J. Lundén, V. Koivunen, A. Huttunen, and H. Poor, "Collaborative Cyclostationary Spectrum Sensing for Cognitive Radio Systems," *IEEE Transactions on Signal Processing*, vol. 57, no. 11, pp. 4182 –4195, Nov. 2009.

[43] S. Enserink and D. Cochran, "A cyclostationary feature detector," in *Asilomar Conference on Signals, Systems and Computers*, Oct. 1994, pp. 806–810.

[44] Y. Zeng and Y.-C. Liang, "Spectrum-Sensing Algorithms for Cognitive Radio Based on Statistical Covariances," *IEEE Transactions on Vehicular Technology*, vol. 58, no. 4, pp. 1804–1815, Sep. 2008.

[45] ——, "Eigenvalue-based spectrum sensing algorithms for cognitive radio," *IEEE Transactions on Communications*, vol. 57, no. 6, pp. 1784–1793, Jun. 2009.

[46] Y. Zeng, Y.-C. Liang, and R. Zhang, "Blindly Combined Energy Detection for Spectrum Sensing in Cognitive Radio," *IEEE Signal Processing Letters*, vol. 15, pp. 649–652, Oct. 2008.

[47] X. Yang, K. Lei, S. Peng, and X. Cao, "Blind Detection for Primary User Based on the Sample Covariance Matrix in Cognitive Radio," *IEEE Communications Letters*, vol. 15, no. 1, pp. 40–42, Jan. 2011.

[48] J. Font-Segura, J. Riba, J. Villares, and G. Vazquez, "Quadratic Sphericity Test for Blind Detection over Time-Varying Frequency-Selective Fading Channels," in *IEEE International Conference on Acoustics, Speech, and Signal Processing (ICASSP)*, May 2013, pp. 4708–4712.

[49] E. J. Candès, J. Romberg, and T. Tao, "Robust Uncertainty Principles: Exact Signal Reconstruction From Highly Incomplete Frequency Information," *IEEE Transactions on Information Theory*, vol. 52, no. 2, pp. 489–509, Feb. 2006.

[50] D. L. Donoho, "Compressed Sensing," *IEEE Transactions on Information Theory*, vol. 52, no. 4, pp. 1289–1306, Apr. 2006.

[51] H. Nyquist, "Certain Topics in Telegraph Transmission Theory," *Transactions of the American Institute of Electrical Engineers*, vol. 47, no. 2, pp. 617–644, Apr. 1928.

[52] C. Shannon, "Communication in the Presence of Noise," *Proceedings of the IRE*, vol. 37, no. 1, pp. 10–21, Jan. 1949.

[53] H. D. Lüke, "The origins of the sampling theorem," *IEEE Communications Magazine*, vol. 37, no. 4, pp. 106–108, Apr. 1999.

[54] D. L. Donoho, "For Most Large Underdetermined Systems of Linear Equations the Minimal ℓ_1-norm Solution is also the Sparsest Solution," *Communications on Pure and Applied Mathematics*, vol. 59, pp. 797–829, Sep. 2004.

[55] S. Chen, D. Donoho, and M. Saunders, "Atomic Decomposition by Basis Pursuit," *SIAM Journal on Scientific Computing*, vol. 20, no. 1, pp. 33–61, Jan. 1998.

[56] D. Needell and J. A. Tropp, "CoSaMP: Iterative Signal Recovery from Incomplete and Inaccurate Samples," *Commun. ACM*, vol. 53, no. 12, pp. 93–100, Dec. 2010.

[57] A. Cohen, W. Dahmen, and R. DeVore, "Compressed sensing and best k-term approximation," *Journal of the American Mathematical Society*, vol. 22, no. 1, pp. 211–231, Jul. 2008.

[58] E. Candes and T. Tao, "Decoding by linear programming," *IEEE Transactions on Information Theory*, vol. 51, no. 12, pp. 4203–4215, Dec. 2005.

[59] Y. C. Eldar and G. Kutyniok, *Compressed sensing: theory and applications.* Cambridge University Press, 2012.

[60] A. Tillmann and M. Pfetsch, "The Computational Complexity of the Restricted Isometry Property, the Nullspace Property, and Related Concepts in Compressed Sensing," *IEEE Transactions on Information Theory*, vol. 60, no. 2, pp. 1248–1259, Feb. 2014.

[61] A. Goldsmith, *Wireless Communications.* Cambridge University Press, 2005.

[62] W. A. Gardner, Ed., *Cyclostationarity in communications and signal processing.* IEEE Press, 1994.

[63] Z. Khalaf and J. Palicot, "New Blind Free-Band Detectors Exploiting Cyclic Autocorrelation Function Sparsity," in *Cognitive Communication and Cooperative HetNet Coexistence.* Springer, 2014, pp. 91–117.

[64] Z. Tian, Y. Tafesse, and B. Sadler, "Cyclic Feature Detection With Sub-Nyquist Sampling for Wideband Spectrum Sensing," *IEEE Journal of Selected Topics in Signal Processing*, vol. 6, no. 1, pp. 58 –69, Feb. 2012.

[65] E. Rebeiz, V. Jain, and D. Cabric, "Cyclostationary-based Low Complexity Wideband Spectrum Sensing Using Compressive Sampling," in *IEEE International Conference on Communications (ICC)*, Jun. 2012, pp. 1619–1623.

[66] D. Cohen, E. Rebeiz, V. Jain, Y. Eldar, and D. Cabric, "Cyclostationary Feature Detection from Sub-Nyquist Samples," in *IEEE International Workshop on Computational Advances in Multi-Sensor Adaptive Processing (CAMSAP)*, Dec. 2011, pp. 333–336.

[67] M. Mishali and Y. Eldar, "From Theory to Practice: Sub-Nyquist Sampling of Sparse Wideband Analog Signals," *IEEE Journal of Selected Topics in Signal Processing*, vol. 4, no. 2, pp. 375–391, Apr. 2010.

[68] A. Napolitano, *Generalizations of Cyclostationary Signal Processing: Spectral Analysis and Applications.* John Wiley & Sons, 2012.

[69] J. Tropp, A. Gilbert, and M. Strauss, "Simultaneous Sparse Approximation via Greedy Pursuit," in *IEEE International Conference on Acoustics, Speech and Signal Processing (ICASSP)*, vol. 5, Mar. 2005, pp. 721–724.

[70] W. A. Gardner, *Statistical Spectral Analysis: A Nonprobabilistic Theory.* Prentice-Hall, Inc., 1986.

[71] M. Abramowitz and I. A. Stegun, *Handbook of Mathematical Functions with Formulas, Graphs, and Mathematical Tables.* Courier Corporation, 1964.

[72] IEEE, "IEEE Standard for Information Technology–Telecommunications and information exchange between systems; Wireless Regional Area Networks (WRAN)–Specific requirements Part 22: Cognitive Wireless RAN Medium Access Control (MAC) and Physical Layer (PHY) Specifications: Policies and Procedures for Operation in the TV Bands," *IEEE Std 802.22-2011*, Jul. 2011.

[73] P. J. Huber, *Robust statistics.* Springer, 2011.

[74] A. Papoulis and S. U. Pillai, *Probability, random variables, and stochastic processes*, 4th ed. McGraw-Hill, 2002.

[75] I. Shomorony and A. Avestimehr, "Worst-Case Additive Noise in Wireless Networks," *IEEE Transactions on Information Theory*, vol. 59, no. 6, pp. 3833–3847, Jun. 2013.

[76] International Telecommunication Union, "Recommendation P.372-12 : Radio noise," Tech. Rep., Jul. 2015. [Online]. Available: https://www.itu.int/rec/R-REC-P.372-12-201507-I/en

[77] C. D. Motchenbacher and J. A. Connelly, *Low noise electronic system design.* Wiley, 1993.

[78] A. Wagstaff and N. Merricks, "Man-Made Noise Measurement Programme (AY4119) - Final Report," Mass Consultants Limited, Tech. Rep. Issue 2, Sep. 2003.

[79] R. M. Gray, *Toeplitz and circulant matrices: A review.* now publishers inc, 2006.

[80] S. Gerschgorin, "Über die Abgrenzung der Eigenwerte einer Matrix," *Bulletin de l'Académie des Sciences de l'URSS*, no. 6, pp. 749–754, 1931.

[81] H. A. DeJarnette III, "Measuring Noise in the VHF Band and Its Effect On Low SNR Signal Detection," Virginia Polytechnic Institute and State University, Tech. Rep., Sep. 2012.

[82] Z. Tian, "Compressed Wideband Sensing in Cooperative Cognitive Radio Networks," in *IEEE Global Communications Conference (GLOBECOM)*, Nov. 2008.

[83] L. Xiao, S. Boyd, and S.-J. Kim, "Distributed average consensus with least-mean-square deviation," *Journal of Parallel and Distributed Computing*, vol. 67, no. 1, pp. 33 – 46, Jan. 2007.

[84] E. J. Candès and Y. Plan, "Matrix Completion With Noise," *Proceedings of the IEEE*, vol. 98, no. 6, pp. 925–936, Jun. 2010.

[85] R. Keshavan, A. Montanari, and S. Oh, "Matrix completion from noisy entries," *The Journal of Machine Learning Research*, vol. 99, pp. 2057–2078, Aug. 2010.

[86] M. Grant and S. Boyd, *CVX: Matlab Software for Disciplined Convex Programming, version 2.1*, Mar. 2014. [Online]. Available: http://cvxr.com/cvx

Curriculum Vitæ

Andreas Karl Bollig	Born on 28th of October 1985 in Wittlich, Germany

Education

1992-1996	Elementary school in Wittlich, Germany
1996-2005	Academic high school in Wittlich, Germany
March 4, 2005	General qualification for university entrance (Abitur)
04/2005-10/2005	Civil service in Wittlich, Germany
10/2005-05/2011	Studies in computer engineering, Faculty of Electrical Engineering and Information Technology, RWTH Aachen University, Aachen, Germany
May 25, 2011	Diploma degree in computer engineering from RWTH Aachen University, Aachen, Germany
07/2011-10/2016	Pursuing the doctoral degree in electrical engineering

Professional Experience

04/2006-09/2010	Student researcher at different institutes of RWTH Aachen University (overall 3.75 years employed), Aachen, Germany
10/2009-03/2010	Intern at Global IP Solutions (now part of Google), Stockholm, Sweden
07/2011-02/2016	Scientific Staff Member (Research Assistant) at the Institute for Theoretical Information Technology of RWTH Aachen University, Aachen, Germany
Since 02/2016	Data Scientist at AXA Konzern AG, Cologne, Germany